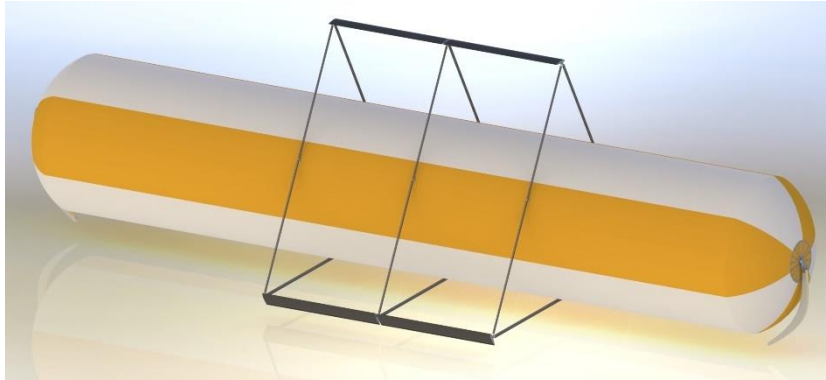




TÉCNICO
LISBOA



Structural Analysis of a Vertical Axis Wind Turbine with a Cylinder in the Central Axis

Catarina Correia Gonçalves

Thesis to obtain the Master of Science Degree in

Mechanical Engineering

Supervisor: Prof. António Manuel Relógio Ribeiro

Examination Committee

Chairperson: Prof. Luís Filipe Galvão dos Reis

Supervisor: Prof. António Manuel Relógio Ribeiro

Member of the Committee: Prof. Filipe Szolnoky Ramos Pinto Cunha

December 2018

Acknowledgements

First, I would like to thank my supervisor Professor Relógio Ribeiro for his guidance, support and availability throughout this thesis; and other professors from IST who were kind enough to help me.

I would also like to thank *Omnidea* for the opportunity to participate in this work, especially Pedro Silva and Paulo Gordo, my supervisors, and other workers at *Omnidea* who were available to guide me through the project.

My family, for all the support and patience they had during this period, and who always supported my decisions and motivated me to do better.

To my friends from high school, Marta, Tiago, Nuno and Jorge, I give a special thank you for always being by my side all these years, for the good times and the bad, which we always overcame together.

I also have to thank my friends from IST, especially the ones from PSEM, the team with whom I spent most of time in university and where I learned more than I could ever have without it. Through all the sweat, blood and tears I know I made friends for life.

I would particularly like to thank Fred for all the help he gave with my thesis, even with the stupid questions, and especially with the simulation's software.

I also want to thank the guys from Lab2ProD who put up with and helped me more than I could ever expect in the final stretch of this thesis.

Last but not least, I want to thank Dias and Pedro, who've been with me in IST from the start. Isabel, who, despite being constantly away in some country, is always nearby with her craziness. Finally, Rita, whom I could never get rid of. For all the cries and the laughs, the mutual encouragement, emotional support and the shared madness.

Abstract

Wind energy has benefited from a rising interest in the development of new and innovative solutions for harvesting wind power. Some projects have focused on harvesting wind from higher altitudes – the high-altitude wind energy systems. This thesis follows the design and development of a new wind turbine concept, which consists of applying the concept of a vertical axis wind turbine to an airborne module, based on the Magnus effect, already developed by *Omnidea*. This work will assess the viability of such a project. To start, a few concept ideas were compared in a concept screening process. Having chosen the main design, core parameters and values were analysed and chosen in order to maximize the efficiency. The next step was to design the mechanical components needed for the structure and define materials, taking into account the importance of minimizing the weight. For the system to float, the total weight of the structure and every part attached to the balloon could not weigh more than the buoyancy offered by the balloon – approximately 250 kg. After a design update, brought by the results of the finite element analyses, the total weight of the system rounded up to 264 kg. This could be addressed by creating a new module with higher length; or adding a smaller balloon to the existing one that could provide extra buoyancy.

Keywords: Wind turbine, vertical axis wind turbine, airborne wind system, Magnus effect, composite materials

Resumo

A energia eólica tem beneficiado de um crescente interesse no desenvolvimento de novas e inovadoras soluções para captação da energia do vento. Alguns destes projetos têm-se desenvolvido no sentido de captar energia do vento a maiores altitudes. Esta tese segue o design e desenvolvimento de um novo conceito de turbina eólica, que consiste em aplicar o conceito de uma turbina eólica de eixo vertical a um módulo aéreo, desenvolvido pela *Omnidea*, cujo funcionamento se baseia no efeito de Magnus. Este trabalho avalia a viabilidade e possibilidade de construção de tal projeto. Inicialmente, alguns conceitos preliminares foram comparados num processo de avaliação de conceitos. Tendo escolhido o design geral, os principais parâmetros e valores que definem uma turbina eólica foram analisados e escolhidos de forma a maximizar a eficiência. O próximo passo consistiu em desenhar os componentes da estrutura e definir materiais, atendendo à importância de minimizar o peso. Para que o sistema possa flutuar, o peso total da estrutura e todos os componentes adjacentes ao balão não pode ultrapassar a flutuabilidade oferecida pelo mesmo, que está cheio de hélio – aproximadamente 250 kg. Após uma atualização do design decorrente dos resultados das simulações numéricas, o peso total da estrutura chegou aos 264 kg. Isto poderia ser resolvido acrescentando ao sistema um outro balão mais pequeno que dê flutuabilidade extra ou desenvolvendo um novo módulo com maior comprimento.

Palavras-chave: Turbina eólica, turbina eólica de eixo vertical, sistema eólico flutuante, efeito de Magnus, materiais compósitos

Table of Contents

Acknowledgements	iii
Abstract	v
Resumo	vii
Table of Contents	ix
List of tables	xi
List of figures	xiii
List of Abbreviations	xvii
Nomenclature	xvii
1. Introduction	1
1.1. The high-altitude wind energy system	1
1.2. Objectives	3
1.3. Thesis Outline	3
2. State of the Art	5
2.1. The importance of Renewable Energies	5
2.2. Wind Energy	6
2.3. Wind turbines	9
2.4. Aerodynamic characteristics of a lift type turbine	13
3. Concept Generation	19
3.1. Concept selection	19
3.2. Decision Process	19
3.3. Concept Screening	21
4. Conceptual Design and Parameters	25
4.1. Design methodology	25
4.2. Description of the concept	25
4.3. Control Mechanism	26
4.4. Design Values and Parameters	27
5. Mechanical Design	37
5.1. Description of the updated concept	37
5.2. Materials	37
5.3. Support arms design	41

5.4.	Guy-wires	43
5.5.	Generator	43
5.6.	Drivetrain	45
5.7.	Balloon and turbine tether components	46
5.8.	Buoyancy and weight distribution	48
5.9.	Load Calculation	49
5.10.	Safety Factors.....	53
6.	Finite Element Analysis	57
6.1.	Finite Element Method.....	57
6.2.	Composite Failure Theory	57
6.3.	Simulations	58
7.	Conclusions and/or Future work.....	71
7.1.	Conclusions	71
7.2.	Future work.....	71
8.	References.....	73
	Appendix A	77
	Appendix B.....	80
	Appendix C.....	82

List of tables

- Table 3-1 List of needs.....20
- Table 3-2 List of metrics20
- Table 3-3 Needs-metrics matrix21
- Table 3-4 Concept Scoring matrix.....23
- Table 4-1 Operation cases and corresponding conditions.....26
- Table 4-2 Computed values of Lb 35
- Table 5-1 Properties of Dyneema sk75. From [34].....38
- Table 5-2 Properties of standard carbon fibre fabric composite material, $V_f = 50\%$. From [35]39
- Table 5-3 Properties of Airex C70.5540
- Table 5-4 Properties of the aluminium alloys.....41
- Table 5-5 Technical properties of the 300STK3M frameless generator44
- Table 5-6 Main dimensions of the 300STK3M frameless generator.....44
- Table 5-7 Final dimensions of the gear pair45
- Table 5-8 Listing of weight of the structure's parts48
- Table 5-9 Partial safety factors for loads. From [41].....54
- Table 5-10 Partial safety factors for materials, for fatigue analysis. From [41]54
- Table 5-11 Reduction factors for the materials' partial safety factor. From [41].....55
- Table 6-1 Properties of standard carbon fibre fabric composite material, $V_f = 50\%$ 58
- Table 6-2 Values of ply failure index and ply strain for the different mesh sizes60
- Table 6-3 Radial and tangential maximum forces and their correspondent position60
- Table 6-4 Results of the iterations simulations.....62
- Table 6-5 Loads acting on each set of support arms.....63
- Table 6-6 Results for the different support arms' chord simulations.....65
- Table 6-7 Radial and tangential design forces for each position θ 66
- Table 6-8 Natural frequencies of the first ten normal modes of the structure69

List of figures

Figure 1-1 Example of the Magnus Effect: superposition of a laminar flow with a circular flow. Adapted from [1]..... 1

Figure 1-2 Schematic view of the concept based on the Magnus effect [2].....2

Figure 2-1 Global primary energy consumption by source, measured in terawatt-hours (TWh). Adapted from [6]5

Figure 2-2 World availability of land-based wind energy: estimated annual electric output in kWh/kW of a wind turbine rated at 11.2 m/s. As in figure 11.33 from [10]7

Figure 2-3 Average wind speeds in m/s at: (a) 120m; (b) 600m. Adapted from [12]8

Figure 2-4 Average power density in kW/m² at: (a) 120 m; (b) 600 m. Adapted from [12].....8

Figure 2-5 Visual comparison between the two wind turbine concepts denoted by the axis of rotation: (a) HAWT; (b) VAWT. Adapted from [13]9

Figure 2-6 Estimated performance of various wind turbine designs as a function of blade Tip Speed Ratio. Adapted from [10]..... 10

Figure 2-7 Typical power curve of a commercial wind turbine. As in [16]..... 11

Figure 2-8 Types of Vertical Axis Wind Turbines: (a) Savonius rotor; (b) Darrieus rotor; (c) H-Darrieus rotor. Adapted from [18]..... 11

Figure 2-9 Top view schematic of a Savonius rotor. Adapted from [19] 12

Figure 2-10 Top view schematic of a Darrieus rotor. Adapted from [19] 12

Figure 2-11 Definition of the force and velocity vectors. Adapted from [21]..... 14

Figure 2-12 Parameters concerning one revolution. Adapted from [22] 14

Figure 2-13 Relative velocity V_{rel} as a function of the position angle θ , for different values of TSR ... 15

Figure 2-14 Angle of attack α as a function of the position angle θ , for different values of TSR..... 16

Figure 3-1 Schematics of each different concept 19

Figure 4-1 NFWT concept design process 25

Figure 4-2 Initial concept design..... 26

Figure 4-3 Probability distribution for the site of operation..... 27

Figure 4-4 (a) Lift to drag ratio as a function of spinning ratio. Adapted from [28]; (b) Lift and drag coefficients as a function of spinning ratio 29

Figure 4-5 Performance curve of a typical Darrieus VAWT. Adapted from [10]..... 29

Figure 4-6 Relationship curves between power coefficient and blade number. As in [31]..... 30

Figure 4-7 Variation of components y and z of net aerodynamic force with θ on 2 (a) and 3 (b) bladed NFWT 31

Figure 4-8 Performance curves of S-VAWT for different values of σ . Adapted from [20] 32

Figure 4-9 Relationship curves between power coefficient and blade incidence angle. Adapted from [31] 33

Figure 4-10 Curves of lift-drag ratio of symmetric aerofoils at various relative thickness. Adapted from [31] 34

Figure 4-11 NACA0018 aerofoil characteristics by percentage of chord 34

Figure 5-1 Updated concept design 37

Figure 5-2 Stress-strain response of a Dyneema sk76 rope at multiple strain rates. From [33]	38
Figure 5-3 Example of an aerofoil cross-section with two shear webs. Adapted from [11]	39
Figure 5-4 Blade support arrangements: (a) simple support; (b) cantilever support; (c) overhang support. Adapted from [36]	41
Figure 5-5 E864 aerofoil characteristics by percentage of chord	42
Figure 5-6 Schematics of different arm configurations: (a) single arm type; (b) triangle type.	43
Figure 5-7 Schematic of the blade structure with guy-wires	43
Figure 5-8 Permanent magnets frameless generators. From [38]	44
Figure 5-9 Representative scheme of the generator's dimensions. From [38]	45
Figure 5-10 Gear transmission system	46
Figure 5-11 (a) Left end of the balloon, working as a “freewheel”; (b) right end of the balloon with the generator and drivetrain assemblies	46
Figure 5-12 Section view (a) and a close-up view (b) of the left side assembly	47
Figure 5-13 Arm support inserts	47
Figure 5-14 Blade support and blade cover inserts (a); interior view of the blade cover (b)	47
Figure 5-15 Schematic of the structure's off centre positioning with the cable	49
Figure 5-16 Total forces acting on a blade	50
Figure 5-17 Depiction of flapwise and edgewise bending	50
Figure 5-18 Position of support arms maximum load situation	52
Figure 5-19 Alignment of support arms sets 1 and 2	52
Figure 5-20 Schematic of the components of the relative velocity in relation to the support arms set 3	53
Figure 6-1 Representation of the chosen element	59
Figure 6-2 Relation between ply stress and number of elements – (a) ϵ_{11} (b) ϵ_{22} (c) ϵ_{12} – and between ply failure index and number of elements (d)	59
Figure 6-3 Element material orientation of blade meshes where the yellow arrows represent the 0° orientation	61
Figure 6-4 Meshed blade with applied loads and constraints	61
Figure 6-5 Different shear web configurations: (a) one shear web, iterations 1 and 4 through 7; (b) two shear webs, iteration 2; (c) shear web structure, iteration 3	62
Figure 6-6 Displacement for load case B, for iterations 1 (a) and 7 (b)	63
Figure 6-7 3D and 2D meshes of an arm support	64
Figure 6-8 Simplification of blade support and blade cover parts	64
Figure 6-9 Variation of displacement in node 6504233 (a) and maximum absolute displacement of the whole structure (b) in the y and z directions, in mm, with position θ	66
Figure 6-10 Variation of Ply Failure Index in element 5803420 with position θ	66
Figure 6-11 Variation of ply 1 strain in element 5803420 in the principal directions 11 (a), 22 (b) and 12 (c)	67
Figure 6-12 Variation of ply 1 maximum strain in element 5803420 in the principal directions 11 (a), 22 (b) and 12 (c)	67

Figure 6-13 Representation of maximum ϵ_{11} of the structure: (a) in compression and (b) in tension for position $\theta = 330^\circ$ 67

Figure 6-14 Representation of the Von Mises stress on the arm support (a) and blade support (b) for position $\theta = 330^\circ$ 67

Figure 6-15 Mode shapes of the structure: (a) mode 1; (b) mode 4; (c) mode 9; (d) mode 1068

List of Abbreviations

CFRP – Carbon Fibre Reinforced Polymer

FEA – Finite Element Analysis

FEM – Finite Element Method

GFRP – Glass Fibre Reinforced Polymer

HAWE – High-Altitude Wind Energy

HAWT – Horizontal Axis Wind Turbine

HMPE – High-modulus Polyethylene

NFWT – Normal Flow Wind Turbine

PFI – Ply Failure Index

S-VAWT – Straight Vertical Axis Wind Turbine

TSR – Tip Speed Ratio

VAWT – Vertical Axis Wind Turbine

Nomenclature

α	Angle of Attack
β	Blade Incidence Angle
Δp	Pressure Difference
$\varepsilon_{11}, \varepsilon_{12}, \varepsilon_{22}$	Strain in Principal Material Axes
$\varepsilon_{Lc}, \varepsilon_{Tc}$	Ultimate Compressive Strain 0°/90°
$\varepsilon_{Lt}, \varepsilon_{Tt}$	Ultimate Tensile Strain 0°/90°
$\varepsilon_{Lc}^d, \varepsilon_{Tc}^d$	Ultimate Compressive Design Strain 0°/90°
$\varepsilon_{Lt}^d, \varepsilon_{Tt}^d$	Ultimate Tensile Design Strain 0°/90°
ε_s	Ultimate Shear Strain
ε_s^d	Ultimate Shear Design Strain
γ	Blade's Local Angle of the Inflow
γ_F	Partial Safety Factor for Loads

γ_M	Partial Safety Factor for Materials
γ_{M0}	Basis Factor for Materials
ν_{LT}	Major Poisson's Ratio
ω	Rotational Speed
ω_{blade}	Blade Rotational Speed
ω_{cyl}	Cylinder Rotational Speed
ρ	Density
ρ_b	Density of the Blade Material
ρ_∞	Undisturbed Air Density
σ	Solidity
$\sigma_{Lt}^d, \sigma_{Tt}^d$	Ultimate Tensile Design Strength 0°/90°
$\sigma_{Lc}^d, \sigma_{Tc}^d$	Ultimate Compressive Design Strength 0°/90°
σ_{LT}^d	Ultimate In-Plane Shear Design Strength
σ_u	Ultimate Tensile Strength
σ_y	Tensile Yield Strength
θ	Position of the Blade
τ	Shear Strength
ν	Cinematic Viscosity of the Air
A	Area of the Surface through which the Wind passes
A_b	Blade Area
A_s	Blade Cross-Section
a	Scale Factor
a_{12}	Gears Centre Distance
b	Gear Width
C_{1a}	Reduction Factor for Influence of Ageing
C_{2a}	Reduction Factor for Temperature Effect

C_{3a}	Reduction Factor for Laminate Production
C_{4a}	Reduction Factor for Laminate Curing
C_D	Drag Coefficient
C_L	Lift Coefficient
C_P	Power Coefficient
$C_{P(max)}$	Maximum Power Coefficient
c	Blade Chord
c_{arm}	Support Arm Chord
D_1	Drive Gear Diameter
D_2	Driven Gear Diameter
D_{cyl}	Cylinder Diameter
D_{tur}	Turbine Diameter
E	Young's Modulus
E_L, E_T	Young's Modulus 0°/90°
e_{arm}	Support Arm Skin Thickness
F	Net Aerodynamic Force
F_{arm}^d	Support Arm Design Force
$F_{buoyant}$	Buoyant Force
F_c	Centrifugal Force
F_D	Drag Force
F_d	Design Force
F_k	Characteristic Force
F_L	Lift Force
F_N, F_T	Normal and Tangential Force
F_N^d, F_T^d	Normal and Tangential Design Force
G	Shear Modulus
G_{LT}	In-Plane Shear Modulus

g	Gravitational Acceleration
h	Elevation of a Point Above a Reference Plane in a Flow
i	Gear Ratio
k	Shape Factor
L_b	Blade Length
M	Normalized Gear Module
m	Mass of one Blade
m_f	Mass of Displaced Fluid
\dot{m}	Mass Flow
N_b	Number of Blades
P	Total Power
P_{avail}	Available Power in The Wind
P_{rated}	Rated Power
P_{rotor}	Rotor Harvested Power
\bar{P}	Total Average Power
\bar{P}_1	Average Power of one Blade
p	Pressure at a Point in a Flow
q_c	Distributed Centrifugal Load
q_T, q_N	Distributed Tangential and Normal Load
q_w	Distributed Gravity Load
q_w^t, q_w^n	Tangential and Normal Components of Distributed Gravity Load
R_b	Balloon Radius
R_{cyl}	Cylinder Radius
R_d	Design Strength
Re	Local Reynolds Number
R_k	Characteristic Strength
R_{tip}	Radius to Blade Tip

R_{tur}	Turbine Radius
S	Stress
S_L^+, S_T^+	Ultimate Tensile Strength 0°/90°
S_L^-, S_T^-	Ultimate Compressive Strength 0°/90°
S_{LT}	Ultimate In-Plane Shear Strength
T	Torque
TSR	Tip Speed Ratio
t	Lamina Thickness
t_{arm}	Support Arm Profile Thickness
V	Wind Velocity
V_b	Blade Speed
V_{cut-in}	Cut-In Speed
$V_{cut-out}$	Cut-Out Speed
V_∞	Undisturbed Wind Speed
V_{mf}	Most Frequent Wind Velocity
V_{rated}	Rated Speed
V_{rel}	Relative Velocity
$V_{rel,max}$	Maximum Relative Velocity
$V_{rel,min}$	Minimum Relative Velocity
V_{rel}^{arm}	Relative Velocity of the Arm
$V_{rel}^n V_{rel}^t$	Normal Tangential Component of Relative Velocity
W	Weight
X	Spinning Ratio
Z_1	Drive Gear Teeth Number
Z_2	Driven Gear Teeth Number

1. Introduction

1.1. The high-altitude wind energy system

This study centres around the evolution and performance assessment of the existing prototype of a High-Altitude Wind Energy (HAWE) system developed by *Omnidea*, a Portuguese company which develops research in aerospace technology and energy systems.

The current prototype is comprised of a lighter-than-air airborne module – a balloon – with a cylindrical shape (currently 18 m long and with a diameter of 3.68 m) which reaches high altitudes (> 500m) by means of the Magnus Effect; a ground station equipped with a control system and a motor/generator to which the wind power is transferred; and a tether cable, connecting the two.

The Magnus Effect consists of the appearance of a lift force on a rotating body subject to a flow. When a cylindrical body is immersed in a viscous flow, the mere translation does not provide it with any lift. However, when the cylinder is given rotation one gets a circular flow, coincident with the direction of the translation in its upper section resulting in higher velocities. In the lower section, the flows have opposite directions leading to lower velocities [1].

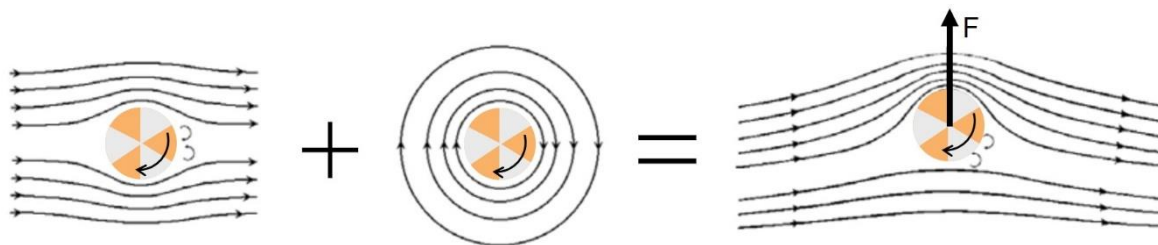


Figure 1-1 Example of the Magnus Effect: superposition of a laminar flow with a circular flow. Adapted from [1]

The difference in velocities around the cylinder generates a pressure difference which is given by Bernoulli's theory of potential flow

$$\frac{1}{2}\rho V^2 + \rho gh + p = const \quad (1.1)$$

Due to the pressure difference in the two sections of the cylinder, a transverse force is generated, perpendicular to the flow direction – the lift force. This force is proportional to the fluid velocity and the angular velocity of the cylinder.

Looking at *Omnidea's* airborne module, it is a cylindrical balloon filled with helium, thus becoming lighter than air, so it can stay afloat due to aerostatic lift, without the need for wind and with no power consumption. With a small electric motor mounted on the cylinder, powered from the ground through electrical cables inside the tether, the balloon can rotate. With angular velocity and the incidence of wind, aerodynamic lift is generated – Magnus effect – and the module gets airborne. The existing

aerodynamic drag and the tension from the cable allow for the alignment of the balloon with the direction of the wind [2].

Presently, the HAWE system can serve as an observation or surveillance platform that can carry payloads. It can be used for terrain observation and mapping or for telecommunications, as a signal receiver or extender. According to *Omnidea*, it is a long endurance platform, easily deployable and capable of reaching higher altitudes compared to other HAWE devices. Another purpose, on which this thesis is focused, is its capability to produce energy.

The power production is performed by the ascending and descending movements of the module, in four phases (Figure 1-2):

- **Unwinding (rising) phase** – The airborne module is set to maximum rotation until it reaches the operating altitude, defined beforehand; the cable is unwound and pulled up by the balloon, driving the generator at the ground station and producing electrical power.
- **Transition phase, T1** – when the operating altitude is reached the rotation is ceased and the aerodynamic lift lowers to zero. This way the energy needed for recovery is reduced.
- **Winding (recovery) phase** – the cable rewinds and the module is pulled down to the starting altitude through the electric motor at ground level. Here, the resisting forces are only the aerodynamic drag and the aerostatic lift.
- **Transition phase, T2** – when the original position is reached the rotation is restarted and a new cycle begins.

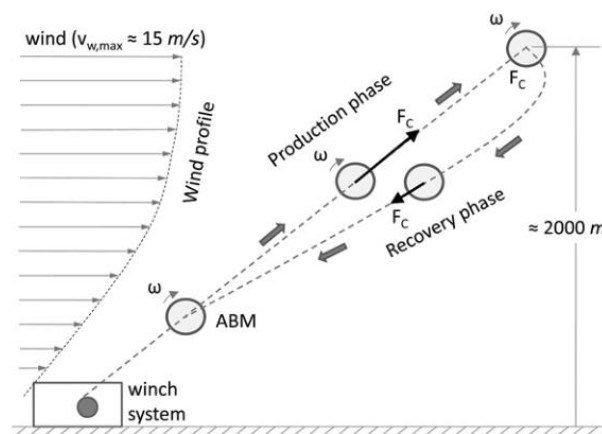


Figure 1-2 Schematic view of the concept based on the Magnus effect [2]

This system produces power in a discontinuous or intermittent cycle, through a production and a recovery phase. During the recovery phase, though in a small amount, there is energy consumption – for winding the cable – and no generation. Only during the unwinding phase there is production of energy. For the power production cycle to be effective there must be a surplus of energy left after the recovery phase. Perkovic et al. [3] performed a study where this surplus is proved to be attainable and relates to the magnitude of the relative wind speed.

The new project aims to change the way the platform produces power. The airborne module would integrate a turbine structure, based on vertical axis wind turbines (VAWT), and the generator would move from the ground to the platform. This would allow it to stay afloat for longer periods of time and to produce energy while it is in the air instead of having to cyclically ascend and descend.

1.2. Objectives

The primary goal of this thesis is to assess the viability/feasibility of applying the concept of a VAWT on a cylindrical balloon to work as an airborne wind system. For that it is necessary to understand the advantages and disadvantages along with the functioning of this type of turbines.

A design should be developed for the existing airborne module and its main components. The turbine ought to be dimensioned by analysis of the main parameters that affect power performance.

Finally, it is important to validate the designed structure and evaluate the lifetime of the new platform, since it is subject to time-varying, cyclic loads.

1.3. Thesis Outline

This thesis is structured in 7 chapters.

Chapter one presents an introduction to the subject addressed in this thesis, as well as the objectives proposed, and the work developed by *Omnidea*.

The second chapter addresses the theoretical aspects involved in wind turbines and aerodynamic characteristics, meaning, the forces and equations used to describe the phenomenon.

The third chapter is devoted to the concept selection process, where different preliminary designs for the turbine are compared according to certain requirements.

In chapter four an analysis of the different parameters that will affect the design, dimensions and the effective functioning of the wind turbine is made, refining the concept chosen from the previous chapter.

The fifth chapter concerns the mechanical design of the components. The drivetrain needed for the chosen generator and the remaining components are described and the materials are selected. The load calculation method is also described, and the partial safety factors are calculated.

The sixth chapter, of virtual prototyping, focuses on the numerical study of the designed turbine. Addressing first the analysis of a single blade and then the static and dynamic analysis of the full structure.

Finally, chapter seven presents the conclusions of this thesis and a few suggestions for future work.

2. State of the Art

2.1. The importance of Renewable Energies

Energy can be arranged into two different groups: renewable (solar, wind, hydro, wave, geothermal, biomass) and non-renewable (coal, fuel, natural gas) sources.

Since the industrial revolution, in the 19th century, coal and oil grew to be the primary energy sources used to fill the energy needs of the modern society. However, with the energy crisis in 1973, oil prices greatly increased and western countries became aware of its limited availability and began a search for alternatives. This phenomenon can be observed in Figure 2-1 as well as the growth of energy consumption in the world by source. With this growing use of energy, it became clear that fossil fuels produce dangerous pollutants, like carbon dioxide, which accumulate in the lower layers of the atmosphere and can lead to air pollution, greenhouse effects and acid rain. All this can contribute to climate change and bring about floods, droughts and even animal extinction [4].

With the increase in environmental pollution, the potential depletion of fossil fuel resources and the growing energy demand, clean and renewable energy resources have become more appealing in recent years. Among these renewable resources – solar, wind, hydro, biomass, etc. – wind energy is found to be a cheaper alternative with a vast potential [5].

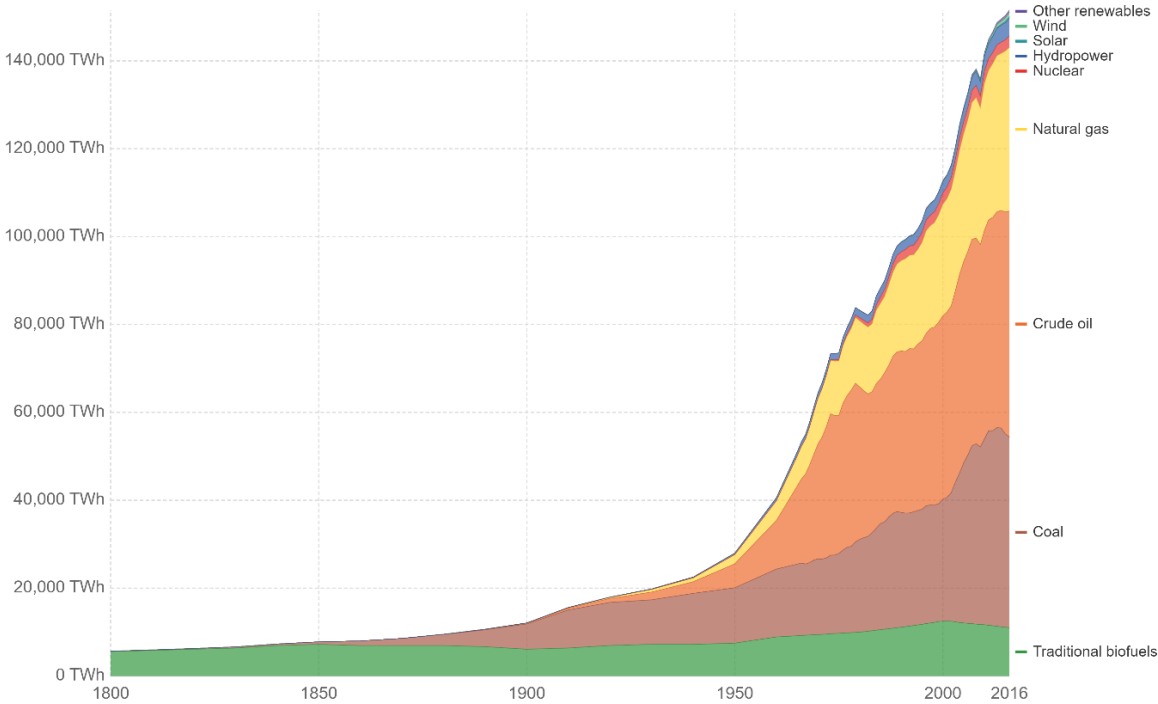


Figure 2-1 Global primary energy consumption by source, measured in terawatt-hours (TWh). Adapted from [6]

2.2. Wind Energy

Wind is air in motion; it is an indirect form of solar energy caused by an uneven heating of the earth's surface due to solar radiation. The wind flow patterns are affected and the masses of air are moved due to the irregularities of the earth's surface: terrain elevations, bodies of water and vegetative cover [7].

The wind energy potential on earth is vast: it has been estimated that there are around 10 million MW of energy incessantly available for harvesting [8]. Besides being a practically endless source of energy, it is clean, non-polluting and has a wide distribution around the world, thus becoming one of the best options for the planet's sustainable development and the global economy.

Nevertheless, there are some drawbacks to consider: despite the wide distribution, wind is an intermittent source, both geographically and temporally, and can, consequently, lead to periods with no energy production (due to low ($< 3 - 4 \text{ m/s}$) or extreme speeds ($> 25 - 30 \text{ m/s}$)) which requires the existence of storage systems and advanced calculation tools to help predict such speeds; The variation of said speed can also affect the quality of production of the electricity calling the need for compensation systems; Its low energy density requires operating several wind turbines – wind plants – which due to their huge size and height may cause visual impact, noise problems and can affect the surrounding ecosystems (mostly birds as a result of blade collision), though having minor environmental impact compared to fossil fuel plants [9].

Still, the power of the wind has been used for thousands of years. Sailboats first used the force of the wind on its sails to create drag to navigate the boat – the kinetic energy of the wind is transformed into kinetic energy of the boat. Windmills have been around since at least 900 AD and were commonly used to pump water or grind cereals. In this case, the kinetic energy of the wind is converted into mechanical power, translated to the rotation of a shaft – the concept of a common turbine. With the advances in technology, wind turbines were created to harness wind power and generate electricity.

The maximum available power in the wind is the mass flow through the propeller times the total kinetic energy of the wind that sweeps the propeller area. The maximum amount of power that is possible to harvest from the wind is dependent on the number of blades.

$$P_{avail} = \frac{1}{2} \dot{m} V_{\infty}^2 = \frac{1}{2} \rho_{\infty} A V_{\infty}^3 \quad (2.1)$$

Where ρ_{∞} is the undisturbed air density, A is the area of the surface through which the wind passes and V_{∞} is the undisturbed wind velocity. This equation shows the power in the wind is directly proportional to the cube of the wind speed. Therefore, it becomes imperative to assess the global availability and geographical distribution of wind as well as its speed. In Figure 2-2 it is possible to see there are some areas of the world where wind energy is a more attractive solution than others such as Argentina, Chile, Greenland, Iceland, Ireland, New Zealand and others [10]. Yet, it is also important to evaluate the topography and the influence of height of installation above ground for the selection of wind farms sites – one of the most substantial impacts on the environment is the visibility and aesthetics of wind turbines

as mentioned before. The ground relief and the presence of population present the biggest limitations to site selection, along with visibility. These plants usually take up large tracts of land and produce high levels of noise, leading energy companies to search for more remote places. Fortunately, current research is being developed towards handling and diminishing these problems.

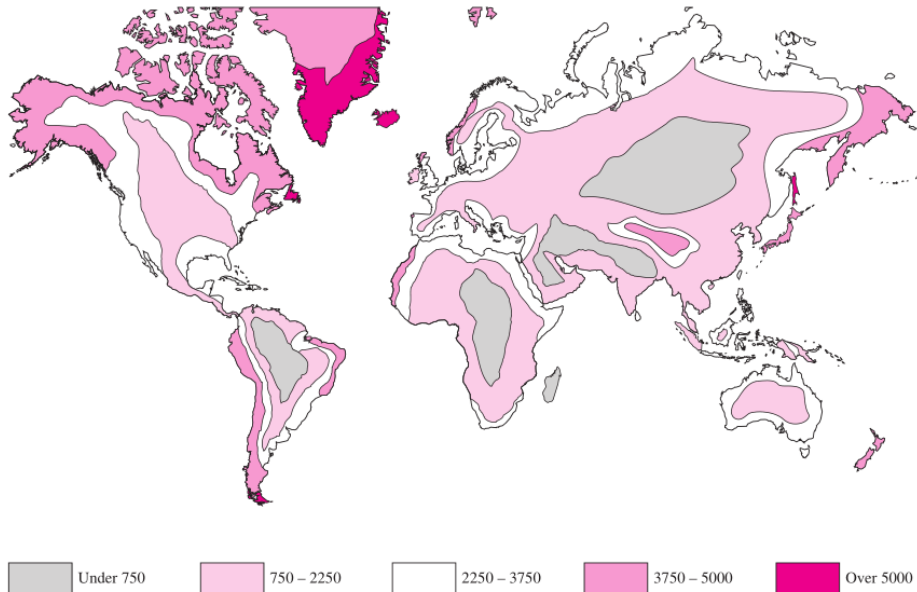


Figure 2-2 World availability of land-based wind energy: estimated annual electric output in kWh/kW of a wind turbine rated at 11.2 m/s. As in figure 11.33 from [10]

The world’s largest terrestrial turbines are roughly 200 m tall. In the areas where they are usually installed, topography, vegetation cover and ground thermic can affect wind density. In regions of higher altitude (relative to the ground) this influence is smaller, the wind becomes stronger and more consistent, with higher velocity magnitudes. As altitude becomes a determining factor in wind availability a new concept aiming to harvest wind at such heights starts to be developed – high-altitude wind energy [3]. In Figure 2-3 it is possible to compare wind speeds at typical heights for terrestrial turbines (120 m) and HAWC systems (600 m).

As seen before in (2.1), wind speed and power are related. Therefore, if wind speed increases with height one can state the wind power available will also increase. In Figure 2-4 it is possible to compare the average power density around the world for the same heights as before. Relating the two figures, Figure 2-3 and Figure 2-4, one can conclude the regions with highest speeds and greatest power density for bigger heights are North America, North and Eastern Europe and some areas of Antarctica. This shows, once again, the importance of site selection for harnessing the power of wind.

It is important to note that these kinds of values come from averages performed with data retrieved over the course of several years. Wind behavior can be very unpredictable over large scales of time; it can vary a lot from one year to the next, or even through decades. These long-term variations make accurate predictions difficult and make it harder to estimate the economic viability of wind plants. However, on shorter time scales (shorter than a year) temporal variability is more predictable [11].

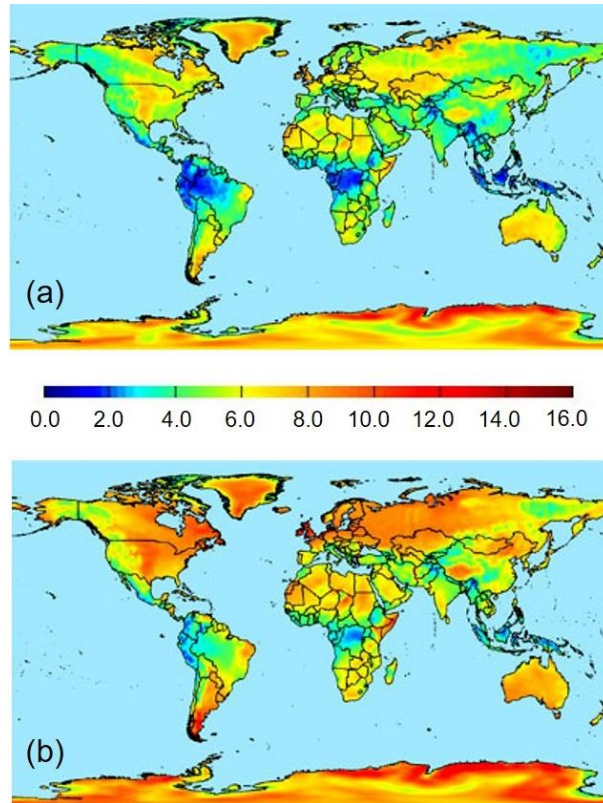


Figure 2-3 Average wind speeds in m/s at: (a) 120m; (b) 600m. Adapted from [12]

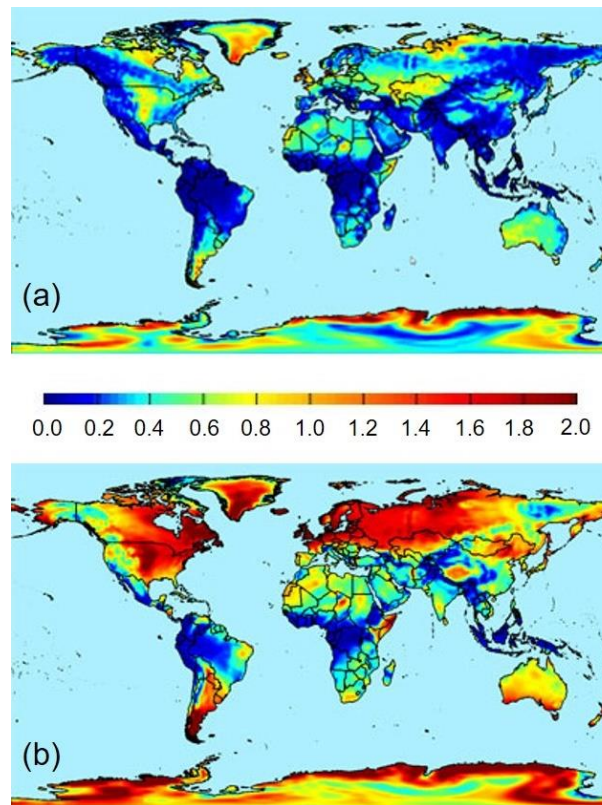


Figure 2-4 Average power density in kW/m² at: (a) 120 m; (b) 600 m. Adapted from [12]

2.3. Wind turbines

Wind turbines convert the kinetic energy of the wind into mechanical power which is in turn converted to electricity.

There are two main turbine concepts which are named after their axis of rotation: horizontal axis wind turbine (HAWT) with a horizontal shaft (Figure 2-5 (a)); vertical axis wind turbine (VAWT) with a vertical shaft (Figure 2-5 (b)) [13].

VAWT's were the first kind of wind turbine to be used to harvest the power of the wind; however, researchers initially believed this type of turbine was much less efficient than the HAWT thus focusing on the development of the latter. Nevertheless, research on VAWT's continued on a minor scale and, more recently, it was found that this concept is actually apt for generating electricity in conditions where HAWT's fail, such as high wind speeds and wind gusts. Due to their configuration, VAWT's produce less noise, are able to harvest wind from any direction and require no yaw system which results in fewer power losses. Another benefit of VAWT's is that since their generator is positioned on the ground, maintenance is easier. On the downside, these turbines have a larger blade area and are often non-self-starting, unlike HAWT's [5].

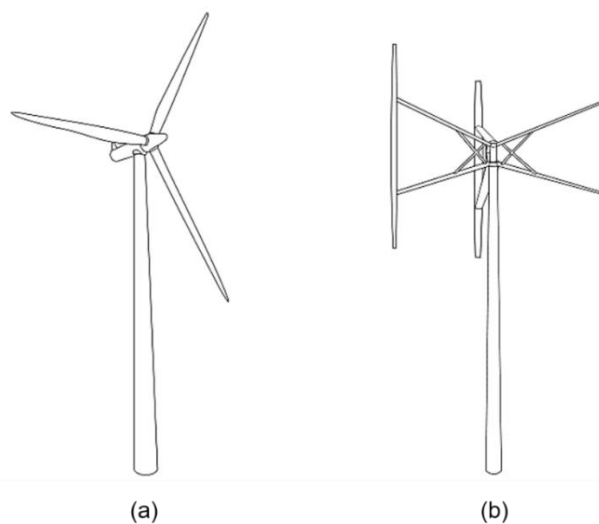


Figure 2-5 Visual comparison between the two wind turbine concepts denoted by the axis of rotation: (a) HAWT; (b) VAWT. Adapted from [13]

The maximum available power is given by equation (2.1). Using this, one can state the aerodynamic efficiency of an ideal frictionless turbine in terms of the power coefficient

$$C_p = \frac{P_{rotor}}{P_{avail}} = \frac{P_{rotor}}{\frac{1}{2}\rho_{\infty}AV_{\infty}^3} \quad (2.2)$$

Rearranging the equation, if the power coefficient is known, one can derive the power generated by a wind turbine when subject to a certain wind speed V_{∞}

$$P_{rotor} = \frac{1}{2} C_p \rho_{\infty} A V_{\infty}^3 \quad (2.3)$$

The power coefficient relates to the ratio between blade tip speed and wind speed, the Tip Speed Ratio (TSR), as in Figure 2-6,

$$TSR = \frac{\omega R_{tip}}{V_{\infty}} \quad (2.4)$$

Where ω is the rotational speed of the turbine and R_{tip} is the radius to the blade tip, which in case of a VAWT equals the radius of the turbine R_{tur} .

Figure 2-6 shows the measured power coefficient C_p as a function of TSR for several types of turbines. Keep in mind these are only average values since, for each type of turbine, there are different designs with different behaviors.

The ideal Betz number (≈ 0.59) is the maximum theoretically possible power coefficient considered for an ideal wind turbine, with an infinite number of blades, in ideal conditions – with homogeneous, incompressible, steady state fluid flow, no frictional drag, uniform thrust over the rotor area and a nonrotating wake. Real wind turbines cannot normally meet these conditions. Considering the rotation of the wake behind the rotor, one can obtain an amended, more detailed curve of the Betz limit – the ideal propeller type curve. The fact that a turbine has a finite number of blades with associated tip losses and that the aerodynamic drag is non-zero also contribute to the decrease in maximum possible power coefficient [14].

For any given turbine, the maximum power coefficient that it can enact during operation, $C_{P(max)}$, plays a significant role in the design of the turbine. Researchers like Kirke [15] defined a range of design TSR instead of a single point. Specifically, a range where the power coefficient remains higher than 70% of $C_{P(max)}$.

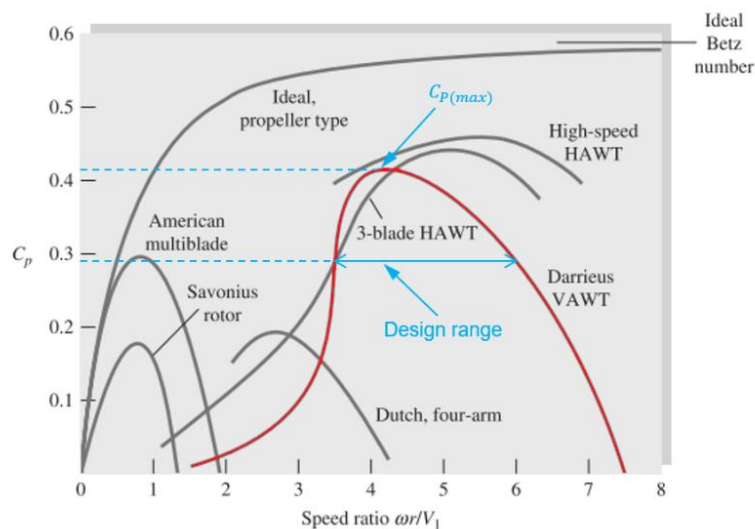


Figure 2-6 Estimated performance of various wind turbine designs as a function of blade Tip Speed Ratio. Adapted from [10]

Wind turbines have a typical power curve which can illustrate their four distinct operating regions, as in Figure 2-7. In region *I* the wind speeds are not sufficient for the turbine to generate power. Only when the wind reaches the cut-in speed V_{cut-in} does the turbine begin to generate power but only below rated values. At this point the turbine enters region *II*, the sub-rated power region. Here, theoretically, power production rises proportionally to the cube of wind speed until it reaches the rated speed V_{rated} . This means the wind is enough for the turbine to reach the rated output power which is approximately constant since it is limited by the turbine. In region *IV* there is no power production as the wind has reached the cut-out speed $V_{cut-out}$ and from this point forward the wind speeds are too high and can damage the structure of the turbine [16].

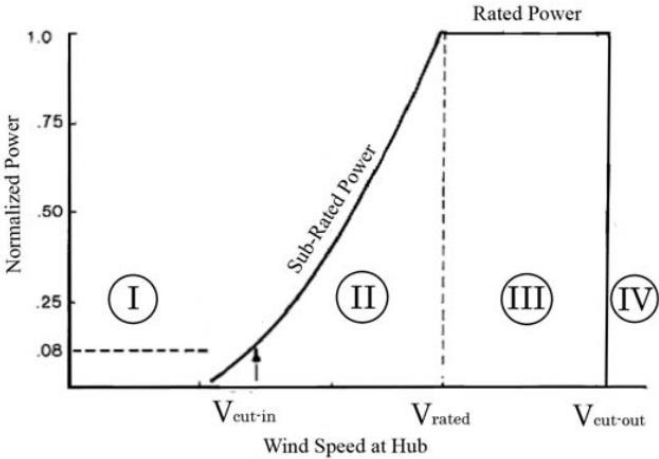


Figure 2-7 Typical power curve of a commercial wind turbine. As in [16]

2.3.1. Vertical Axis Wind Turbines

VAWT's can be divided into two categories according to the active force that propels the movement: drag and lift driven turbines. The aerodynamic drag is the component of the force parallel to the direction of the flow while the lift is the component of the force perpendicular to the flow [17]. Figure 2-8 represents the schematics for the main types of VAWT's.

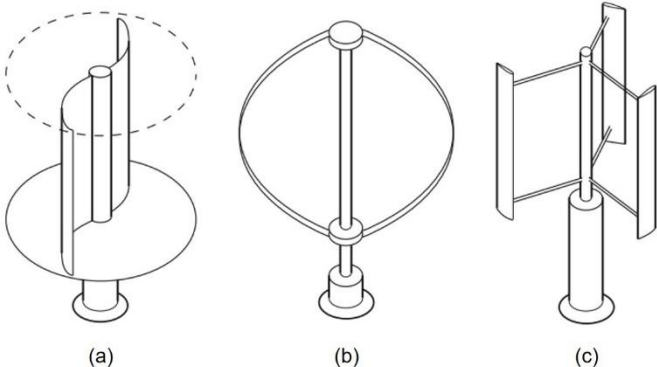


Figure 2-8 Types of Vertical Axis Wind Turbines: (a) Savonius rotor; (b) Darrieus rotor; (c) H-Darrieus rotor. Adapted from [18]

The Savonius rotor (Figure 2-8 (a)) is a drag-type turbine. It consists of two half-cylinder sections attached to a central shaft so that its cross-section forms an “S”. This way, one of the blades is moving against the wind and the other with it. Due to their curvature, the blade moving against the wind experiences less drag. The net torque required to rotate the turbine comes from the drag differential between the blades. All drag-type turbines work this way. Figure 2-9 illustrates a schematic of this process for the Savonius rotor [17].

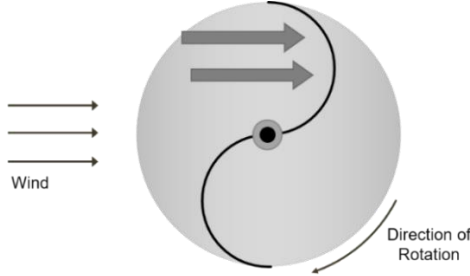


Figure 2-9 Top view schematic of a Savonius rotor. Adapted from [19]

Lift-type turbines have the aerodynamic lift as the active force that makes them turn – Darrieus turbines fit into this category. When a rotor is spinning, the blades move in a circular path in such a way that there are always blades upwind and downwind. This movement generates a lift force, greater than the resulting drag, pointing in an oblique direction which varies with the movement of the blade due to the variation in the angle of attack α (Figure 2-10), giving the necessary torque for rotation [19].

A typical Darrieus turbine like in Figure 2-8 (b) is called an eggbeater or phi-rotor due to its configuration – its two or more blades have a curvature that follows a Troposkien curve and are only attached to the shaft at the ends [10]. This allows for fewer bending stresses. A variation of this turbine is the H-Darrieus rotor (Figure 2-8 (c)), or Giromill or simply H-rotor, which is characterized by its straight vertical blades attached to the shaft through supporting arms. This turbine can have two ways of functioning – fixed-pitch and variable-pitch. The latter allows the blades to rotate around their own longitudinal axis, so it is possible to maintain the angle of attack constant consequently increasing the turbine’s efficiency. This construction is, however, more complex than the first [5].

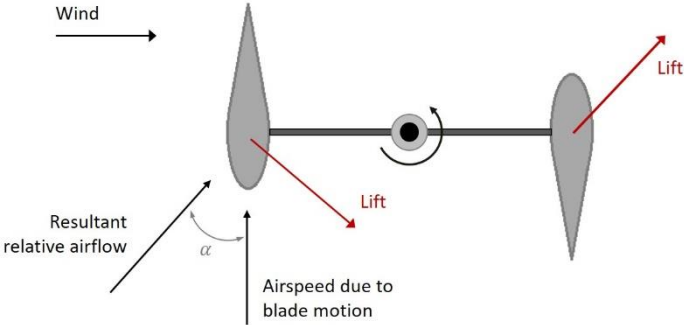


Figure 2-10 Top view schematic of a Darrieus rotor. Adapted from [19]

By understanding their functioning method, one can recognize that a drag-type turbine has less capability to harness the power of the wind than a lift-type turbine. For this reason, drag-type turbines are not typically used in commercial wind farms. Nevertheless, they are a good choice for urban environments, for a house, as they have a good capability to harness low wind speeds and have a good starting torque [17].

Regardless of the design, wind turbines can also be classified in two types according to rotational speed control – constant speed rotor or variable speed rotor. The first is designed, for a single chosen wind speed, to function at an optimum point and has been used in older models, when the generator is directly connected to the grid. The second, used in newer wind turbines, is designed to function at optimum conditions for each wind speed by adjusting the rotational speed [20].

In this thesis, the concept of a VAWT, with its axis normal to the wind flow, is applied to an airborne system – a cylindrical balloon – which is positioned in a horizontal position. This configuration does not follow the typical convention, so, to avoid confusion, it will be designated as a normal flow wind turbine (NFWT).

2.4. Aerodynamic characteristics of a lift type turbine

To further understand the behaviour of a NFWT it is important to recognise the variables involved, namely, velocities, forces applied and angles. Figure 2-11 presents the relevant velocity vectors and force components acting on a blade.

Note that these parameters are studied for the given wind speed direction and counter-clockwise blade rotation, where the position of the blade $\theta = 0^\circ$ matches the positive y-axis. These considerations are true for the remainder of the thesis.

According to [21], for a turbine with radius R_{tur} , the rotational movement of the blades is characterized by the rotational speed ω and each blade has a speed V_b , tangential to its revolving motion, given by

$$\vec{V}_b = \vec{\omega} \overrightarrow{R_{tur}} \quad (2.5)$$

This means the air motion relative to the blade will be $-\vec{V}_b$. This movement combined with a certain freestream wind speed \vec{V}_∞ results in each blade being subject to a relative velocity \vec{V}_{rel} . This velocity changes magnitude and direction according to the blade's position θ , observable in Figure 2-12. As will be seen ahead, the angle of attack α , between the relative velocity and the blade's chord line, also changes with the position θ .

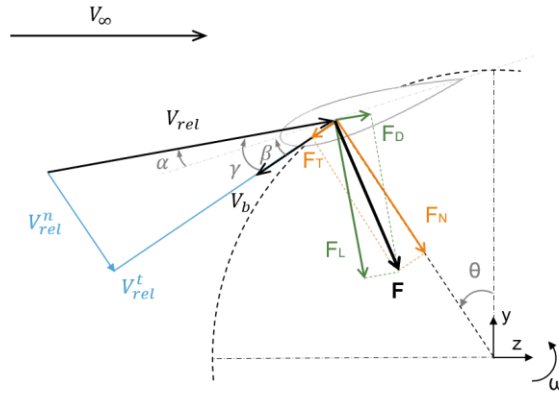


Figure 2-11 Definition of the force and velocity vectors. Adapted from [21]

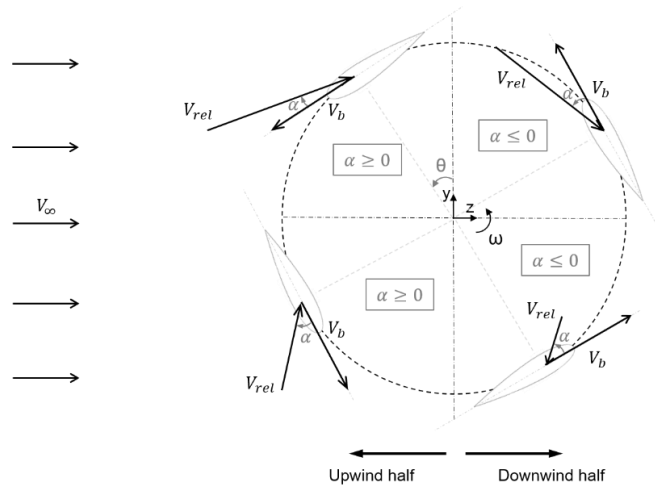


Figure 2-12 Parameters concerning one revolution. Adapted from [22]

From Figure 2-11 one sees that the relative velocity has a tangential and a normal component. Examining the vectors, each component can be computed as

$$V_{rel}^t = \omega R_{tur} + V_{\infty} \cos \theta \quad (2.6)$$

$$V_{rel}^n = V_{\infty} \sin \theta \quad (2.7)$$

The total magnitude of a blade's relative velocity is given by

$$V_{rel} = \sqrt{(V_{rel}^t)^2 + (V_{rel}^n)^2} \quad (2.8)$$

Using equations (2.6), (2.7) and (2.4) one gets

$$\begin{aligned} V_{rel} &= \sqrt{(\omega R_{tur} + V_{\infty} \cos \theta)^2 + (V_{\infty} \sin \theta)^2} = \sqrt{V_{\infty}^2 (TSR + \cos \theta)^2 + V_{\infty}^2 \sin^2 \theta} \Leftrightarrow \\ &\Leftrightarrow V_{rel} = V_{\infty} \sqrt{(TSR + \cos \theta)^2 + \sin^2 \theta} \end{aligned} \quad (2.9)$$

Figure 2-13 represents the evolution of the relative velocity of a single blade as a function of position θ , for different values of TSR , considering the freestream wind speed $V_\infty = 10 \text{ m/s}$. It is possible to see the relative velocity reaches a maximum for $\theta = 0^\circ$ or $\theta = 360^\circ$, when the blade's movement is aligned with the direction of the wind. The minimum is reached for $\theta = 180^\circ$, when the blade is moving against the wind. Knowing this, one can calculate the maximum and minimum values of the relative velocity

$$V_{rel,max}(\theta = 0^\circ, 360^\circ) = V_\infty(TSR + 1) \quad (2.10)$$

$$V_{rel,min}(\theta = 180^\circ) = V_\infty(TSR - 1) \quad (2.11)$$

Now, with (2.9), the local Reynolds number, as a function of θ , is computed as

$$Re = \frac{V_{rel}c}{\nu} = \frac{V_\infty \sqrt{(TSR + \cos \theta)^2 + \sin^2 \theta} c}{\nu} \quad (2.12)$$

Where c is the blade chord in meters and ν is cinematic viscosity of air considered $1.5 \times 10^{-5} \text{ m}^2/\text{s}$.

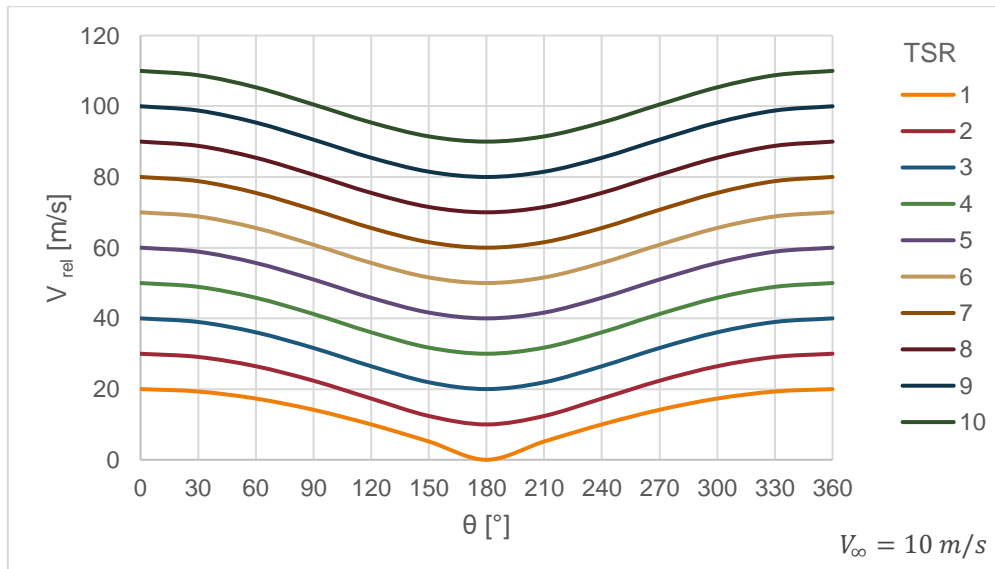


Figure 2-13 Relative velocity V_{rel} as a function of the position angle θ , for different values of TSR

The blade's local angle of the inflow γ , found between the relative velocity and the blade velocity, can be computed, from Figure 2-11, from the components of the relative velocity at each position,

$$\gamma = \tan^{-1} \left(\frac{V_{rel}^n}{V_{rel}^t} \right) \quad (2.13)$$

With equations (2.6), (2.7) and (2.4) the angle γ is calculated as

$$\gamma = \tan^{-1} \left(\frac{V_\infty \sin \theta}{\omega R + V_\infty \cos \theta} \right) = \tan^{-1} \left(\frac{\sin \theta}{\frac{\omega R}{V_\infty} + \cos \theta} \right) \quad (2.14)$$

$$\gamma = \tan^{-1} \left(\frac{\sin \theta}{TSR + \cos \theta} \right)$$

The blade incidence angle β is an input parameter of the rotor. The relationship between this angle and the angle of attack of the blade α is computed as in [21]

$$\alpha = \gamma - \beta \quad (2.15)$$

Substituting (2.14),

$$\alpha = \tan^{-1}\left(\frac{\sin \theta}{TSR + \cos \theta}\right) - \beta \quad (2.16)$$

This means the angle of attack is a function not only of the blade's position but also of the Tip Speed Ratio. Figure 2-14 represents the evolution of α for a single blade through one revolution. It is possible to notice that with the increase of TSR the variation of α becomes smaller. On the other hand, for lower TSR (approximately $TSR < 3$), α reaches values above the critical angle of attack where a blade is stalled and therefore produces less lift and smaller C_L . For $\theta = 0^\circ$ or $\theta = 360^\circ$ and $\theta = 180^\circ$, α is zero since the blade is moving in the direction of the wind.

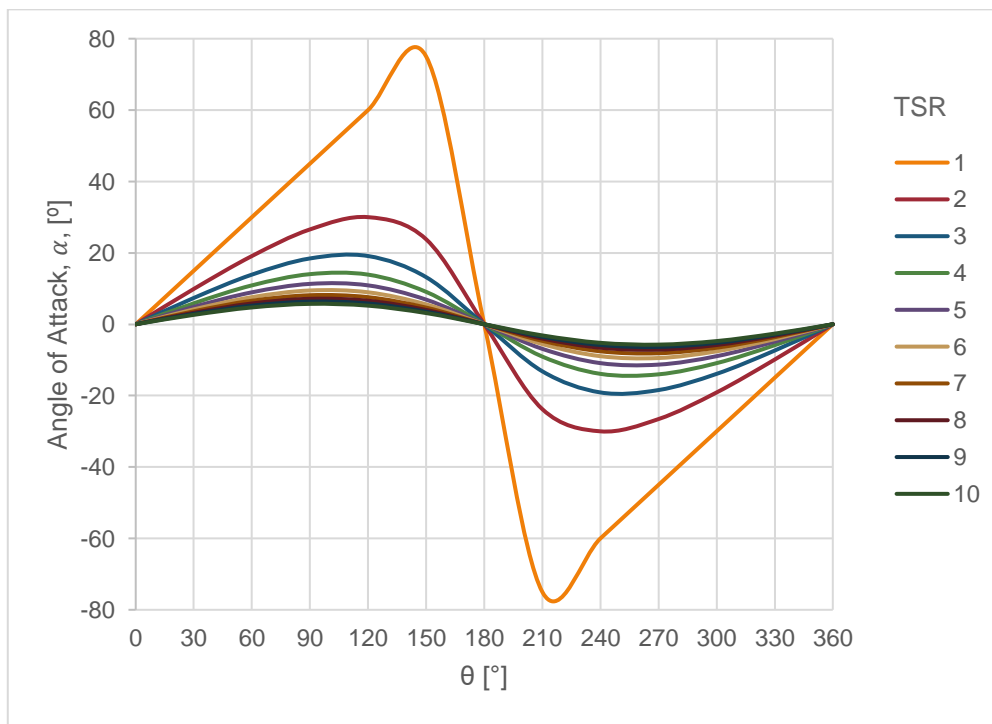


Figure 2-14 Angle of attack α as a function of the position angle θ , for different values of TSR

Figure 2-11 also shows the notations of the forces applied on a single blade. The net aerodynamic force F can be decomposed in two aerodynamic components: lift, F_L , perpendicular to the direction of the relative velocity and positive in the inward direction, for positive α ; and drag, F_D , parallel to the relative velocity and positive in the direction from the leading edge to the trailing edge. These two are defined through the lift and drag coefficients, C_L and C_D .

$$F = \sqrt{(F_L^2 + F_D^2)} \quad (2.17)$$

$$F_L = \frac{1}{2} \rho_{\infty} A_b V_{rel}^2 C_L \quad (2.18)$$

$$F_D = \frac{1}{2} \rho_{\infty} A_b V_{rel}^2 C_D \quad (2.19)$$

Where $A_b = c \cdot L_b$ is the blade area, with c being the chord of the blade and L_b its length. The aerodynamic coefficients can be obtained, for every position θ , for a given blade profile, from graphs that show the evolution of C_L and C_D as a function of α and the local Reynolds number Re .

The net force F can also be decomposed in two other components in the radial referential: F_N , the normal force, representing the structural loads on the blades, and F_T , the tangential force, gives the torque from the rotor [23]. These vectors can be expressed as a function of the aerodynamic forces and the local angle of inflow

$$F_T = F_L \sin \gamma - F_D \cos \gamma \quad (2.20)$$

$$F_N = F_L \cos \gamma + F_D \sin \gamma \quad (2.21)$$

Like the components of the relative velocity, the normal force is positive in the outward direction, and the tangential force is positive in the direction from the leading edge to the trailing edge.

Now, torque can be expressed as

$$T = F_T R_{tur} \quad (2.22)$$

And power can be calculated from the torque as

$$P = T \omega \quad (2.23)$$

The average power as a function of the position θ for one blade can be computed as

$$\bar{P}_1 = \frac{1}{2\pi} \int_0^{2\pi} P(\theta) d\theta \quad (2.24)$$

Using equations (2.22) and (2.23) the former develops as

$$\bar{P}_1 = \frac{1}{2\pi} \int_0^{2\pi} F_T(\theta) R_{tur} \omega d\theta \quad (2.25)$$

The total average power is obtained by multiplying (2.25) by the number of blades N_b

$$\bar{P} = \frac{N_b R_{tur} \omega}{2\pi} \int_0^{2\pi} F_T(\theta) d\theta \quad (2.26)$$

3. Concept Generation

As mentioned before, the goal is to apply the concept of a VAWT turbine to the existent airborne platform by *Omnidea* and improve it as a HAWT system. A product development method approach [24] was used to evaluate a few potentially viable designs for such a system in order to reach a final concept for design and testing.

3.1. Concept selection

As a first step, a few designs were drafted, based on pre-existing ideas by *Omnidea* and a brainstorming session with the company, for the concept that could perform the intended function.

Knowing the balloon has radius R_b , there are essentially three main concepts evaluated here that differ in balloon/blade configuration:

- One balloon with turbine blades around it, with radius $R > R_b$ – A, D
- Two balloons with turbine blades in between them with radius R_b – B, E
- One balloon with turbine blades on each side with radius R_b – C, F

Every pair of concepts has the same configurations and they differ in the type of blades – one has straight blades and the other curved blades, as illustrated in Figure 3-1. The type of blade has great relevance in terms of manufacturing, cost and sturdiness, so they are considered as separate concepts.

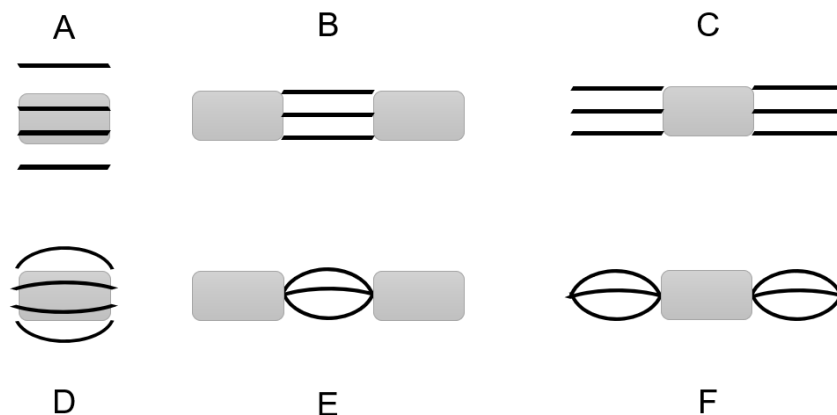


Figure 3-1 Schematics of each different concept

3.2. Decision Process

In order to start the decision process, the requisites deemed necessary were gathered from *Omnidea* and expressed in terms of “needs”, of *what* the product has to accomplish. These needs are stated in Table 3-1 and rated by relevance from 1 to 5, with 1 being “not relevant” and 5 being “very relevant”.

After defining each need and respective relevance, the next step is to contemplate each one and relate them to a specific metric and operational unit (Table 3-2), so that the product specifications can be evaluated. Each metric was also rated according to relevance.

Not all metrics have operational units associated. They may not be quantifiable, so they are evaluated on a subjective level. Other metrics work as a simple test where their value is pass/fail. These are listed as binary. Ideally, each need should correspond to its own metric, however, in practice this is typically not possible. The next tables show that a need can relate to more than one metric.

Table 3-1 List of needs

#	Need	Relevance
1	Must be able to endure strong winds	4
2	Minimum cost	5
3	Ease of maintenance	2
4	Ease of assembly	2
5	Ease of transport	2
6	Ease of manufacturing	4
7	Ease of landing/take-off	4
8	Starting torque capability	5

Table 3-2 List of metrics

# Metric	# Need	Metric	Relevance	Units
1	1	Sturdiness	4	Subj.
2	2	Production cost	5	€
3	3	Ease of maintenance	2	Subj.
4	3	Time to assemble/disassemble for maintenance	2	Days
5	3, 7	Ease of landing/take-off	4	Subj.
6	4	Ease of assembly	2	Subj.
7	5	Ease of transport	2	Subj.
8	6	Ease of manufacturing	4	Subj.
9	8	Torque	5	Binary

A couple other specifications turned up while brainstorming with *Omnidea* that were deemed more appropriate as project design specifications rather than needs so they are not contemplated in these tables.

Next, a needs-metrics matrix, Table 3-3, is constructed to represent, in a more visual way, the relationship between the needs and the metrics.

Table 3-3 Needs-metrics matrix

	Metrics	Sturdiness	Production cost	Ease of maintenance	Time to assemble/disassemble for maintenance	Ease of landing/take-off	Ease of assembly	Ease of transport	Ease of manufacturing	Torque
Needs	1	2	3	4	5	6	7	8	9	
Must be able to endure strong winds	1	X								
Minimum cost	2		X							
Ease of maintenance	3			X	X	X				
Ease of assembly	4						X			
Ease of transport	5							X		
Ease of manufacturing	6								X	
Ease of landing/take-off	7					X				
Starting torque capability	8									X

3.3. Concept Screening

To perform the selection of the better suited design, a decision matrix is used. It consists of a concept scoring matrix where each need was attributed a weight, according to relevance, and each concept was rated qualitatively in performance from 1 (poor) to 6 (great) in respect to each need – Table 3-4. In terms of cost, a higher rating means a lower cost.

These ratings are usually done comparatively to a reference design. In this case, however, there is no reference since for this kind of product the solutions are only comparable to each other.

Going through some of the decisions, in terms of cost it was considered that curved blades are a lot more expensive than straight blades; having two balloons instead of one is costlier as is having more blades. In terms of manufacture the reasoning was similar.

Regarding the ease of maintenance, it was considered that concepts A and D would be easier to access for maintenance.

Having blades between two balloons (B and E) was thought to be more difficult to assemble, due to access, than concepts C and F. Due to their size, concepts A and D were considered even more difficult.


The ratings for ease of landing and take-off were related to the size of the different concepts.

The ease of transport was mainly related to the length of each different concept, the possibility of carrying the prototype disassembled and the extra care with curved blades.

Regarding the strong winds issue, curved blades have better stress distribution due to their geometry, as mentioned before, so they are considered “tougher” and having two balloons was considered more hazardous.

From these matrices it is possible to see that a few concepts have received comparable scores; however, concept A has the highest score, which agrees with what the team believed to be the best concept *a priori*.

Table 3-4 Concept Scoring matrix



Selection criteria	Weight (%)	A		B		C		D		E		F	
		Rating	Weighted score	Rating	Weighted score	Rating	Weighted score	Rating	Weighted score	Rating	Weighted score	Rating	Weighted score
Must be able to endure strong winds	14.3	5	0.71	2	0.29	3	0.43	6	0.86	2	0.29	4	0.57
Minimum cost	17.9	5	0.89	4	0.71	3	0.54	2	0.36	2	0.36	1	0.18
Ease of maintenance	7.1	5	0.36	4	0.29	4	0.29	5	0.36	4	0.29	4	0.29
Ease of assembly	7.1	3	0.21	4	0.29	5	0.36	2	0.14	4	0.29	5	0.36
Ease of transport	7.1	5	0.36	3	0.21	4	0.29	4	0.29	3	0.21	3	0.21
Ease of manufacturing	14.3	6	0.86	5	0.71	4	0.57	3	0.43	2	0.29	1	0.14
Ease of landing/take-off	14.3	3	0.43	5	0.71	5	0.71	3	0.43	5	0.71	5	0.71
Starting torque capability	17.9	5	0.89	4	0.71	4	0.71	3	0.54	2	0.36	3	0.54
Total	100.0	--	4.71	--	3.93	--	3.89	--	3.39	--	2.79	--	3.00

4. Conceptual Design and Parameters

4.1. Design methodology

The first step in the design of a wind turbine is to specify the desired rated power. Next, based on the initial balloon concept, an optimum turbine diameter is calculated, and the rated rotational speed is computed. Subsequent key design parameters and topology are chosen and fixed, preferably within their optimum range, so that the turbine’s length can be calculated. Site conditions are also needed. As stated previously, wind is a variable source and knowledge of the intended site of operation is important. The wind conditions will dictate the loads on the system. With the design load cases estimated, the components can be designed to withstand said cases.

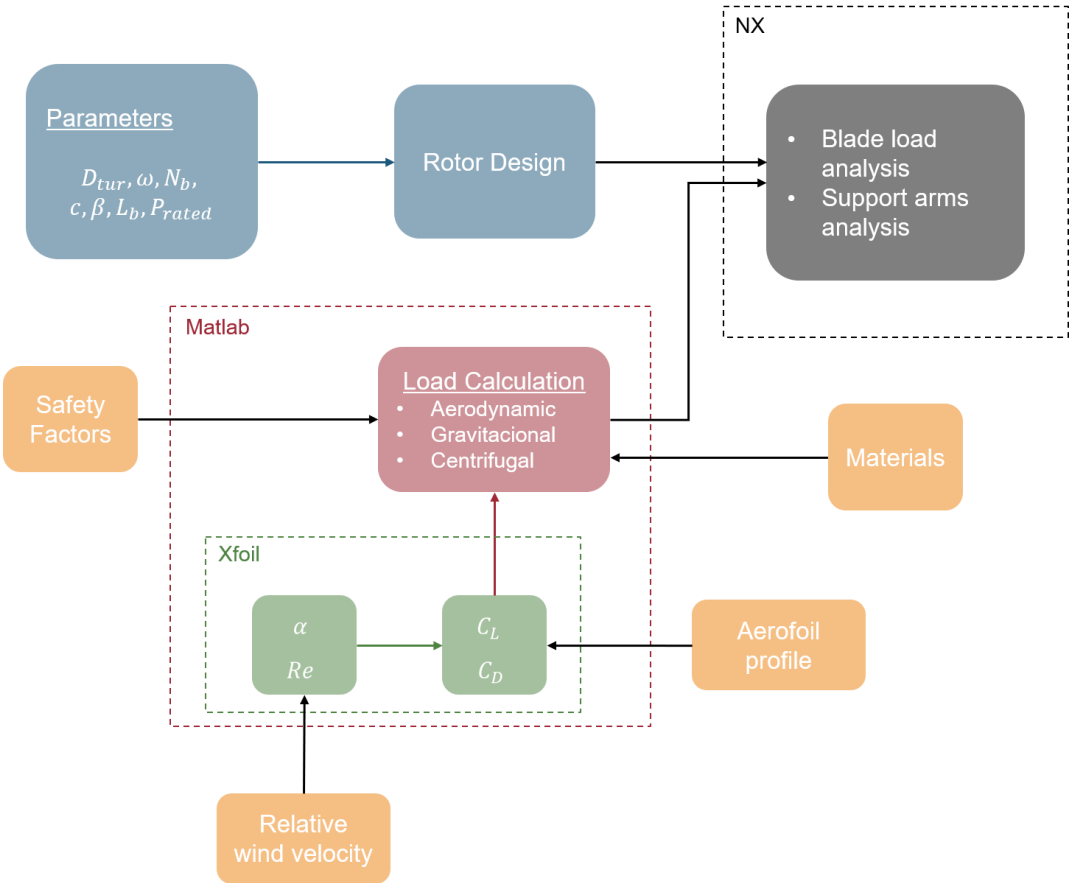


Figure 4-1 NFWT concept design process

4.2. Description of the concept

The selected concept for design, concept A, consists of one balloon with straight turbine blades around it. Per the company’s request, the turbine will be designed to fit the already existing balloon which has a length of 18 metres and a diameter of 3.8 metres.

Starting with the existing platform, the initial design structure consists of supporting arms attached to the blade's ends and connected to the balloon's side rims, as depicted in Figure 4-2. According to the length of the blades, one or more supports along the length might be necessary.

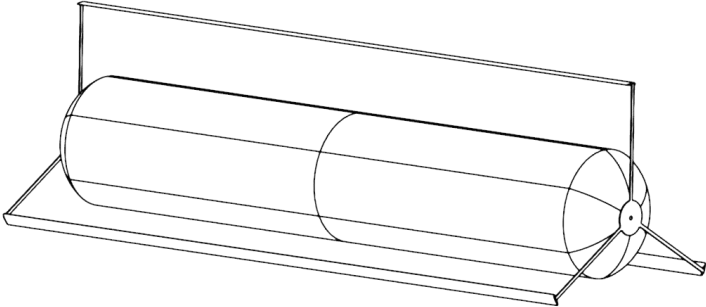


Figure 4-2 Initial concept design

4.3. Control Mechanism

This turbine will be a variable speed rotor. For a given wind speed, the rotational speed will be adjusted according to the optimum point of operation of the turbine. A way to accomplish this is with a controller unit, a power converter will regulate the generator output so as to adjust to the ideal rotational speed [25]. Following this strategy, and to achieve this control, three operation cases can be defined: parked, pre-rated and post-rated. These are defined in Table 4-1.

Table 4-1 Operation cases and corresponding conditions

Operation Case	Minimum wind speed	Maximum wind speed	Condition	Control Variable
Parked	0	V_{cut-in}	No rotation	$\omega = 0$
Pre-rated	V_{cut-in}	V_{rated}	Constant $C_p = C_{p,max}$	$\omega = \frac{TSR_{C_{p,max}} V_{\infty}}{R_{turb}}$
Post-rated	V_{rated}	$V_{cut-out}$	Constant $P = P_{rated}$	$\omega = \frac{TSR_{C_p(V_{\infty})} V_{\infty}}{R_{turb}}$

4.4. Design Values and Parameters

4.4.1. Wind speed distribution

Estimation of wind resource characteristics helps to determine the performance of a wind turbine at a given site. Statistical analysis of this resource can help understand its variability over time and allow for estimation of the wind energy output at that site.

The project team from *Omnidea* verified that the most frequent wind speed, V_{mf} , on the site of operation is 10 m/s. However, no other information on the wind distribution is given.

According to [11], the Weibull distribution is considered a good representation of the variation in hourly mean wind speed over a year (or several) in several sites. It can be given by the probability density function,

$$f(V) = k \frac{V^{k-1}}{a^k} \exp \left[- \left(\frac{V}{a} \right)^k \right] \quad (4.1)$$

k is the shape factor, usually chosen between 1 and 3, knowing that higher k means a sharper peak in the curve and so a smaller wind speed variation. As stated by [26], for the region of the site of operation of the turbine the shape factor can be set to $k = 2$. This is in fact a special case of the Weibull distribution as it corresponds to the Rayleigh distribution, which is a fairly typical value for many locations.

a is the scale factor. To determine a one can turn to V_{mf} . Finding the derivative of the Weibull distribution as a function of V and equaling it to zero, one finds the tangent to the maximum inflection point

$$\frac{df(V)}{dV} = 0 \Rightarrow V_{mf} = a \left(1 - \frac{1}{k} \right)^{\frac{1}{k}} \Rightarrow a = 10\sqrt{2} \quad (4.2)$$

Finally, the distribution comes as

$$f(V) = \frac{V}{100} \exp \left[- \frac{V^2}{200} \right] \quad (4.3)$$

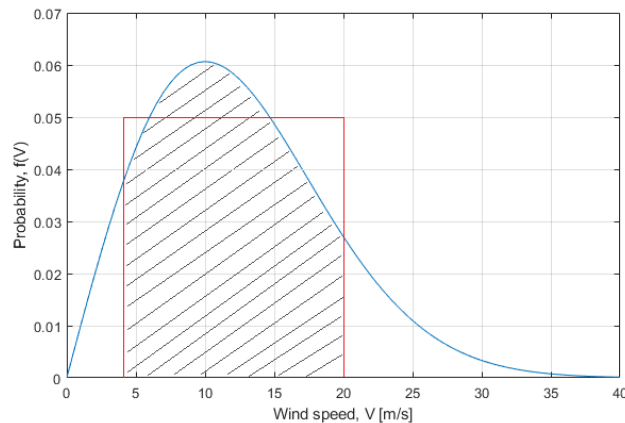


Figure 4-3 Probability distribution for the site of operation

Setting $V_{cut-out} = 20 \text{ m/s}$, a typical value for these turbines, for a work time of around 80%, it is possible to obtain V_{cut-in} with the inverse of the distribution. This leads to $V_{cut-in} = 4 \text{ m/s}$. Figure 4-3 shows the correspondent the traced area.

4.4.2. Diameter and Rotational speed

To maximize the lifting power of the platform, it is advantageous to get the most lift out of the balloon. Greater lift will lead to higher altitudes which means higher wind velocities and more power.

The characteristics of a flow around the balloon, a cylinder device that uses the Magnus effect, are mainly dependent on the Reynolds number and the spinning ratio X [27]

$$X = \frac{\omega R}{V_{\infty}} \quad (4.4)$$

The magnitude of the lift and drag forces and the friction torque are also dependent on said numbers. Sedaghat [28] introduced a correlation for the lift to drag ratio of rotating circular cylinders as a function of the spinning ratio,

$$\frac{C_L}{C_D} = \frac{-0.01355 - 0.4065 \times X + 1.2944 \times X^2 + 0.2249 \times X^3 - 0.09632 \times X^4}{1.0631 - 0.9137 \times X + 0.4694 \times X^2} \quad (4.5)$$

The lift and drag coefficients are expressed as

$$C_L = \frac{F_L}{\frac{1}{2} \rho_{\infty} A V_{\infty}^2}, \quad C_D = \frac{F_D}{\frac{1}{2} \rho_{\infty} A V_{\infty}^2} \quad (4.6)$$

Where F_L and F_D are, respectively, the lift and drag forces, ρ_{∞} is the undisturbed air density, A is a reference area defined from a given cylinder section and V_{∞} is the freestream wind speed.

Figure 4-4 (a), on the left, represents correlation (4.5), compared with experimental work [29] and numerical results of [30]. Figure 4-4 (b) shows the variation of C_L and C_D with the spinning ratio X . The region with higher lift is in the region of greater spinning ratio; however, this is not the region with best performance, since it also means higher values of drag which can be unfavorable. On the other hand, thinking of the spinning cylinder in the air attached to the ground by a cable, higher X leads to higher rotational speeds, which means that the cable will be stretched at a lower angle (with the ground) and, for the same cable length, the altitude reached will also be lower. Ergo, the optimum spinning ratio is a compromise between the two factors – higher lift and lower rotational speed. This way, the value of optimum spinning ratio is estimated to be at the peak of the curve, where $X \approx 2$.

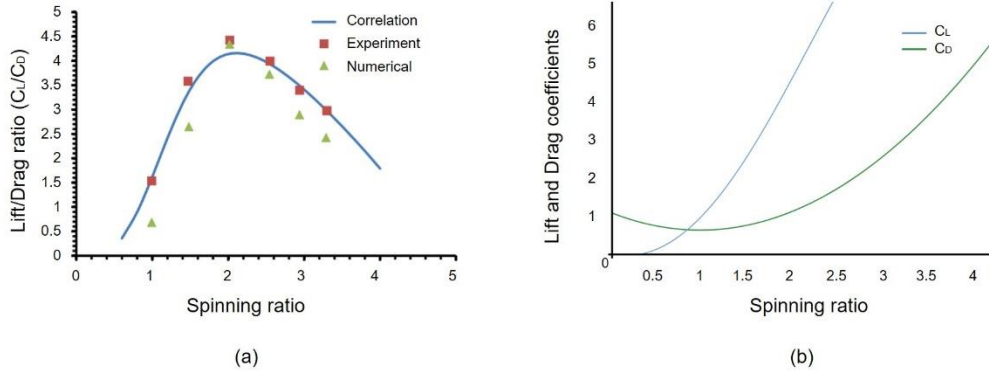


Figure 4-4 (a) Lift to drag ratio as a function of spinning ratio. Adapted from [28]; (b) Lift and drag coefficients as a function of spinning ratio

When dealing with a turbine, the previous ratio is adopted and referred to as Tip Speed Ratio (TSR) – the relation between the turbine blade tip speed and the wind speed [13], as stated in equation (2.4). As mentioned before, since a VAWT is being designed and not a horizontal axis turbine, every point of the blade is at the same distance from the rotor axis, so one can state R_{tip} simply as R_{tur} and get

$$TSR = \frac{\omega R_{tur}}{V_{\infty}} \quad (4.7)$$

In Figure 4-5, one gets, for a typical Darrieus VAWT, that the maximum value for the power coefficient is found for $TSR \approx 4.2$.

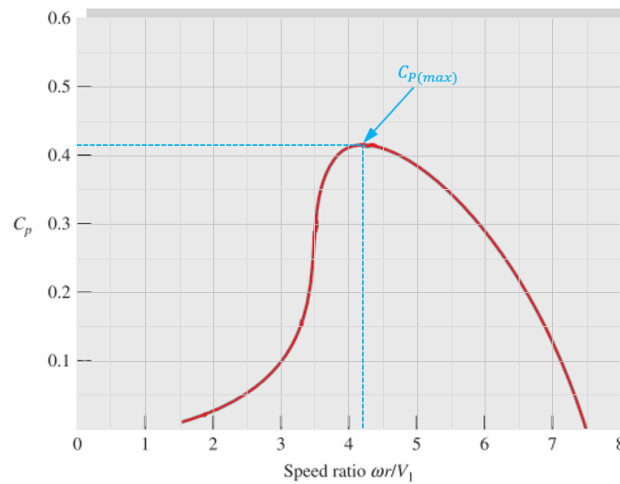


Figure 4-5 Performance curve of a typical Darrieus VAWT. Adapted from [10]

Therefore, for the same freestream wind speed, V_{∞} , and considering that both the balloon and the turbine will have the same angular velocity ω , it is possible to relate the two ratios and find the ideal distance between the blades and the Magnus cylinder to obtain the best performance,

$$\omega_{cyl} = \omega_{blade} \Rightarrow 2 \frac{V_{\infty}}{R_{cyl}} = 4.2 \frac{V_{\infty}}{R_{tur}} \Rightarrow R_{tur} = 2.1 R_{cyl} \quad (4.8)$$

Knowing, from *Omnidea*, that the balloon has a fixed diameter of 3.68 m one can find the diameter of the turbine rotor by applying the relation found previously,

$$D_{tur} = 2.1D_{cyl} \Rightarrow D_{tur} = 2.1 \times 3.68 \approx 7.7 \text{ m} \quad (4.9)$$

Again, from Figure 4-5, the maximum power coefficient for a Darrieus VAWT is, approximately, $C_{p,max} = 0.416$, for $TSR = 4.2$. For a wind speed of $V_{\infty} = 10 \text{ m/s}$ one gets, from equation (4.7), that the nominal rotational speed should be $\omega \approx 104 \text{ rpm}$. It should be noted that the rotational speed is an important design parameter since it relates to the structural integrity of the rotor. This is because, for a certain mass m of one blade, the centrifugal forces are proportional to the square of the rotational speed

$$F_c = mR_{tur}\omega^2 \quad (4.10)$$

4.4.3. Blade Number

When choosing the number of blades, one needs to consider the balance between the turbine's aerodynamic efficiency and the blade's stiffness. The choice must be efficient but also feasible which the optimum option is sometimes not.

Straight vertical axis wind turbines (S-VAWT) can be found with one, two, three or more blades. Figure 4-6 has the power coefficient C_p as a function of TSR for different blade numbers. Here it can be seen that the peak of power coefficient is moving to lower values of TSR and decreasing with the increase of blade number, for N greater than 2. The range of design TSR also decreases with the increase in blade number, as the performance curves become sharper.

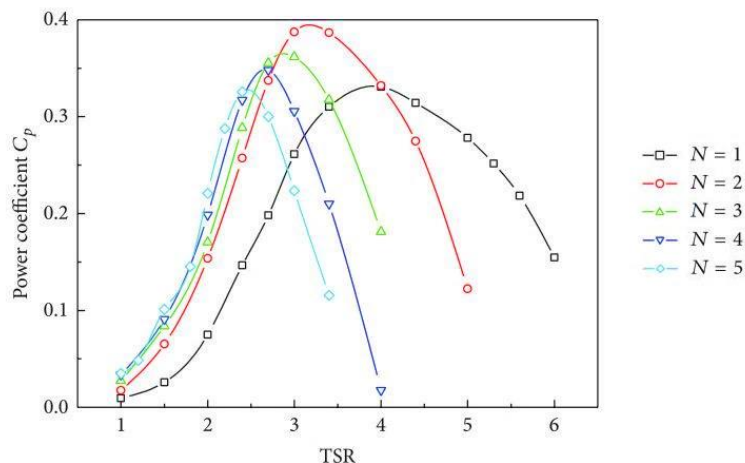


Figure 4-6 Relationship curves between power coefficient and blade number. As in [31]

The curve $N = 2$ presents the higher range of design TSR and higher $C_{p,max}$. However, before making a definitive choice, there are other factors to consider. The blades in a NFWT are subject to aerodynamic forces that vary with the angle of attack α which in turn varies with the position θ as in Figure 2-13. This

cyclic variation in both the magnitude and direction of the net force and the torque can induce resonance in the turbine [32]. The net aerodynamic force F , as per equation (2.17), is the vector sum of lift and drag, which are function of V_{rel} , which, in turn, is a function of θ . Knowing this, one can qualitatively analyse how the force on the centre shaft will vary with the position – Figure 4-7. The figure shows that 3 blades will peak three times while 2 blades only peak twice during a revolution. This means 3 blades will produce more fatigue cycles; however, even if the mid-range force is higher, the alternating forces are lower – less amplitude – which means the forces acting upon the structure are steadier and less prone to sudden variation. Another advantage of having three blades is their better self-starting capability compared to a two-bladed rotor [31].

Therefore, three blades were chosen for this case.

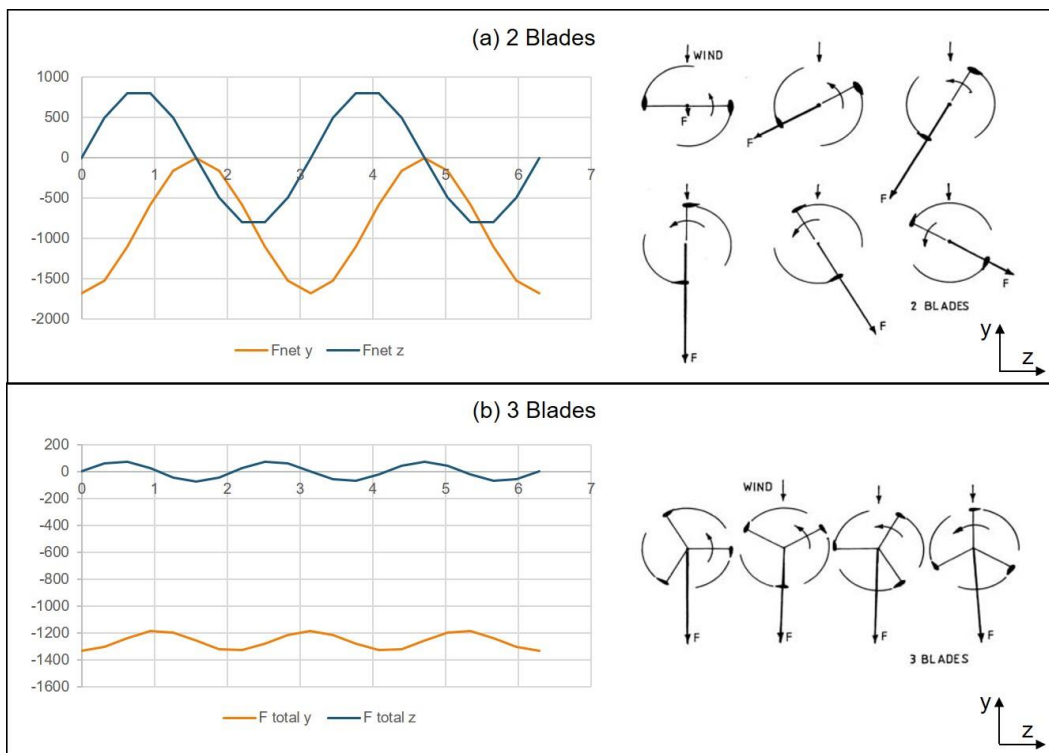


Figure 4-7 Variation of components y and z of net aerodynamic force with θ on 2 (a) and 3 (b) bladed NFWT

4.4.4. Solidity and blade chord

Solidity is one of the main design parameters of a turbine rotor. It is the measure of percentage of solid area in a circle traced by the rotor

$$\sigma = \frac{\text{blade area}}{\text{rotor frontal area}} = \frac{N_b c L_b}{D_{tur} L_b} \quad (4.11)$$

This parameter depends on the blade number N_b , the chord c and the turbine's diameter D_{tur} or, more commonly, its radius R_{tur} [20]. The latter is the most common convention in the literature and is the one chosen for this thesis.

$$\sigma = \frac{N_b c}{R_{tur}} \quad (4.12)$$

From the formula it is possible to deduce that with higher solidity the weight and, subsequently, the manufacturing costs will increase. As a design parameter, it is also possible to relate the solidity with the efficiency of the turbine and thus with C_p and TSR. Figure 4-8 is a result from the numerical model by Ahmadi-Baloutaki et al [20]. This model was performed for an S-VAWT with three NACA0015 blades and a free-stream Reynolds number of 170 000 and they found the same results and trends in other studies which make the model acceptable for this wind turbine.

Looking at Figure 4-8, the maximum power coefficient increases with the increase in solidity up to $\sigma = 0.4$. Beyond this point it decreases with the increasing solidity. Also, the range of design TSR becomes smaller with increasing σ . Knowing this, it is reasonable to assume that the optimum solidity factor lies somewhere between 0.2 and 0.6 where one has the highest values of maximum power coefficient.

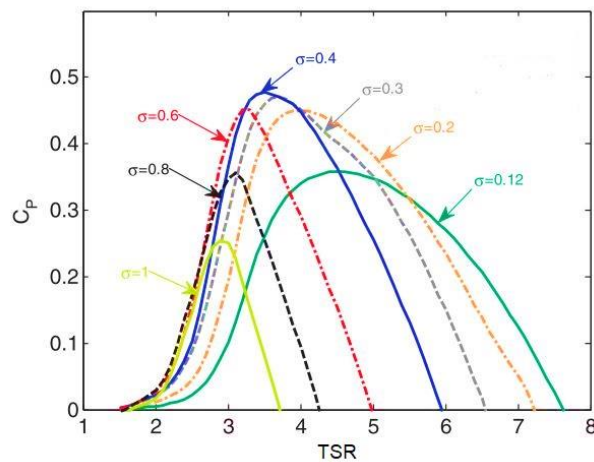


Figure 4-8 Performance curves of S-VAWT for different values of σ . Adapted from [20]

Allying a higher design range of TSR and a high $C_{P(max)}$ with the fact that higher solidity will mean more weight, the value of solidity chosen for this turbine will be $\sigma = 0.3$ as this value is expected to be relatively close to optimum.

The value for the aerofoil chord follows from the solidity as

$$c = \frac{\sigma R_{tur}}{N_b} \quad (4.13)$$

So, in this case, the blades will have $c \approx 0.39 \text{ m}$.

4.4.5. Blade incidence angle

The blade's incidence angle β , sometimes called pitch angle, is a very important factor for performance enhancement since, as seen previously in section 2.4, it relates to the angle of attack of the blade. It can also enhance the lift, an important factor for the balloon flight ability.

Figure 4-9 shows multiple curves of power coefficient of S-VAWT's for different blade incidence angles. A negative angle is out-offset and usually improves the aerodynamic performance. A positive angle is in-offset and has an adverse influence on performance [31]. Observing the figure, it is possible to see that $\beta = -4^\circ$ shows the highest value of $C_{P(max)}$ and the higher range of design TSR , making it a good choice for the turbine.

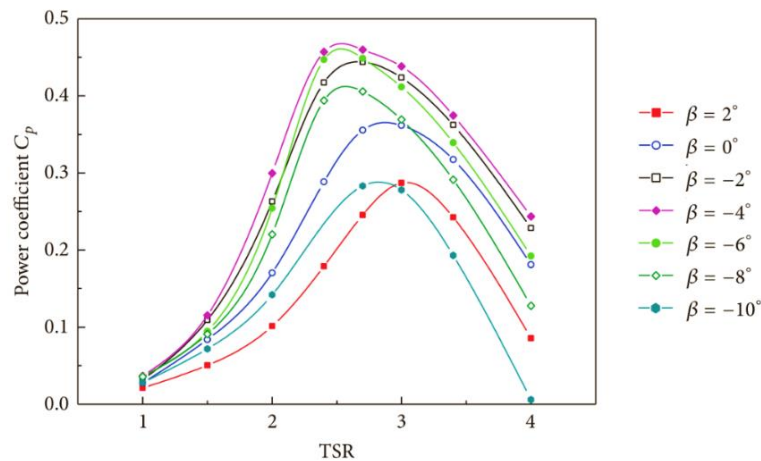


Figure 4-9 Relationship curves between power coefficient and blade incidence angle. Adapted from [31]

4.4.6. Blade profile

A blade's cross-sectional profile is one of the key aspects for an efficient wind turbine design. There are many different aerofoil profiles that can be divided in mainly two categories: asymmetric and symmetric aerofoils.

Asymmetric profiles have non zero lift at zero angle of attack, unlike symmetric profiles, and so have a better ability to self-start. However, the closer a profile is to symmetric the greater its power output will be. Symmetrical profiles do not need to readjust to wind direction since they produce aerodynamic lift from both sides of the aerofoil throughout a complete revolution of the rotor [20]. This is why they are so popular in VAWT design. Their ease in manufacturing is also a great advantage as it usually means lower costs.

Due to these reasons and the ready availability of the NACA00XX symmetrical profiles performance data, only these will be considered for this project.

The thickness of a NACA aerofoil is given by a percentage of the chord, given by the last two numbers of the profile's designation. The most commonly used NACA symmetrical aerofoils range thickness

between 12% and 21%. Figure 4-10 shows that profiles with relative thickness (RT) of 15% and 18% have the highest lift-drag ratio and a wider range of high lift-drag ratio, indicating these as preferred profiles. Larger thickness means higher blade stiffness and improves both the blade’s ability to self-start and its power coefficient; nonetheless, it also means potentially more weight and a drag penalty [31].

Knowing this, the NACA0018 profile seems to be a good choice for the turbine design. However, a fluid dynamics study should be performed to better understand more the differences in profile choice in the turbine’s efficiency.

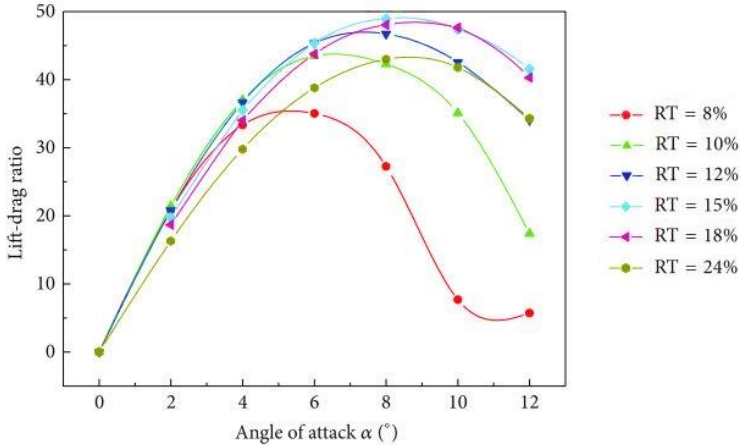


Figure 4-10 Curves of lift-drag ratio of symmetric aerofoils at various relative thickness. Adapted from [31]

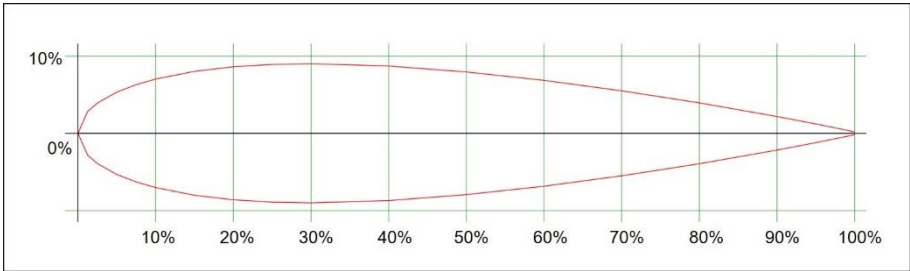


Figure 4-11 NACA0018 aerofoil characteristics by percentage of chord

4.4.7. Rated power and rotor length

One request from *Omnidea* is that the turbine should have a rated power between 10 and 20 kW. Since the balloon has 18 metres in length, that should be the maximum permissible length for the turbine’s blades.

It has already been stated that wind is a variable source, so it is best to design the turbine for the most frequent wind velocity. As seen in section 4.4.1, the maximum power coefficient is $C_p = 0.416$ for $TSR = 4.2$ and the design rotation speed can be calculated by rearranging equation (4.7) which gives $\omega \approx 104 \text{ rpm}$. Next, knowing $\rho_\infty = 1.225 \text{ kg/m}^3$, with C_p , the necessary blade length L_b is computed (Table

4-2) for a given rated power P_{rated} from equation (2.3) where the swept area A is $L_b D_{tur}$. The results displayed in the table show that the blades will be, for certain, shorter than the balloon.

$$L_{b,i} = \frac{2P_{rated,i}}{C_p \rho \omega D_{tur} V_{mf}^3} \quad (4.14)$$

Table 4-2 Computed values of L_b

P_{rated} [kW]	10	12	14	15	16	18	20
L_b [m]	5.1	6	7.1	7.6	8.2	9.2	10.2

5. Mechanical Design

5.1. Description of the updated concept

In light of the developments from the previous chapters, it is known that the blades will be shorter than the balloon so there is a need to update the previous design from Figure 4-2. Instead, the blades will be connected through the supporting arms to the balloon's outer net. Figure 5-1 shows a schematic view of the updated airborne system.

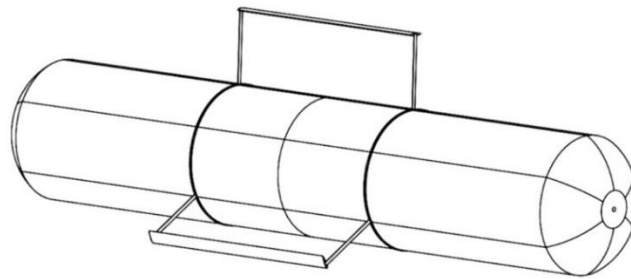


Figure 5-1 Updated concept design

5.2. Materials

When designing a wind turbine, material selection is one of the most important aspects to consider. The blades of a wind turbine are subject to great stresses, varied load conditions, centrifugal forces and a considerable number of fatigue cycles.

5.2.1. Balloon net and guy-wires

To provide stiffness and prevent the balloon from bending due to the ground tether cable force, *Omnidea* covered the balloon with a net made of high-modulus polyethylene (HMPE) rope – commercially known as *Dyneema* – which will also be used for the guy-wires. The rope properties described in Table 5-1 are for *Dyneema sk75*, the rope used by *Omnidea*. However, these are not enough to describe the material in the simulations ahead. The necessary tensile properties, namely the stress-strain curve, were only found for *Dyneema sk76*, which is a very similar grade [33].

Table 5-1 Properties of Dyneema sk75. From [34]

Property	Unit	Value
Modulus	GPa	113
Tenacity	GPa	3.4
Breaking force	N	610
Elongation	%	3.5

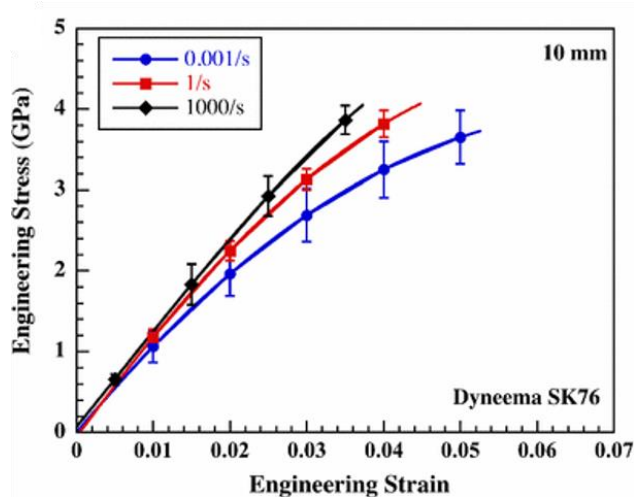


Figure 5-2 Stress-strain response of a Dyneema sk76 rope at multiple strain rates. From [33]

5.2.2. Blades

Ideally, the chosen material should combine the required structural properties to resist fatigue and centrifugal forces due to rotation, with lower cost, lower weight and the ability to be shaped into the selected aerofoil. Important requirements include high yield strength, high stiffness and low density. Depending on size and application, wind turbine blades are generally made from wood, aluminium or composite materials like glass or carbon fibre reinforced polymers (GFRP and CFRP). The first two are generally used on smaller blades and urban applications while the other are becoming more popular in wind turbine manufacturing.

In this case, one of the most important aspects of the chosen material is its density. Since this turbine will be airborne, lowering its weight is a crucial goal of the project. Composite materials show more favourable strength-to-weight ratios when compared to the other materials mentioned before and thus are a more appropriate choice for constructing the blades.

The manufacture of the blades will be handled by one of *Omnidea's* partners, *UAVision*. They work with both glass and carbon fibre and have also started working with Kevlar. Glass fibre is the most commonly used material in the wind industry because it is cheaper [11], despite not having mechanical properties as good as the latter. Kevlar has suitable mechanical properties but different than those of carbon fibre

and it is used in different applications as well; it may be suited for components carbon fibre is not. In this case, higher mechanical properties are preferred but Kevlar is more expensive than carbon fibre, and its use cases fall outside of the requirements of this structure. In addition, *UAVision* has more experience working with carbon fibre, so it is preferable to choose it as the design material.

The blade will be manufactured as a hollow shell, a simple and common construction that efficiently resists flexural and torsional loads. However, it is not so efficient with out-of-plane shear loads, therefore one or more shear webs (Figure 5-3) , perpendicular to the blade chord, are included to address those loads [11]. These shear webs are usually manufactured with a structural foam core material which provide rigidity and stiffness with low weight.

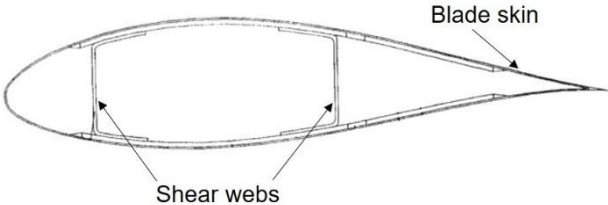


Figure 5-3 Example of an aerofoil cross-section with two shear webs. Adapted from [11]

The company providing the carbon fibre cannot divulge the exact properties of the material due to issues of confidentiality so information on standard carbon fibre fabric composite material from [35] was utilized. This is based on a composite made from carbon fibre fabric with epoxy resin (120°C cure), with 50% fibre volume. From the several properties calculated, the most relevant for the design process are detailed in Table 5-2.

Table 5-2 Properties of standard carbon fibre fabric composite material, $V_f = 50\%$. From [35]

Property	Unit	Symbol	Value
Young's modulus 0°/90°	GPa	E_L, E_T	70
In-plane shear modulus	GPa	G_{LT}	5
Major poisson's ratio	-	ν_{LT}	0.1
Ultimate tensile strength 0°/90°	MPa	S_L^+, S_T^+	600
Ultimate compressive strength 0°/90°	MPa	S_L^-, S_T^-	570
Ultimate in-plane shear strength	MPa	S_{LT}	90
Density	g/cm ³	ρ	1.6
Lamina thickness	mm	t	0.22

A widely used lay-up used on various applications is the quasi-isotropic laminate since, as the name indicates, it has a behaviour close to isotropic. This is considered to be a workable solution for the turbine blades though it should be noted that a study on the influence of different lay-ups ought to be performed. A typical quasi-isotropic lay-up is the symmetric $[0/\pm 45/90]_s$, which has a minimum of eight layers.

The shear webs for the blades will use a foam core of Airex C70.55 – Table 5-3 – with 3 mm thickness, reinforced with two plies of carbon fibre $[\pm 45]$ on each side to increase stiffness.

Table 5-3 Properties of Airex C70.55

Property	Unit	Symbol	Value
Young's modulus	MPa	E	45
Shear modulus	MPa	G	22
Ultimate tensile strength	MPa	σ_u	1.3
Shear strength	MPa	τ	0.85
Density	kg/m ³	ρ	60

5.2.3. Support arms

The support arms were first thought to be in aluminium, however, a quick design simulation and a few calculations showed that they would be unnecessarily heavy, as at least six are needed. Thus, composites are a preferable choice. Like the turbine blades, the support arms can be made of carbon fibre, which is much lighter and has better mechanical properties, and facilitates the manufacture of the arms since the mould for one arm can be re-used whereas an arm made out of aluminium has to be machined every time a new one is needed.

5.2.4. Inserts

Carbon fibre is an adequate material to manufacture both the blades and the support arms but separate parts are needed to attach them to each other and the support arms to the balloon. These components – inserts – will, most likely, have an uncommon and complex shape so carbon fibre and other composite materials are unsuited for their manufacture.

Metals are the most suitable material for the inserts, specifically aluminium alloys, which display favourable strength-to-weight ratios in the guise of the 6000 and 7000 series, which are used by *Omnidea* (6063-T6 and 7075-T6, respectively; their properties are listed in Table 5-4). They can be bonded to the composite parts using specific adhesives to bond metal to composites.

Table 5-4 Properties of the aluminium alloys

Property	Unit	Symbol	7075-T6	6063-T6
Young's modulus	GPa	E	71.7	68.9
Shear modulus	GPa	G	26.9	25.8
Ultimate tensile strength	MPa	σ_u	572	241
Tensile Yield strength	MPa	σ_y	503	214
Shear strength	MPa	τ	331	152
Density	g/cm^3	ρ	2.81	2.7

5.3. Support arms design

The support arms will attach the blades to the balloon. Independently of the arrangement, the arms will be positioned at 25% of the chord from the leading edge – the “quarter chord” – as it is typically done in most wind turbine designs, in order to reduce moments transferred from the blades to the supporting arms [13].

5.3.1. Arrangement

There are three main types of blade support arrangement (Figure 5-4) – simple support, cantilever support and overhang support. The first two types are favoured to minimize parasitic drag but have higher maximum moment and maximum deflection than the overhang support. The latter and the simple support are preferred for VAWT's with smaller capacity that, due to centripetal acceleration, have high bending moments [36]. Based on this fact, and since minimizing drag is an important aspect, the simple support is believed to be the best fit for the structure.

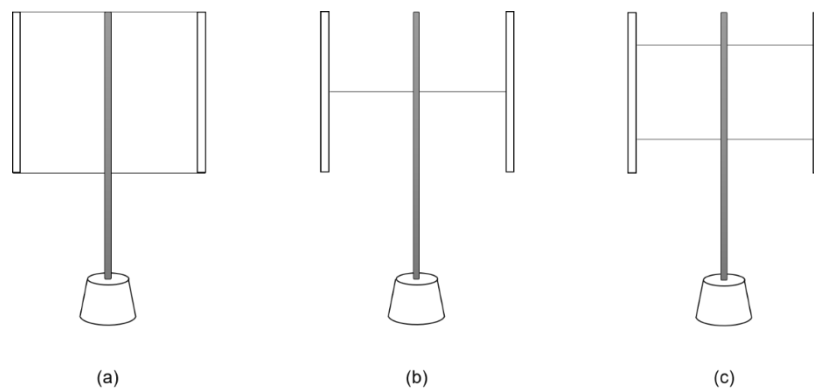


Figure 5-4 Blade support arrangements: (a) simple support; (b) cantilever support; (c) overhang support. Adapted from [36]

5.3.2. Cross-section

The cross-section of the arms has structural implications and can influence the power output of the turbine as some shapes can induce more drag than others. Usual shapes include rectangle, circle, elliptical and aerofoil. Eppler [37] designed and tested a few aerofoil profiles with low drag specifically for struts. Out of those, the E864 aerofoil, designed for a Reynolds number of 1,200,000, is better suited for this turbine since this is closer to the average Reynolds number of the turbine.

As an initial guess, the chord of the support arm aerofoil profile is set to 25% of the blade chord, $c_{arm} = 97.5 \text{ mm}$. For an E864 aerofoil – Figure 5-5 – thickness is 38.8 % of the chord so $t_{arm} = 37.82 \text{ mm}$. The profile skin thickness will correspond to the minimum possible thickness of the composite, as seen before for the blades, $e_{arm} = 8 \times t_i = 1.76 \text{ mm}$. During the simulations phase, the chord length will be iterated if necessary.

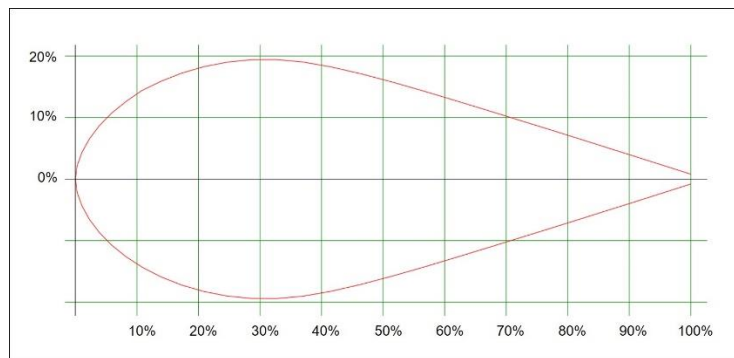


Figure 5-5 E864 aerofoil characteristics by percentage of chord

5.3.3. Configuration

For a given arrangement, the arms can also be configured in different ways. That is, in each support position one can have one or more arms with different configurations. In this project, the support arms are attached to the balloon which is not a rigid structure and, for example, a single arm configuration, like in Figure 5-6 (a), can lead the arms to suffer unexpected displacements which might force the balloon and rupture it. Therefore, a two-armed support seems like a better option. Arranging the arms in a triangle circumscribed about the balloon – Figure 5-6 (b) – prevents the rupture by eliminating the forces in the radial direction and placing them only on the outer net. Another advantage is the better stress distribution through the support arms.

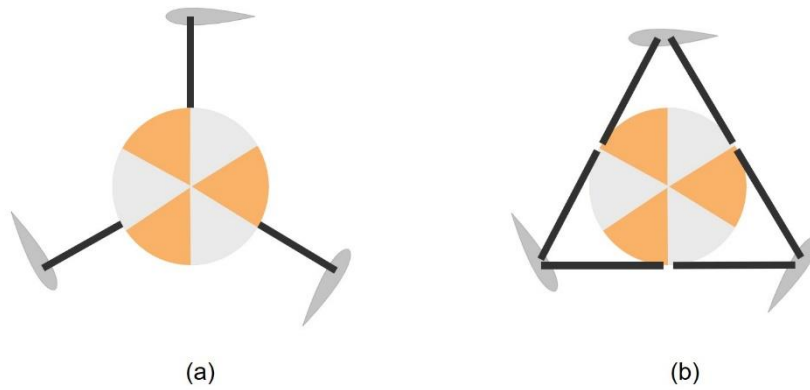


Figure 5-6 Schematics of different arm configurations: (a) single arm type; (b) triangle type.

5.4. Guy-wires

The blade structure was designed to be lightweight but still robust in order to endure the normal and tangential loads acting on the blades, due to the wind and the rotation of the structure. These forces were studied as so because, since the balloon can self-align with the wind, it will be “hitting” the structure on the direction of rotation. However, when the wind shifts direction, the balloon needs time to align. In those moments, the structure is subject to side winds and can oscillate.

For this reason, to increase the robustness of the structure, guy-wires will be added securing the sides of the blades to the rope that is casing the balloon.

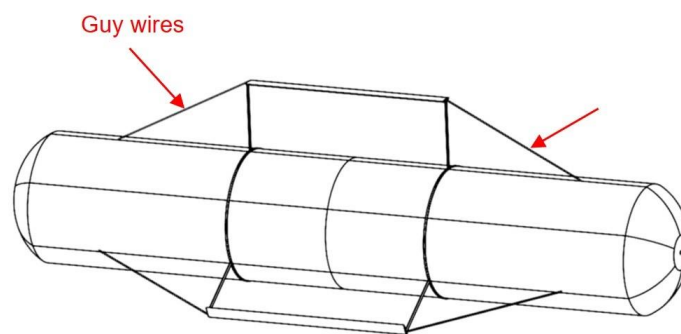


Figure 5-7 Schematic of the blade structure with guy-wires

5.5. Generator

As it is a common choice in new turbine designs for both its simplicity and economic competitiveness, the chosen generator is a permanent-magnet synchronous generator. The use of permanent magnets in the place of a coil system leads to less weight.

If the generator is directly connected to the turbine there is no need for a gearbox which means fewer mechanical losses. However, lower speed generators, used for direct-drive, are heavier than their higher

speed counterparts (they are usually in the hundreds of kilograms) and so they are not viable for this project. Therefore, a generator with higher rotational speed must be chosen and, consequently, a drivetrain must be designed.

From Alxion’s website [38] the 300STK3M model was considered a suitable option – Figure 5-8. Relevant characteristics can be found in Table 5-5 and Table 5-6. The dimensions are pictured Figure 5-9.



Figure 5-8 Permanent magnets frameless generators. From [38]

Table 5-5 Technical properties of the 300STK3M frameless generator

Property	Unit	Value
Rated speed	rpm	800
Rated Power	W	12150
Input torque at rated speed	N.m	160
Efficiency at rated power	%	90
Current at rated power	A	27.1
Voltage at rated power	V	261
Weight	kg	24.5

Table 5-6 Main dimensions of the 300STK3M frameless generator

Dimensions	Unit	Symbol	Value
Housing external diameter	mm	B	303
Rotoric internal diameter	mm	C	190
Housing length	mm	LB	142.5

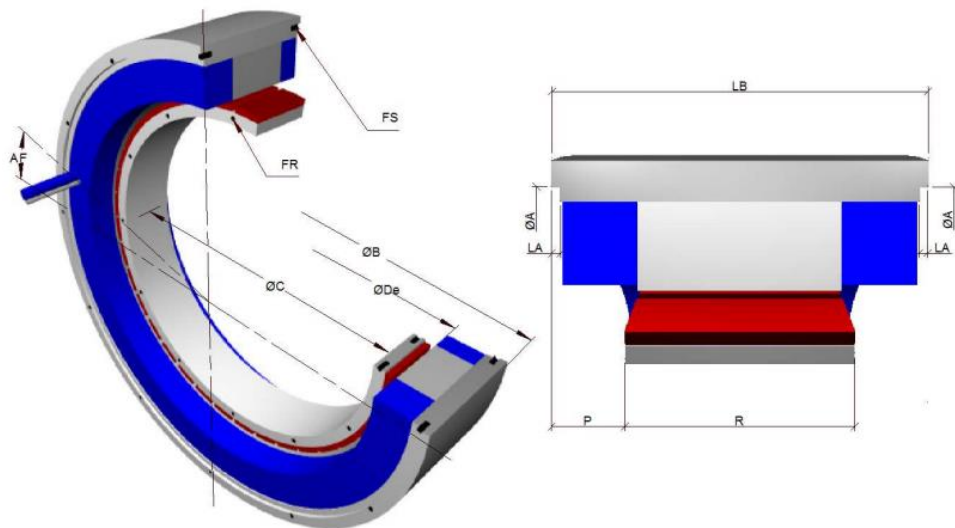


Figure 5-9 Representative scheme of the generator's dimensions. From [38]

5.6. Drivetrain

Knowing the nominal rotations of both the balloon and the generator the gear ratio can be computed ($i \approx 0.13$) and the design process of the drivetrain can start.

A few options emerged when conceiving the drivetrain. A retail planetary gearbox would be the easier option however, one good enough to withstand the applied torques would be too heavy. A simple pair of gears is a better option. Another possible solution would be a belt system, using the balloon itself as a pulley. It is predicted that this system would weigh approximately the same as the gear system, due to the size of the driven pulley, but it is estimated the first would be more complex and probably less robust and less safe when performing landings. Therefore, the drivetrain will be designed with a pair of gears. The material chosen for the gears was a steel alloy due to their high strength.

Following previous procedures from *Omnidea* a normalized module of $M = 3 \text{ mm/tooth}$ is chosen. Now, the width, b , and centre distance, a_{12} , of the gears are changed iteratively to compute diameter and tooth number in order to reduce the tooth pressure. The final dimensions are listed in Table 5-7 and the system is illustrated in Figure 5-10.

Table 5-7 Final dimensions of the gear pair

D_1	459	mm
D_2	60	mm
Z_1	153	teeth
Z_2	20	teeth
a_{12}	257	mm
b	25	mm

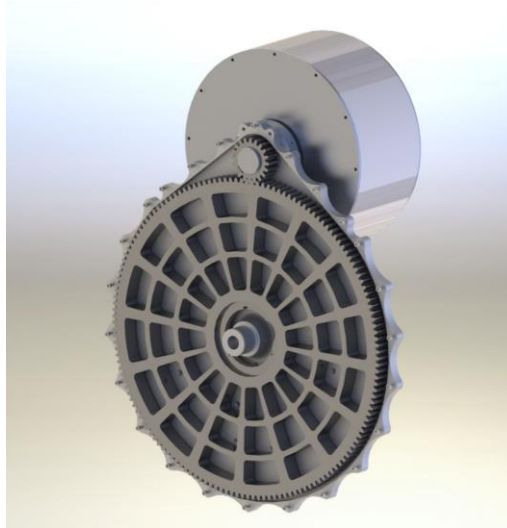


Figure 5-10 Gear transmission system

5.7. Balloon and turbine tether components

The main components designed by *Omnidea* to attach the balloon to the system of ground tethering remained the same. The rims and the boomerangs (for attachment of the cable) were not changed. The original module had two small motors on each end of the balloon and now, on the left side the balloon needs to act as a freewheel, in order to rotate, and on the right side – the side of the generator – it needs to transmit power to the drivetrain. This way, the disks and hubs for the bearing were adapted according to those needs – Figure 5-11 and Figure 5-12. The inserts for the support arms and the blades are designed to be constructed with three to four welded parts, and to be glued to the composites, as mentioned previously – Figure 5-13 and Figure 5-14 (a). The blade cover, also glued to the blades, will have a bolted connection to the blade support – Figure 5-14 (b). In Figure 5-13 it is possible to note a base plate with a bolted connection to the arms support. This plate will be placed underneath the *Dyneema* net, which is tightly surrounding the balloon, and will be attached to the arm support.

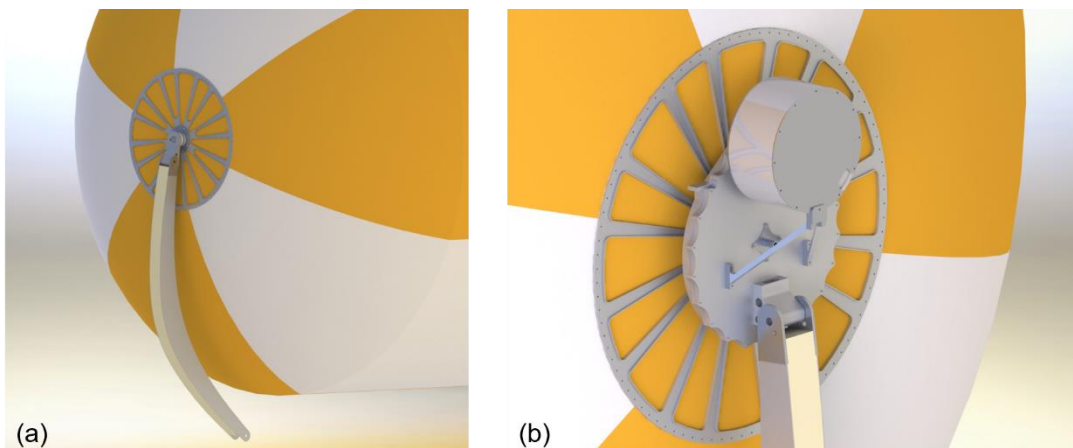


Figure 5-11 (a) Left end of the balloon, working as a “freewheel”; (b) right end of the balloon with the generator and drivetrain assemblies

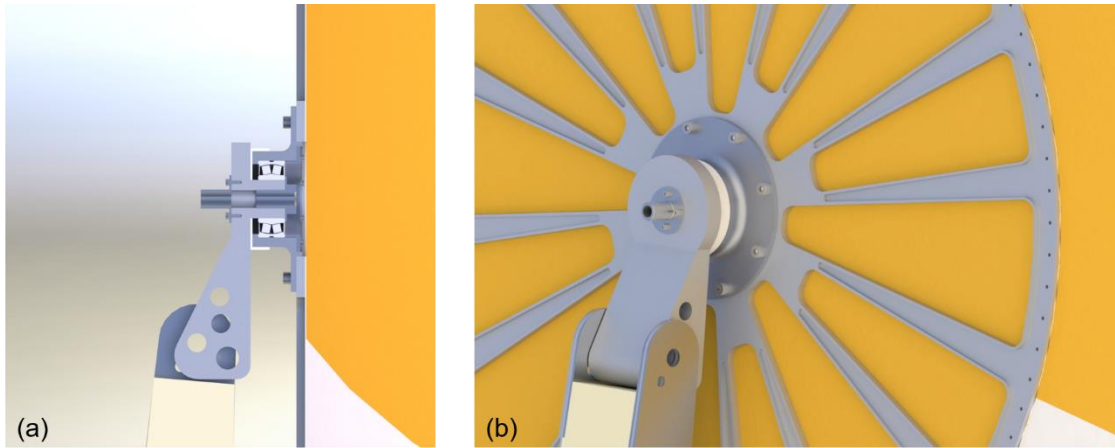


Figure 5-12 Section view (a) and a close-up view (b) of the left side assembly

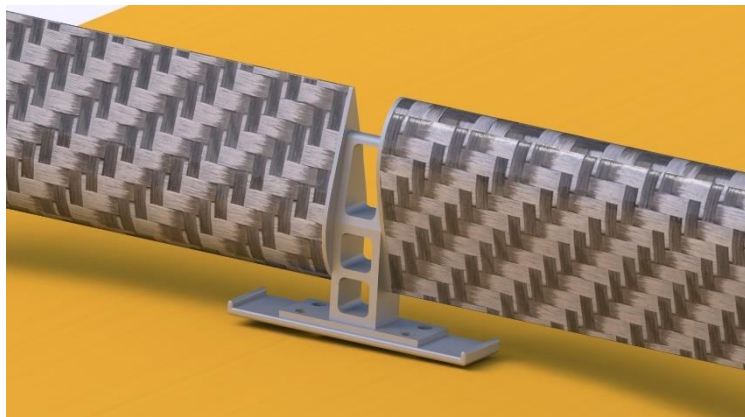


Figure 5-13 Arm support inserts

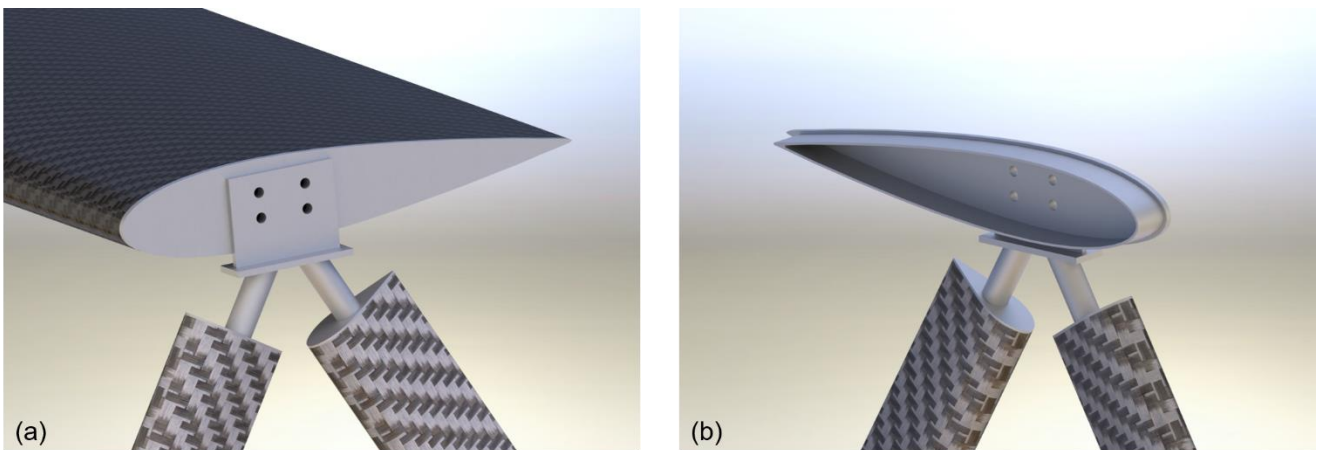


Figure 5-14 Blade support and blade cover inserts (a); interior view of the blade cover (b)

5.8. Buoyancy and weight distribution

With this project being an airborne system, it has been stated before that weight is a very important issue. Minimization of the weight is one of the primary goals of the structure's design. The weight of the structure will influence how high the system can float before it needs to rotate in order to fly higher. This is given by the buoyancy of the balloon since the balloon is filled with helium.

The buoyant force on a body is equal to the weight of the fluid displaced by the body. Archimedes' principle says,

$$F_{buoyant} = m_f g \quad (5.1)$$

where m_f is the mass of displaced fluid. This means, a body will float, at a certain height, when the buoyant force is equal to its weight [10]. For the purpose of checking the floatability of the system, only the mass of fluid displaced by the balloon will be accounted for since it is the main contributor to the buoyancy.

According to *Omnidea*, the balloon has a volume of approximately 205 m^3 . This is equivalent to 250.84 kg of air. Given that this is an airborne platform, it should be noted that the volume of helium should not change with height since it does not reach enough altitude for its density to change. Stating a minimum height of 20 m for the turbine to pick up wind and start to rotate, the structure will float at that height if its mass equals said mass of air. In Table 5-8 the weights of the components of the structure (by assembly) are listed, and the total weight can then be compared to the target mass of air.

Table 5-8 Listing of weight of the structure's parts

Parts	Weight [kg]
Helium volume	34.07
Balloon net and skin	70
Transmission assembly	19.45
Generator assembly	27.62
Blade and support arms inserts	4.85
Blades	42.66
Support arms	26.16
Other parts	21.75
Subtotal	246.56
Cable (20 m)	7.00
Total	253.56

The total weight of the structure is slightly higher than the buoyancy of the balloon which means the floatation ceiling lowers from 20 to 12 m . Ergo, the length of unwound cable is shorter. It is important to verify if this height is enough in terms of safety both for the workers and the apparatus.

5.8.1. Weight distribution

The existence of the generator and a transmission system – heavier components – on one side of the balloon leads to some uneven weight distribution of the structure. A counterweight, a common solution, is not a good option here since it will only add more weight to the module which is the opposite of the intended goal. The blade structure can be placed with an offset from the centre but since it cannot be completely positioned at the opposite end due to interference with the cable it cannot entirely make up for the weight disproportion – Figure 5-15.

The remaining imbalance can be compensated in a few other ways. If the balloon were lengthier it could not only sustain more weight, but it could also increase the offset and move the centre of mass of the entire structure towards the centre of the balloon.

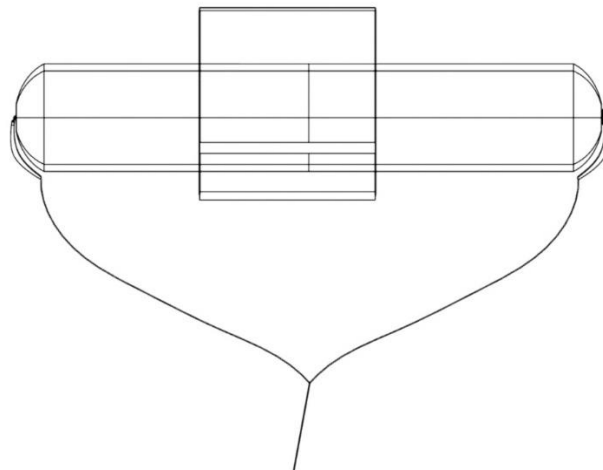


Figure 5-15 Schematic of the structure's off centre positioning with the cable

5.9. Load Calculation

As seen before, a wind turbine blade is subject to lift and drag forces which can be decomposed into normal and tangent forces (section 2.4) that contribute to the structural and torque loads acting on the blade. In addition to these forces, the blade, characterized by a certain weight and subject to a certain rotation, is also subject to gravitational and centrifugal forces which will add to said loads – Figure 5-16. All these forces are projected to the normal and tangent direction of the movement, which cause flapwise and edgewise bending, respectively as per Figure 5-17.

The structural and torque load calculations, as well as power and resulting torque, were performed using algorithms implemented in *Matlab* with inputs and outputs as in Figure 4-1.

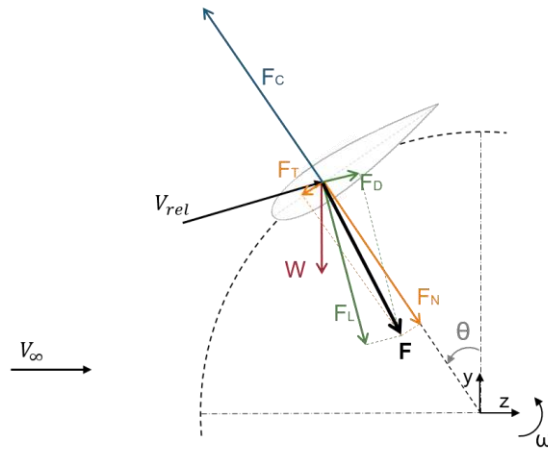


Figure 5-16 Total forces acting on a blade

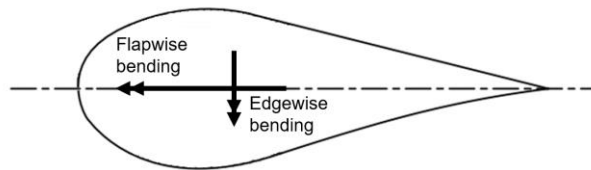


Figure 5-17 Depiction of flapwise and edgewise bending

5.9.1. Aerodynamic Loads

When addressing aerodynamic loads, it is known these are dependent on the environment conditions, which vary with time. As so, more than one load case should be considered when designing a turbine. This thesis will be looking at the two most important load cases:

- Normal operating conditions (V_{rated}), **Load case A**;
- Maximum operating conditions ($V_{cut-out}$), **Load case B**.

In the particular case of this turbine, if it reaches the maximum operating conditions it will be stopped and brought down for safe keeping, this way, load case B will lead the structural design of the turbine while load case A will only be monitored.

For either load case, the TSR is the first thing to calculate from equation (4.7) which is then used to compute the relative velocity, the local Reynolds number and the angle of attack, from equations (2.8), (2.12) and (2.16), respectively, for multiple positions through the course of a revolution. Then, with the use of an existing script from *MathWorks* file exchange [39], an interface is created between *Matlab* and *Xfoil*, a free online software [40] which calculates how the aerodynamic coefficients C_L and C_D vary with α for a given Re and aerofoil profile.

Now, using equations (2.18), (2.19), (2.20) and (2.21), one can compute the values of the forces F_L , F_D and then F_T and F_N , respectively, as a function of the position θ for one revolution. It is important to note that the wind acts on the entire length of the blade and therefore, if the forces are divided by the length L_b one gets uniformly distributed loads with intensities q_T and q_N .

5.9.2. Gravitational Loads

The weight of any object with mass m is given by

$$W = mg \quad (5.2)$$

Assuming a constant amount of material per unit length of the blade, it is possible to have a uniformly distributed load due to gravity with intensity

$$q_w = \rho_b A_s g \quad (5.3)$$

Where ρ_b is the density of the blade material, A_s is the blade's cross-sectional area and g is the gravitational acceleration equal to 9.8 m/s^2 .

The gravitational load has constant magnitude and vertical direction, directed at the ground (Figure 5-16). This means that in the reference frame of the rotor it will have a normal and a tangent component that will vary with the position θ

$$q_w^t = -q_w \sin \theta \quad (5.4)$$

$$q_w^n = -q_w \cos \theta \quad (5.5)$$

5.9.3. Centrifugal Loads

The centrifugal force is an inertial force, directed outward, in a rotating reference frame. For any object of mass m subject to a rotation ω this force is given by equation (4.10). Since this force is also dependent on the mass, the previous assumption for the gravitational force can be made again, and the uniformly distributed load comes as

$$q_c = \rho_b A_s R_{tur} \omega^2 \quad (5.6)$$

Like q_w , the centrifugal load has constant magnitude and direction, but this one is always directed outward from the rotor – Figure 5-16.

5.9.4. Support arms

The force analysis of the support arms is not as linear as the analysis of the blades, since the cross-section is not always in the same plane as the direction of the wind. Nevertheless, in structural design,

the components are designed for the situation of maximum loads, which allows for the study of a single instance in the case of these support arms.

Here, the situation of maximum load corresponds to the position with higher drag, which is portrayed in Figure 5-18, where one of the sides of the structure is aligned perpendicular to the direction of V_∞ . This way, the cross-section of the support arms sets 1 and 2 is aligned with the wind, with $\alpha = 0^\circ$. In set 1, the aerofoil is oriented with the direction of the wind ($\phi = 0^\circ$) and in set 2 in the opposite direction ($\phi = 180^\circ$) – Figure 5-19.

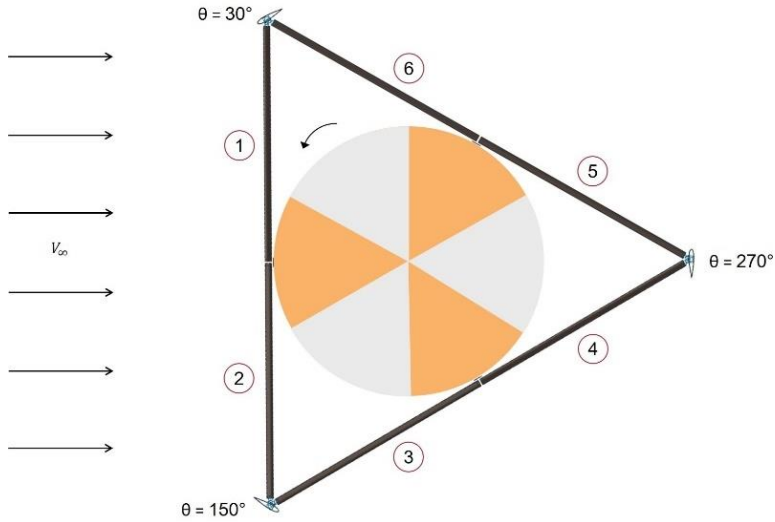


Figure 5-18 Position of support arms maximum load situation

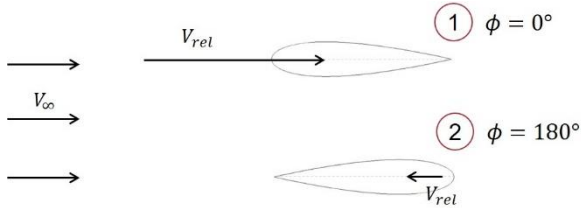


Figure 5-19 Alignment of support arms sets 1 and 2

The loads calculated here follow a conservative approach. The distributed load applied across the arms is considered uniform and does not account for the variation with radius. It is important to note that a more comprehensive study should be performed with the help of a computational fluids dynamic tool, to also assess the influence of each arm on the others.

The relative velocity used to calculate the drag force is calculated in relation to ϕ , the angle between the direction of the wind and the direction of the relative motion of the arm, V_{rel}^{arm} , represented in Figure 5-20. The tangential components of the relative velocity, V_{rel} , cancel each other out in every pair of support arms – pairs 1-2, 3-4 and 5-6. By employing vectorial calculations, the normal component is computed as

$$V_{rel}^n = V_{rel}^{arm} + V_{\infty}^n = \omega R + V_{\infty} \cos \phi \quad (5.7)$$

This is valid for every set of support arms, according to the position of the arm in relation to the wind velocity.

The drag is calculated as in equation (2.19), with V_{rel}^n . The drag coefficients are computed from *XFOil* for the strut profile E864, similar to the process used for the aerodynamic loads. Note that, by assessing the relative velocity in the normal direction, the angle of attack is always considered equal to 0°.

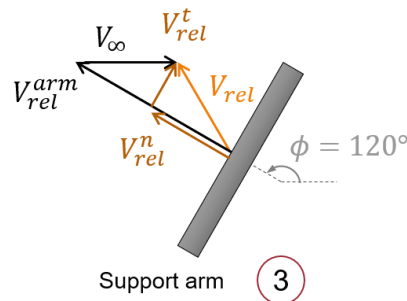


Figure 5-20 Schematic of the components of the relative velocity in relation to the support arms set 3

5.10. Safety Factors

In order to commence a designing process, it is important to define a safety factor which will command all further calculations. Safety factors can vary considerably depending on the purpose of the project, the safety issues involved, the knowledge of the materials, the working conditions, etc.

The method of the partial safety factors as stated in [41] is widely used for the design of wind turbines and contemplates the uncertainties and variability in loads and materials, the uncertainties in analysis' methods and the importance of structural components with regard to the consequences of failure. This way there are two types of safety factors to be defined – for loads and for materials.

5.10.1. Partial safety factors for loads

The partial safety factors for loads cover their variance, their probability of occurrence and the accuracy of the load model (gravitational, aerodynamic or inertial forces). These are independent of the materials.

The design values of the forces F_d come as

$$F_d = \gamma_F F_k \quad (5.8)$$

Where γ_F is the partial safety factor for the loads and F_k are their characteristic values.

In the analysis of ultimate strength, one can refer to Table 5-9, present in [41], which contains different safety factors according to the source of loading and the type of design situation. Since the calculations

will be made with respect to the total sum of applied forces, a conservative approach is taken and the same factor of 1.35 is applied to all loads.

Table 5-9 Partial safety factors for loads. From [41]

Source of loading	Unfavourable loads			Favourable loads
	Type of design situation			All design situations
	Normal and extreme	Abnormal	Transport and erection	
Aerodynamic	1.35	1.1	1.5	0.9
Operational	1.35	1.1	1.5	0.9
Gravity	1.1/1.35	1.1	1.25	0.9
Other Inertial forces	1.25	1.1	1.3	0.9
Heat influence	1.35	-	-	-

5.10.2. Partial safety factors for materials

The partial safety factors for materials consider the dependence on the type of material, the processing, geometrical parameters and, if fitting, the impact of the manufacturing process on the strength.

The design strength R_d is computed from the characteristic value of the materials' strength R_k and the partial safety factor for materials γ_M as per equation (5.9).

$$R_d = \frac{R_k}{\gamma_M} \tag{5.9}$$

For the static strength analysis, a value of 1.1 is to be used as a basis for metallic components. For the fatigue analysis, a different value should be considered and applied according to the criteria in Table 5-10.

Table 5-10 Partial safety factors for materials, for fatigue analysis. From [41]

Inspection and accessibility	Component failure results in destruction of wind turbine or endangers people	Component failure results in wind turbine failure or consequential damage	Component failure results in interruption of operation
Periodic monitoring and maintenance; good accessibility	1.15	1.0	1.0
Periodic monitoring and maintenance; poor accessibility	1.25	1.15	1.0

For fibre reinforced plastics, γ_M is derived from the multiplication of a basis factor with appropriate reduction factors that account for influences on the material properties. For a short-term strength verification, this leads to a partial safety factor for materials of 2.205 – Table 5-11. So, for the carbon fibre composite, in the longitudinal direction, the ultimate strength is $R_k = 600 \text{ MPa}$ and so, $R_d = 272.1 \text{ MPa}$.

Table 5-11 Reduction factors for the materials' partial safety factor. From [41]

Basis factor	γ_{M0}	1.35
Influence of ageing	C_{1a}	1.35
Temperature effect	C_{2a}	1.1
Laminate produced by resin infusion method	C_{3a}	1.1
Post-cured laminate	C_{4a}	1.0
$\gamma_M = \gamma_{M0} C_{1a} C_{2a} C_{3a} C_{4a}$		2.205

5.10.3. Analysis Procedure

The procedure with this method is to first, compute the stress S in the component resulting from the design loads – equation (5.10) – and then check if the stress remains lower than the design strength R_d of the material as per equation (5.11).

$$S = S(F_d) \tag{5.10}$$

$$S \leq R_d \tag{5.11}$$

6. Finite Element Analysis

6.1. Finite Element Method

The Finite Element Method or FEM is a numerical method where a given domain is represented as a collection of discrete parts (finite elements), and over each element the governing equation is approximated by some variational method. The elements are then assembled to obtain the solution to the initial domain. This assemblage is usually subject to boundary and/or initial conditions.

In this thesis, the program *SolidWorks*, employed in *Omnidea*, was used to model the turbine which was then imported to *Siemens NX*, used here to perform the pre-processing of the model, by simplifying, de-featuring and preparing the geometry for analysis in *NX Nastran*. It is also employed in the post-process and analysis of the results obtained. In the FEA program, a mesh is defined, for every part of the model, in order to better discretize the continuous domain.

6.2. Composite Failure Theory

There are many failure theories for composite materials whose main difference to isotropic materials is their directional dependence on strength on a macroscopic level. These criteria are employed on a ply-by-ply basis meaning the laminate is assumed to have failed when the first ply fails, the so called first-ply failure.

The most common and widely used theories are:

- Maximum stress theory;
- Maximum strain theory;
- Tsai-Hill failure criterion;
- Tsai-Wu failure criterion.

The first two assume no stress interaction and predict failure modes by comparing individual stresses or strains with their ultimate values, while the other two include interaction between different stress/strain components and are able to predict overall failure but do not predict the specific failure mode [42].

The maximum strain theory was chosen since it showed better results with the data available on material properties. Other theories were not certain to be accurate and this one was more conservative. In this theory, failure occurs when any principal material axis strain components exceed the corresponding ultimate strain. Thus, lamina failure does not occur if,

$$\begin{aligned} -\varepsilon_{Lc} < \varepsilon_{11} < \varepsilon_{Lt} \\ -\varepsilon_{Tc} < \varepsilon_{22} < \varepsilon_{Tt} \\ -\varepsilon_s < \varepsilon_{12} < \varepsilon_s \end{aligned} \tag{6.1}$$

Picking up Table 5-2, the design strengths are now calculated and listed in Table 6-1.

Table 6-1 Properties of standard carbon fibre fabric composite material, $V_f = 50\%$

Property	Unit	Symbol	Value
Young's modulus 0°/90°	GPa	E_L, E_T	70
In-plane shear modulus	GPa	G_{LT}	5
Ultimate tensile design strength 0°/90°	MPa	$\sigma_{Lt}^d, \sigma_{Tt}^d$	272.1
Ultimate compressive design strength 0°/90°	MPa	$\sigma_{Lc}^d, \sigma_{Tc}^d$	258.5
Ultimate in-plane shear design strength	MPa	σ_{LT}^d	40.8

With these properties it is possible to calculate the values for the ultimate design strains, in order to apply the method of the partial safety factors,

$$\varepsilon_{Lc}^d = \frac{\sigma_{Lc}^d}{E_L} = 0.00369 \quad \varepsilon_{Lt}^d = \frac{\sigma_{Lt}^d}{E_L} = 0.00388$$

$$\varepsilon_{Tc}^d = \frac{\sigma_{Tc}^d}{E_T} = 0.00369 \quad \varepsilon_{Tt}^d = \frac{\sigma_{Tt}^d}{E_T} = 0.00388$$

$$\varepsilon_s^d = \frac{\sigma_{LT}^d}{G_{LT}} = 0.00816$$

FEM simulations are particularly helpful to determine the behaviour of composite materials and employ these theories. *NX Nastran* has a module dedicated to laminated composites which uses ply failure theories to compute ply failure indices, margins of safety and/or strength ratios.

The ply failure index can be applied to any failure criteria and indicates the regions where the laminate could fail. If $PFI \geq 1$, the lamina is unsafe and may fail. The strength ratio specifies the safety of the composite and determines how much the applied load can be increased or should be decreased by whether it is safe or unsafe.

6.3. Simulations

6.3.1. Convergence study

First, a convergence study must be performed to choose the appropriate element size for the next simulations. For this, one single element is chosen to monitor the values of ply strain and ply failure index. The element from which the results will be retrieved was chosen from an area that corresponded to a high gradient of displacements, at approximately 0.75 m from the left of the blade – Figure 6-1. Starting at an element size of 50 mm, the mesh was refined several times by reducing the element size in half.

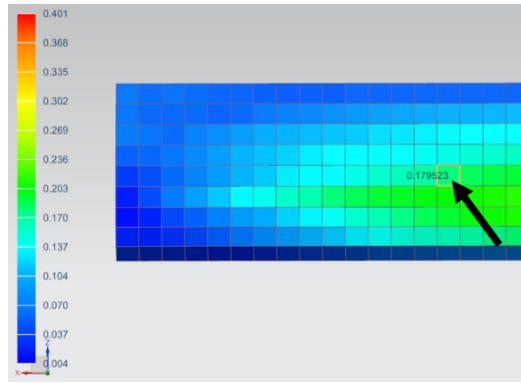


Figure 6-1 Representation of the chosen element

Table 6-2 lists the values of ply failure index and ply strain found for the selected element, always for the same ply (ply 1). Figure 6-2 represents the convergence plots of those values. In every case, the values converge as the mesh is refined. The refinement was stopped when the difference in ply strain and PFI values between element sizes was small enough (around 4%) to consider the mesh appropriate for further simulations.

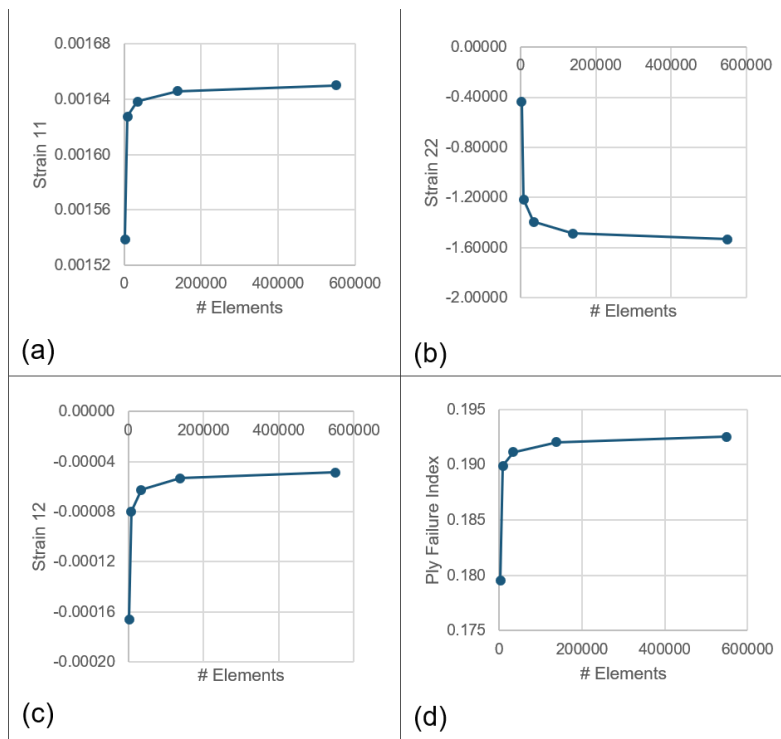


Figure 6-2 Relation between ply stress and number of elements – (a) ϵ_{11} (b) ϵ_{22} (c) ϵ_{12} – and between ply failure index and number of elements (d)

Table 6-2 Values of ply failure index and ply strain for the different mesh sizes

Element Size [mm]	# Elements	PFI	ϵ_{11}	ϵ_{22}	ϵ_{12}
50	2492	0.180	0.00154	-0.43862	-0.00017
25	8639	0.190	0.00163	-1.21652	-0.00008
12.5	34492	0.191	0.00164	-1.39470	-0.00006
6.25	138556	0.192	0.00165	-1.48805	-0.00005
3.125	550146	0.193	0.00165	-1.53594	-0.00005

6.3.2. Single Blade

Having completed the convergence study, a single blade was analysed so as to assess the performance of the component and the need for extra supports along its length. As this is a simpler, preliminary analysis, the focus was on the situation of maximum load (Table 6-3) in both the radial and the tangential direction – even though they might not occur at the same time. The loads applied in the simulation correspond to the design loads referred to in section 5.10 of the partial safety factors.

Note that, while the structure is designed according to the maximum load case B, load case A was also considered in the analysis so as to verify the stresses in the most frequent case, which will be the main source of fatigue in the structure.

Table 6-3 Radial and tangential maximum forces and their correspondent position

	Load Case A		Load Case B	
	Force [N]	θ [°]	Force [N]	θ [°]
Radial direction	13977.9	300	22909.4	330
Tangential direction	1111.6	300	2386.5	90

Composite structures usually have two dimensions much larger than the third, particularly, length and width larger than thickness and, as such, 2D shell elements are commonly used to model these types of problems. Here, the blade was subjected to linear static analyses and meshed using linear quadrilateral elements with an element size of 3.125 mm. The thickness of the profile is defined in the element properties and corresponds to the actual thickness of the skin. The same is valid for the shear webs.

One important aspect to address when modelling composite laminates is the element material orientation. One must guarantee that all the elements in the mesh of the component are pointing in the

same direction, usually in the longitudinal axis so as to agree with the 0° orientation of the plies. In Figure 6-3 there is an example of the element material orientation of a blade.

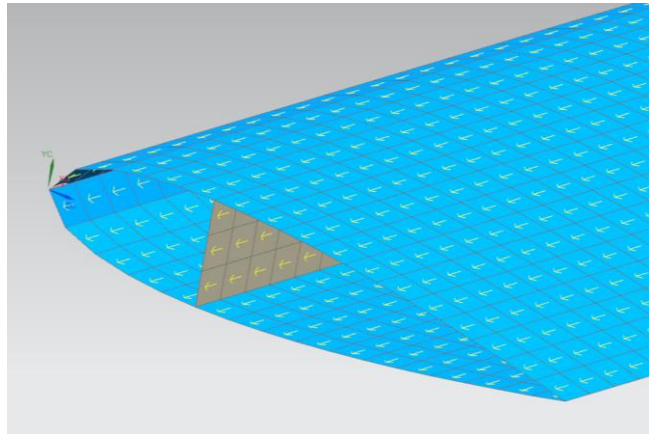


Figure 6-3 Element material orientation of blade meshes where the yellow arrows represent the 0° orientation

With the mesh fully prepared, two boundary conditions were applied: a simple support constraint on one side and a fixed constraint with free rotation in the x axis (length of the blade) on the other – Figure 6-4, in order to simulate, as closely as possible, the boundary conditions of the blade in the structure.

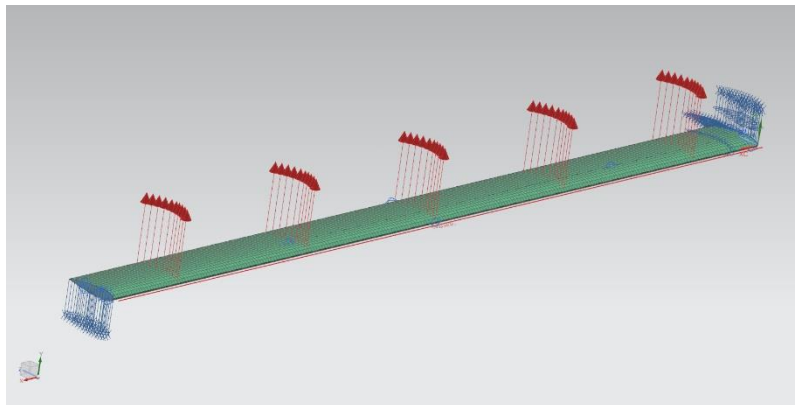


Figure 6-4 Meshed blade with applied loads and constraints

After completing the analysis, it was found that the efforts on the blade surpassed the design strength by, approximately, 190%. This is not acceptable and was expected due to length of the blade and the high loads applied. For this reason, a few design options were simulated in order to find the best configuration for the blades.

After the first analysis, six iterations were performed. Iterations 2 and 3, with different shear web configurations – Figure 6-5. In iteration 4, the lay-up was doubled, to increase skin thickness. Iteration 5 featured a higher thickness profile, the NACA0021. In iteration 6, the solidity was increased to 0.4 and, accordingly, the chord to 0.510 m. Finally, iteration 7 simulated two blades with 3 metres in length each,

with a support in the middle. The results for maximum value of displacement, ply failure index and ply stress, the latter for both load cases, are listed in Table 6-4.

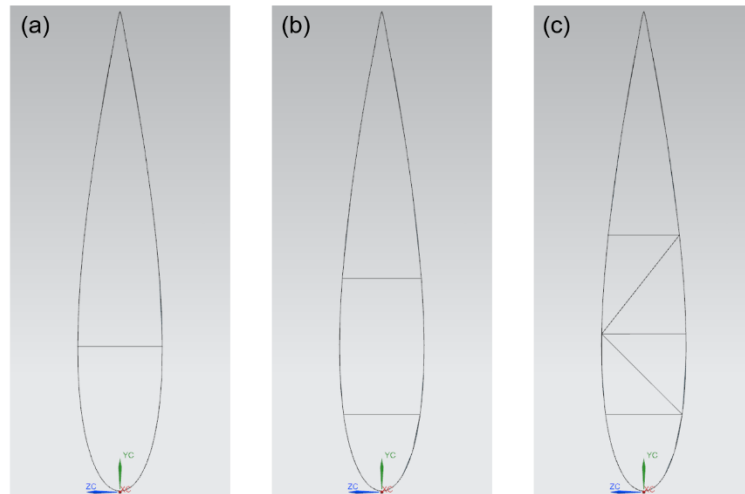


Figure 6-5 Different shear web configurations: (a) one shear web, iterations 1 and 4 through 7; (b) two shear webs, iteration 2; (c) shear web structure, iteration 3

Table 6-4 Results of the iterations simulations

# Iteration	1	2	3	4	5	6	7
Blade weight [kg]	14.20	14.75	17.19	27.75	14.57	18.73	14.20
Max displacement B [mm]	583	616	594	314	437	282	49
Max PFI B	1.601	1.738	1.701	0.916	1.417	1.116	0.451
Max ply strain 11 B	0.0113	0.0129	0.0120	0.0069	0.0112	0.0039	0.0031
Max ply strain 11 A	0.0079	0.0082	0.0073	0.0042	0.0069	0.0023	0.0019

As it is possible to see from the previous table, only configuration 7 proves to be adequate for the load cases considered. As such, the turbine structure will be redesigned in order to accommodate a third set of support arms. This will increase the total weight of the structure from 246.56 to 263.55 kg which is higher than the buoyancy of the balloon. This can no longer be solved by lowering the floatation ceiling. To address this issue, two solutions could be devised: creating a new module with higher length; or adding a smaller balloon to the existing one that could provide extra buoyancy.

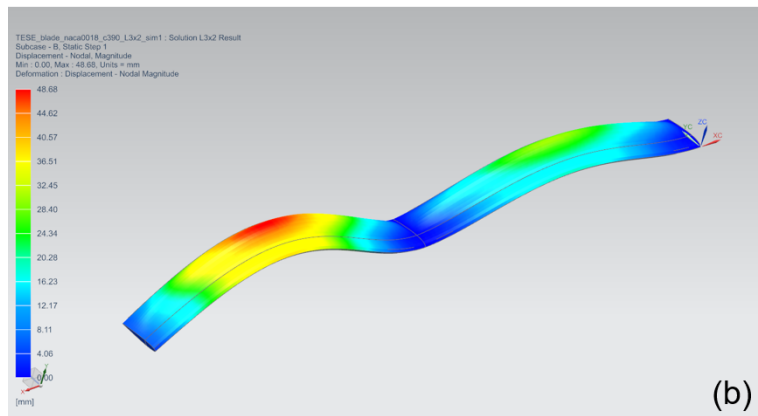
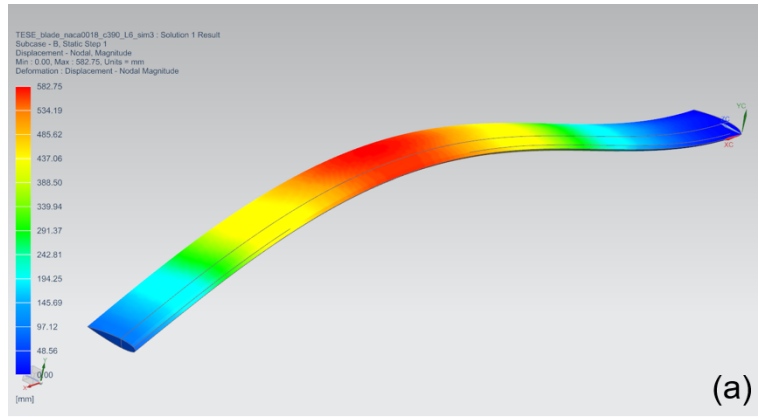


Figure 6-6 Displacement for load case B, for iterations 1 (a) and 7 (b)

6.3.3. Support arms

After analysing the blade's behaviour and verifying its design, the next study can now focus on the support arms. Based on the load calculations from subsection 5.9.4, for a chord of $c = 0.975 \text{ m}$, the acting loads for each set of support arms were calculated in *Matlab* and are listed below.

Table 6-5 Loads acting on each set of support arms

# set	F_{arm}^d [N]
1	11135
2	4675
3	6753
4	10519
5	6753
6	10519

The blades were first meshed the same way as before, with a 2D mapped mesh with linear quadrilateral elements with an element size of 3.125 mm and so were the support arms. However, this proved to be too refined a mesh to solve in the available computer and so, taking into consideration the complexity of smaller elements and the convergence analysis, the size of the elements was increased to 10 mm.

The geometry was defeatured in order to facilitate meshing, cut down the simulation time and provide for accurate enough results given the overall complexity and size of the structure: small features such as fillets and chamfers were removed to facilitate meshing with 3D tetrahedra or hexahedra (depending on the shape of the part) (Figure 6-7); thin geometries such as the blades and arms were converted into midsurfaces to allow for meshing with 2D shell elements and some connection elements were reduced to a line representing their central axis to allow for meshing with 1D beam elements (Figure 6-8). All meshes were connected using connection elements (RBE3) regardless of whether the parts were glued, welded or screwed to each other.

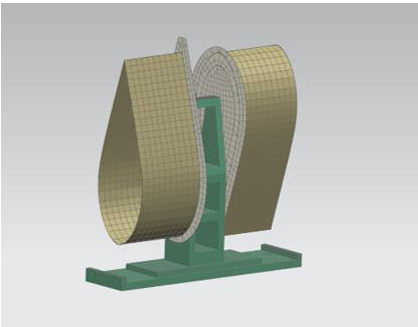


Figure 6-7 3D and 2D meshes of an arm support

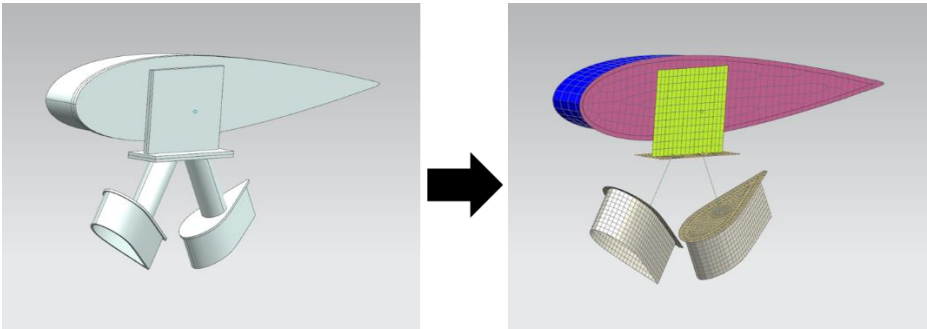


Figure 6-8 Simplification of blade support and blade cover parts

The guy-wires were modelled as 1D rod elements and connected to the blades using RBE3 connectors. The material was characterized with a non-linear behaviour, since it is a rope, with the stress-strain information from Figure 5-2.

The arm supports that connect to the balloon's net were fixed, along with the end of the guy-wires, so as to simulate the boundary conditions present therein.

With the new model prepared, the analysis is run again. The initial value of support arm chord proves to be inadequate to the situation evaluated and so the chord value is iterated until an acceptable value is reached. This happens when all three conditions of the maximum strain theory are met. In this study, only two iterations were needed, and the chord length achieved was $c = 110 \text{ mm}$. The results are listed in Table 6-6. Again, it is important to note that this a conservative approach since the influence of each arm on the others during rotation is not accounted for.

Table 6-6 Results for the different support arms' chord simulations

Chord [mm]	Max ϵ_{11}	Max ϵ_{22}	Max ϵ_{12}	Min ϵ_{11}	Min ϵ_2	Min ϵ_{12}	Max displacement [mm]
97.5	0.00446	0.00237	0.00434	- 0.00471	- 0.00191	- 0.00406	125.6
100	0.00397	0.00151	0.00359	- 0.00377	- 0.00135	- 0.00323	102.4
110	0.00386	0.00149	0.00257	- 0.00363	- 0.00129	- 0.00262	93.9

6.3.4. Full Structure

After analysing the blade's behaviour and verifying the support arms design, the full turbine structure can be simulated. This analysis was performed with the loads in the radial and tangential direction, only this time multiple subcases were created where each represents a different load situation for each increment of θ . The load values applied are detailed in Table 6-7. The full structure was subjected to a series of linear static analyses, analogue to those performed on the blade only (as described in section 6.3.2).

The results for the node and element, illustrated in Figure 6-9 to Figure 6-11, proved to stay within the limits of the conditions of the maximum strain theory. The maximum values computed portray specific areas of the blades where the values extend outside of the defined acceptable limits (Figure 6-13); these are areas of stress concentrations. This happens at the blades' extremities where the shear webs and blade covers meet. This issue is caused by the simplification of the model and it can be resolved by applying a reinforcement to the shear web, making it into an I-profile. The inserts also display the same issue of stress concentrations due to the simplification of the model. This problem should not occur in the real components since they have features like fillets or chamfers or have welds.

Appendix B presents images of the displacement and the ply strain of the full structure, for the position $\theta = 330^\circ$.

Table 6-7 Radial and tangential design forces for each position θ

θ [°]	Load Case A		Load Case B	
	F_N^d [N]	F_T^d [N]	F_N^d [N]	F_T^d [N]
0	10346.6	-38.1	15745.6	-65.6
30	7120.1	-32.7	7051.7	500.1
60	5035.3	367.6	2332.1	2376.4
90	4384.1	677.2	4281.9	2386.5
120	5364.5	488.0	7305.0	1360.6
150	7254.7	54.0	9071.2	683.7
180	9217.7	-16.2	12556.7	-14.5
210	10983.1	436.9	14479.3	614.3
240	11878.4	821.2	13994.7	107.2
270	12912.7	1072.0	18151.2	1512.1
300	13977.9	1111.6	21270.2	2158.7
330	134689.0	555.0	22909.4	1626.3

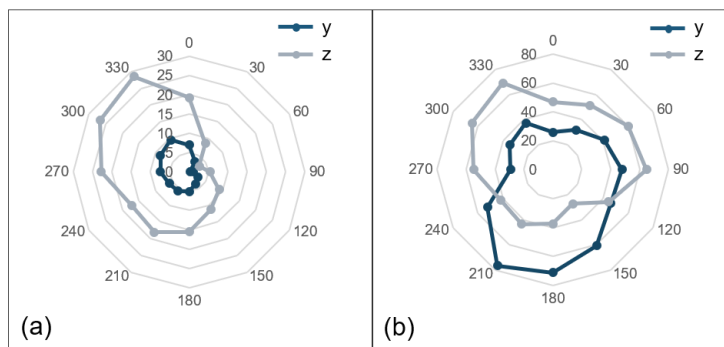


Figure 6-9 Variation of displacement in node 6504233 (a) and maximum absolute displacement of the whole structure (b) in the y and z directions, in mm, with position θ

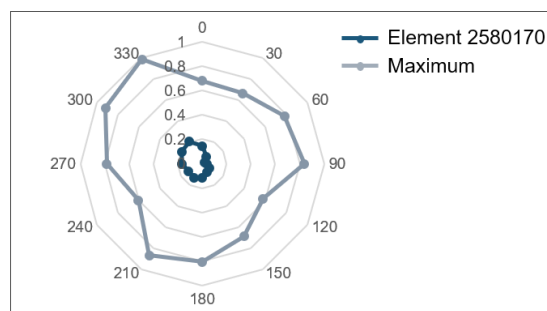


Figure 6-10 Variation of Ply Failure Index in element 5803420 with position θ

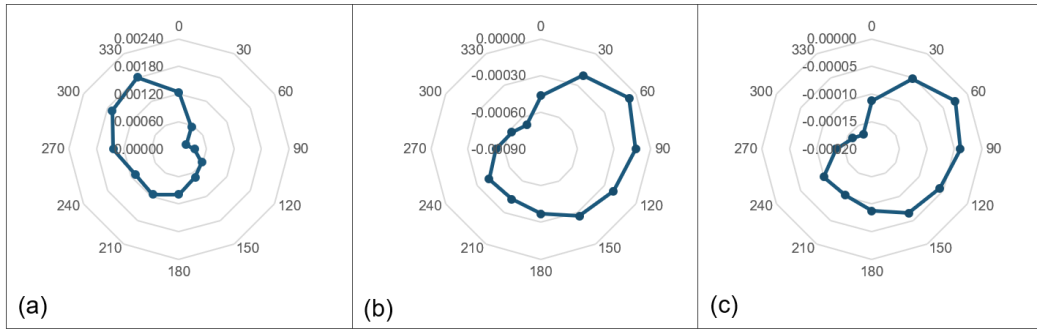


Figure 6-11 Variation of ply 1 strain in element 5803420 in the principal directions 11 (a), 22 (b) and 12 (c)

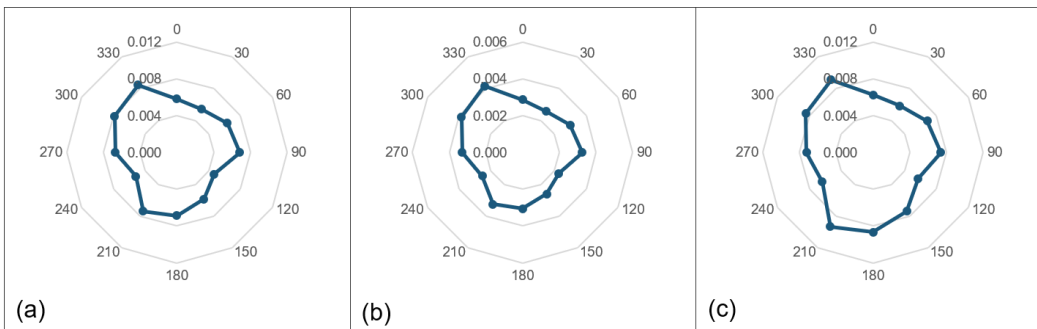


Figure 6-12 Variation of ply 1 maximum strain in element 5803420 in the principal directions 11 (a), 22 (b) and 12 (c)

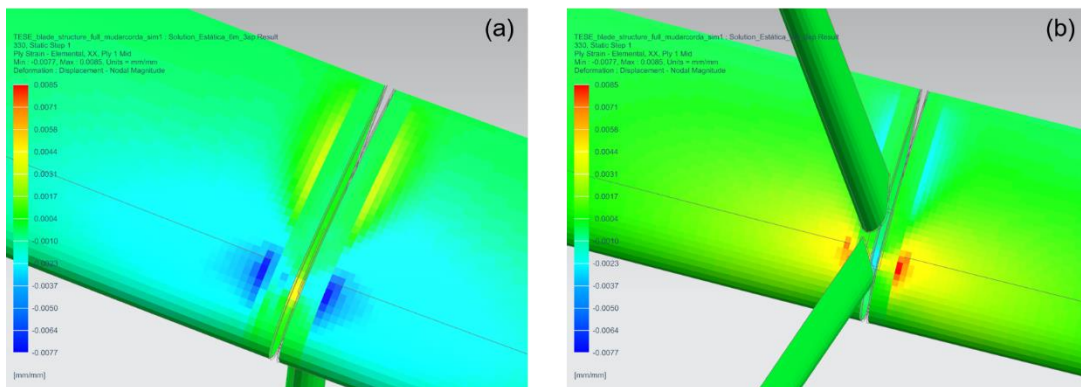


Figure 6-13 Representation of maximum ϵ_{11} of the structure: (a) in compression and (b) in tension for position $\theta = 330^\circ$

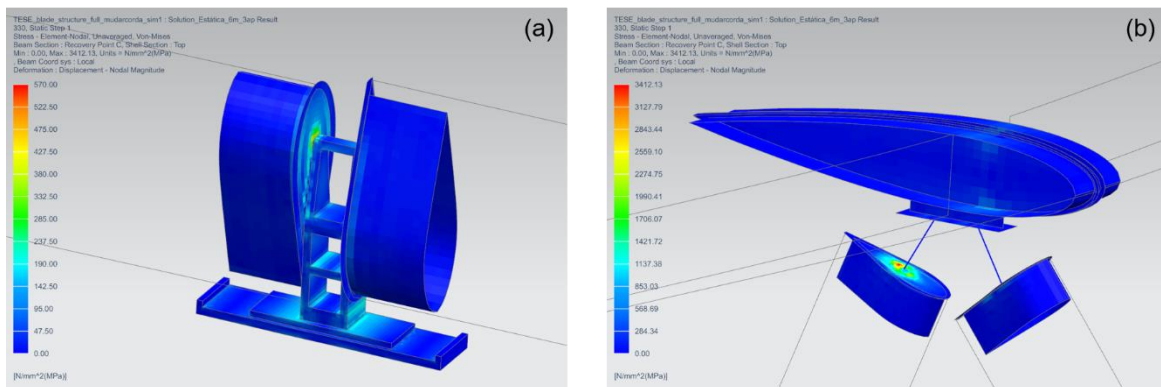


Figure 6-14 Representation of the Von Mises stress on the arm support (a) and blade support (b) for position $\theta = 330^\circ$

6.3.5. Dynamic analysis

A dynamic analysis is another important verification to perform. This kind of analysis is used to determine the natural frequencies and mode shapes of a structure, characterizing the behaviour of the structure when subject to dynamic loading. This is especially vital when working with rotating machines. It is vital that the operating frequency of said machine does not coincide with the natural frequencies of the components, or it could lead to structural damage or failure.

The turbine developed in this thesis was determined to rotate at a maximum of, approximately, $130 \text{ rpm} \approx 2.2 \text{ Hz}$. For structural safety, the first natural frequency of the structure should be at least double that.

The natural frequencies and respective normal modes were obtained using *NX Nastran*. Only a few modes are presented in Figure 6-15 due to similarities in shape between them (consequence of symmetries in the structure). The modes are represented on a 10% model amplification in order to be properly visible (otherwise they would be too small to be noticeable); thus, the presented magnitude of the displacements does not represent the real displacements. The first ten natural frequencies of the structure are listed in Table 6-8. It is possible to see that the first five modes, for example, could happen simultaneously since their frequencies are very close to each other. Still, this proves not to be an issue since these frequencies are around six times higher than the frequency of rotation of the structure.

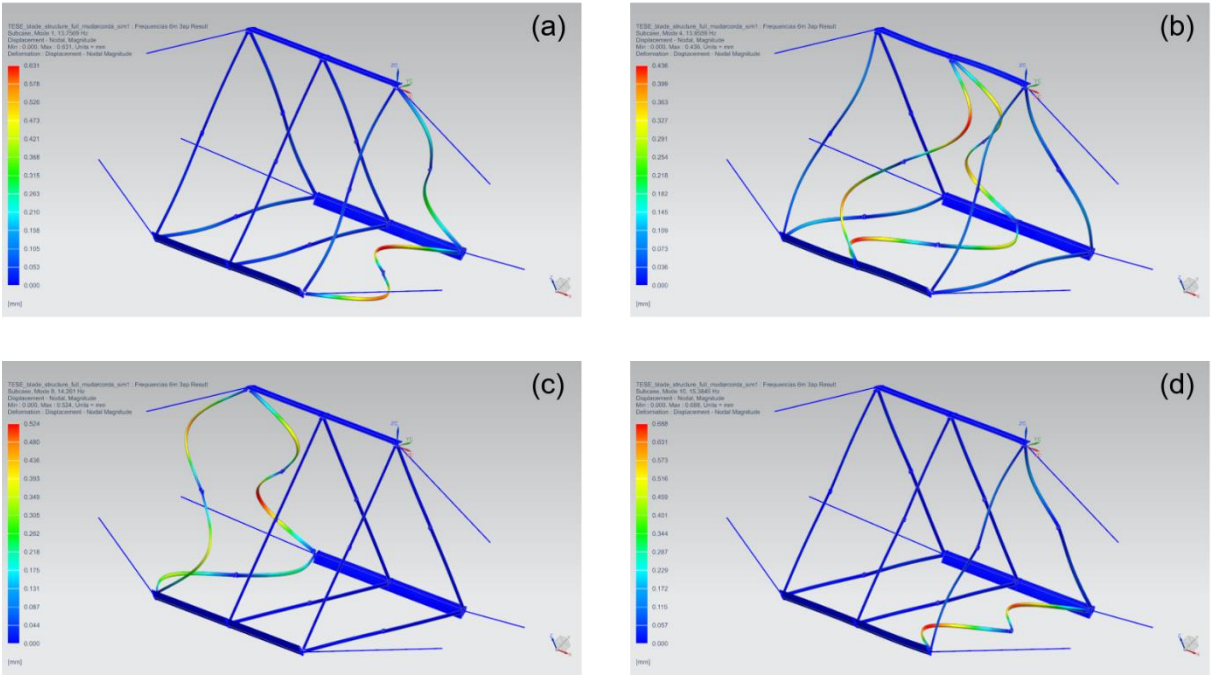


Figure 6-15 Mode shapes of the structure: (a) mode 1; (b) mode 4; (c) mode 9; (d) mode 10

Table 6-8 Natural frequencies of the first ten normal modes of the structure

# Mode	Frequency [Hz]
1	13.757
2	13.845
3	13.919
4	13.956
5	13.998
6	14.016
7	14.072
8	14.131
9	14.261
10	15.384

7. Conclusions and/or Future work

7.1. Conclusions

The work introduced in this thesis was born from *Omnidea's* ambition and motivation to further develop their existing airborne wind system with new and different functionalities. The main goal was to develop a wind turbine that could be attached to the Magnus balloon system, in order for it to work at high altitudes where higher wind speeds are available and occur more often.

A concept development process was employed so as to first achieve the best concept idea for design based on existing studies and information on vertical axis wind turbines. The options were weighed, compared and selected with the purpose of ensuring maximum efficiency. The mechanical components were designed to ensure structural integrity and to be as lightweight as possible. This was the main difficulty in the project since the balloon only has so much buoyancy. These components were reiterated a couple times in order to reduce weight to the maximum. The balloon, besides providing the system with floatability, also had a role in providing lift. The Magnus effect will most likely be disturbed by the presence of the turbine, which is probably the main source of lift during rotation, but only a computational fluid dynamics study could provide more insight into that issue. This kind of study could also provide more accurate information on the amount of power the designed structure could produce which could affect the design of the blades and even the support arms of the turbine.

After the first structural finite element analyses, the rotor suffered some design changes which greatly affected the total weight of the structure. It increased from 246.56 to 263.55 kg, which is higher than the buoyancy provided by the balloon. This could be addressed by creating a new module with higher length or adding a smaller balloon to the existing one that could provide extra buoyancy.

Concluding, this 12 kW wind energy system can be a good start for further developments in the area. Conducting computer fluid dynamics studies can help improve the design in order to make it more lightweight. A more comprehensive study on the materials used in every component can also help with that issue. Nonetheless, this project is not necessarily fixed as a wind energy system. It could also be used as a self-sustained platform for terrain observation and mapping, fire monitorization or even for telecommunications. Different purposes might need different requirements in terms of generated power which can change the design.

7.2. Future work

The work developed in this thesis focused only on the structural design and assessment of this new kind of wind turbine. Computer fluid dynamics studies fall out of the scope of this thesis although, as already stated, some studies should be performed in conjugation with the mechanical design to better understand the aerodynamic and power losses that are happening, the lift that the blades and the

balloon are creating and, mainly, the amount of power the turbine is producing. This will help improve the design.

A more detailed composites study could also be beneficial. It could improve lay-up design which affects the weight and stiffness of the structure.

The drivetrain system must be subjected to more detailed studies since the one presented should only be considered introductory as it could possibly be lighter by using different materials or switching to pulleys. Any of these systems should take into account the lubrication system used.

Developing a prototype on a smaller scale for testing in a wind tunnel could also help to better understand the aerodynamic and structural behaviour of the structure.

8. References

- [1] P. M. Oliveira, "Sustentação Aerodinâmica," 2008.
- [2] R. Schmehl, *Airborne Wind Energy 2011*. 2011.
- [3] L. Perkovic, P. Silva, M. Ban, N. Kranjcevic, and N. Duic, "Harvesting high altitude wind energy for power production: The concept based on Magnus' effect," *Appl. Energy*, vol. 101, pp. 151–160, 2013.
- [4] A. D. Sahin, "Progress and recent trends in wind energy," *Prog. Energy Combust. Sci.*, vol. 30, no. 5, pp. 501–543, 2004.
- [5] M. M. Aslam Bhutta, N. Hayat, A. U. Farooq, Z. Ali, S. R. Jamil, and Z. Hussain, "Vertical axis wind turbine - A review of various configurations and design techniques," *Renew. Sustain. Energy Rev.*, vol. 16, no. 4, pp. 1926–1939, 2012.
- [6] H. Ritchie and M. Roser, "Energy Production & Changing Energy Sources," *OurWorldInData.org*, 2018. [Online]. Available: <https://ourworldindata.org/energy-production-and-changing-energy-sources/>. [Accessed: 10-Jan-2018].
- [7] Wind Energy Development Programmatic Environmental Impact Statement, "Wind Energy Basics." [Online]. Available: <http://windeis.anl.gov/guide/basics/index.cfm>. [Accessed: 11-May-2017].
- [8] G. M. Joselin Herbert, S. Iniyar, E. Sreevalsan, and S. Rajapandian, "A review of wind energy technologies," *Renew. Sustain. Energy Rev.*, vol. 11, no. 6, pp. 1117–1145, 2007.
- [9] L. Gato, *Wind energy*. 2016.
- [10] F. White, "Fluid Mechanics," *McGraw-Hill, New York*, 2010.
- [11] T. Burton, D. Sharpe, N. Jenkins, and E. Bossanyi, *Wind Energy Handbook*, 1st ed., vol. 53, no. 9. 2013.
- [12] J. B. Bevirt, "High-altitude wind: Fast and consistent." [Online]. Available: <http://www.jobyenergy.com/haw/resource>. [Accessed: 15-May-2017].
- [13] M. Wahl, "Designing an H-rotor type Wind Turbine for Operation on Amundsen-Scott South Pole Station," *Uppsala Univ.*, no. December, p. 73, 2007.
- [14] J. F. Manwell, J. G. McGowan, and A. L. Rogers, *Wind Energy Explained: Theory, Design and Application*, 2nd ed. John Wiley & Sons, 2003.
- [15] B. K. Kirke, "Evaluation of Self-starting Vertical Axis Wind Turbines for Stand-alone Applications," 1998.
- [16] S. J. Johnson and D. E. Berg, "Active Load Control Techniques for Wind Turbines," *Contract*, no. August, pp. 1–132, 2008.

- [17] A. Hemami, *Wind Turbine Technology*, 1st ed. Cengage Learning, 2012.
- [18] A. P. Schaffarczyk, *Introduction to Wind Turbine Aerodynamics - Chapter 2*, vol. 153. 2014.
- [19] X. Jin, G. Zhao, K. Gao, and W. Ju, "Darrieus vertical axis wind turbine: Basic research methods," *Renew. Sustain. Energy Rev.*, vol. 42, pp. 212–225, 2015.
- [20] M. Ahmadi-Baloutaki, R. Carriveau, and D. S.-K. Ting, "Straight-bladed vertical axis wind turbine rotor design guide based on aerodynamic performance and loading analysis," *Proc. Inst. Mech. Eng. Part A J. Power Energy*, vol. 228, no. 7, pp. 742–759, 2014.
- [21] M. Rossander *et al.*, "Evaluation of a blade force measurement system for a vertical axis wind turbine using load cells," *Energies*, vol. 8, no. 6, pp. 5973–5996, 2015.
- [22] S. Brusca, R. Lanzafame, and M. Messina, "Design of a vertical-axis wind turbine: how the aspect ratio affects the turbine's performance," *Int. J. Energy Environ. Eng.*, vol. 5, no. 4, pp. 333–340, 2014.
- [23] E. Dyachuk, M. Rossander, A. Goude, and H. Bernhoff, "Measurements of the aerodynamic normal forces on a 12-kW straight-bladed vertical axis wind turbine," *Energies*, vol. 8, no. 8, pp. 8482–8496, 2015.
- [24] K. T. Ulrich and S. D. Eppinger, *Product Design and Development*, vol. 384. 2012.
- [25] E. Muljadi, K. Pierce, and P. Migliore, "Soft-stall control for variable-speed stall-regulated wind turbines," *J. Wind Eng. Ind. Aerodyn.*, vol. 85, no. 3, pp. 277–291, 2000.
- [26] D. Vaz, "Energia Eólica," 2016.
- [27] A. Hably, J. Dumon, and G. Smith, "Control of an airborne wind energy system with a Magnus effect," *Proc. Am. Control Conf.*, vol. 2016–July, no. May, p. 7, 2016.
- [28] A. Sedaghat, I. Samani, M. Ahmadi-Baloutaki, M. El Haj Assad, and M. Gaith, "Computational study on novel circulating aerofoils for use in Magnus wind turbine blades," *Energy*, vol. 91, pp. 393–403, 2015.
- [29] C. Badalamenti and S. Prince, "Effects of Endplates on a Rotating Cylinder in Crossflow," no. August, pp. 1–17, 2008.
- [30] N. Thouault, C. Breitsamter, N. Adams, J. Seifert, C. Badalamenti, and S. A. Prince, "Numerical Analysis of a Rotating Cylinder with Spanwise Disks," *AIAA J.*, vol. 50, no. 2, pp. 271–283, 2012.
- [31] Y. -b. Liang, L. -x. Zhang, E. -x. Li, X. -h. Liu, and Y. Yang, "Design Considerations of Rotor Configuration for Straight-Bladed Vertical Axis Wind Turbines," *Adv. Mech. Eng.*, vol. 6, p. 16, 2015.
- [32] I. Paraschivoiu, *Wind Turbine Design: With Emphasis on Darrieus Concept*. Montreal, Canada: Polytechnic International Press, 2002.

- [33] B. Sanborn, A. M. DiLeonardi, and T. Weerasooriya, "Tensile Properties of Dyneema SK76 Single Fibers at Multiple Loading Rates Using a Direct Gripping Method," *J. Dyn. Behav. Mater.*, vol. 1, no. 1, pp. 4–14, Mar. 2015.
- [34] DSM Dyneema B. V., "Technical brochure: Dyneema in marine and industrial applications," vol. 31, no. 46, p. 4, 2008.
- [35] Performance Composites Ltd, "Mechanical Properties of Carbon Fibre Composite Materials." [Online]. Available: http://www.performance-composites.com/carbonfibre/mechanicalproperties_2.asp. [Accessed: 14-May-2018].
- [36] M. Islam, A. Fartaj, and R. Carriveau, "Analysis of the design parameters related to a fixed-pitch straight-bladed vertical axis wind turbine," *Wind Eng.*, vol. 32, no. 5, pp. 491–507, 2008.
- [37] R. Eppler, *Airfoil Design and Data*. Springer-Verlag Berlin Heidelberg, 1990.
- [38] Alxion, "STK Wind and water turbines alternators." [Online]. Available: <http://www.alxion.com/products/stk-alternators/>. [Accessed: 25-May-2018].
- [39] "Xfoil Interface Updated - File Exchange - MATLAB Central," *MathWorks*. [Online]. Available: <https://www.mathworks.com/matlabcentral/fileexchange/49706-xfoil-interface-updated>. [Accessed: 09-Oct-2018].
- [40] MIT, "Xfoil - Subsonic Airfoil Development System," 2013. [Online]. Available: <https://web.mit.edu/drela/Public/web/xfoil/>. [Accessed: 11-Aug-2018].
- [41] Germanischer Lloyd Industrial Services GmbH, *Guideline for the Certification of Wind Turbines*. 2010.
- [42] J. Altenbach, H. Altenbach, and W. Kissing, *Mechanics of Composite Structural Elements*. Springer.

Appendix A

A.1 – Script for load calculation for the full structure analysis

```
clear all

% % Air properties
rho = 1.225; % [kg/m3]
nu = 1.5e-5; % [m2/s]

% % Design Dimensions
D_balao = 3.68; % [m]
D_turb = 7.7; % [m]
L = 6; % [m]

% % Design Parameters
solid = 0.3; % solidity
Nb = 3; % number of blades
cordai = round(solid*D_turb/(2*Nb),2); % [m] blade chord
esp = 0.22*8*10^-3; % [m] profile skin thickness

rho_blade = 1.60e3; % [kg/m3] Densidade da Fibra + Matriz

% % Load Cases wind velocity and rotational speed
w_rated = 104; % [rpm]
w_cutout = 124; % [rpm]
v_rated = 10; % [m/s]
v_cutout = 20; % [m/s]

speed = input('Load Case ', 's');
switch speed
    case 'A'
        V = v_rated;
        w = w_rated;
    case 'B'
        V = v_cutout;
        w = w_cutout;
    otherwise
        disp('Insert valid Load Case')
end

TSR = round( (w*pi*D_turb) / (60*V) ,1);
Cp = tabela_cp_tsr(TSR);

% Angles for every position theta
ang = 30; % increment
arc = deg2rad(ang)*D_turb/2;
theta0 = deg2rad([0:ang:360]');
theta0(length(theta0)) = []; % removing the 360
gamma0 = round( rad2deg(atan( - sin(theta0) ./ (TSR + cos(theta0)) )) ,1); %
[°] Local inflow angle
pitch = -4; % [°] Blade incidence angle
alpha0 = gamma0 - pitch; % [°] Angle of attack

alpha = alpha0;
graus0 = rad2deg(theta0); graus = graus0;

% Relative velocity and Reynolds number for every position theta
```

```

v_rel = V*sqrt(TSR^2+2*TSR*cos(theta0)+1); % [m/s]
Re = v_rel*cordai / nu;

% Computation of the aerodynamic coefficients
CL_vec = zeros(length(alpha0),1);
CD_vec = zeros(length(alpha0),1);
for i = 1:length(alpha0)
    % Interface with Xfoil
    [polar,foil] = xfoil('NACA0018',alpha0(i),Re(i),0.2,'oper/vpar n
12','oper iter 500');
    if isnan(polar.alpha) == 1
        CL_vec(i) = 0;
        CD_vec(i) = 0;
    else
        CL_vec(i) = polar.CL;
        CD_vec(i) = polar.CD;
    end
end

% Clearing the vectors of null entries
for h = length(CL_vec):-1:1
    if CL_vec(h,1) == 0 && CD_vec(h,1) == 0
        CL_vec(h) = []; CD_vec(h) = [];
        theta0(h) = []; gamma0(h) = [];
        v_rel(h) = [];
        alpha(h) = [];
        graus(h) = [];
    end
end

% % Loads calculation
FL = 0.5.*CL_vec.*rho.*cordai.*v_rel.^2; % [N/m] Lift Force
FD = 0.5.*CD_vec.*rho.*cordai.*v_rel.^2; % [N/m] Drag Force
FN = FL.*cos(deg2rad(gamma0)) + FD.*sin(deg2rad(gamma0)); % [N/m] Normal
Force
FT = FL.*sin(deg2rad(gamma0)) - FD.*cos(deg2rad(gamma0)); % [N/m] Tangent
Force

% Calculation of the profile area and the second moments of area for NACA0018
% Profile defined through points
[Ix_blade, Iy_blade, A_blade] = calcula_inercia_area_naca(esp);

% Centrifugal Load
FC = rho_blade*A_blade*D_turb/2*(w*2*pi/60)^2; % [N/m]

% Gravitational Load
massa = rho_blade*A_blade*L; % [kg]
W = rho_blade*A_blade*9.8; % [N/m]
W_n = - W*cos(theta0); % [N/m]
W_t = - W*sin(theta0); % [N/m]

% Partial Safety factor for loads
SF_loads = 1.35;
% Distributed loads
Fn_total = FN + FC + W_n; % [N/m] characteristic value of the normal load
Ft_total = FT + W_t; % [N/m] characteristic value of the tangential load
Fn_design = SF_loads*Fn_total; % [N/m] design value of the normal load
Ft_design = SF_loads*Ft_total; % [N/m] design value of the tangential load
% Acting forces
FN = Fn_design*L; % [N]

```

```

FT = Ft_design*L; % [N]

% Maximum values of the forces
[FN_max, tetaN] = max(FN); % [N]
[FT_max, tetaT] = max(FT); % [N]

```

A.2 – Script for load calculation for the support arms analysis

```

% % Load Cases wind velocity and rotational speed
w_rated = 104; % [rpm]
w_cutout = 124; % [rpm]
v_rated = 10; % [m/s]
v_cutout = 20; % [m/s]

speed = input('Load Case ', 's');
switch speed
    case 'A'
        V = v_rated;
        w = w_rated;
    case 'B'
        V = v_cutout;
        w = w_cutout;
    otherwise
        disp('Insert valid Load Case')
end

chord = input('Support arm chord in metres: '); % [m] corda do perfil

% Length of a support arm
ang = deg2rad(60);
L_arm = round(sqrt((D_balao*sin(ang)/2)^2 + (D_turb/2 - D_balao*cos(ang)/2)^2), 2);

SF_loads = 1.35; % Partial Safety factor for loads

TSR = round((w*pi*D_turb) / (60*V_cutout), 2);

% Position of the support arms in relation to the wind velocity
angles = deg2rad([0 180 120 300 240 60]);
% Obtained values of CD for the respective Reynolds numbers
CD = [0.007 0.016 0.013 0.009 0.013 0.009];

% Initialization of vectors
v_rel_n = zeros(1, length(CD)); Re = v_rel_n; FD_d_arm = Re;

for i = 1:length(angles)
    % [m/s] normal relative wind speed
    v_rel_n(i) = round(w*pi*D_turb/60 + V*cos(angles(i)), 1);
    Re(i) = v_rel_n(i).*chord / nu;

    FD_arm = 0.5.*CD(i).*rho_arm.*chord.*v_rel_n(i).^2; % [N/m]
    % characteristic value of the load
    FD_d = SF_loads*FD_arm; % [N/m] design value of the load
    FD_d_arm(i) = FD_d*L_arm; % [N] Acting force
end

```

Appendix B

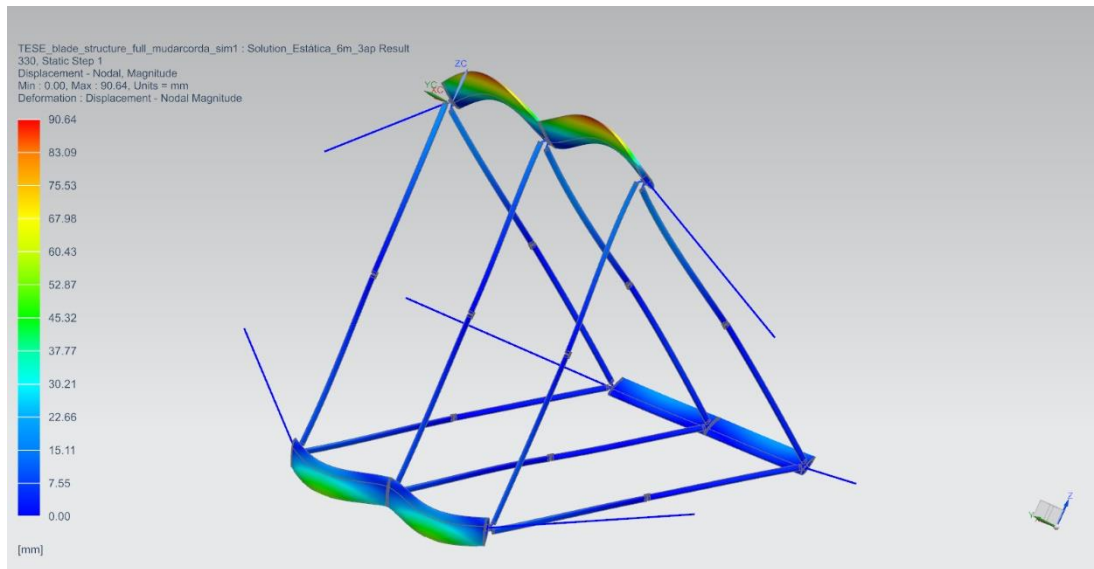


Figure B.1 – Displacement magnitude computed from the full structure analysis, for position $\theta = 330^\circ$

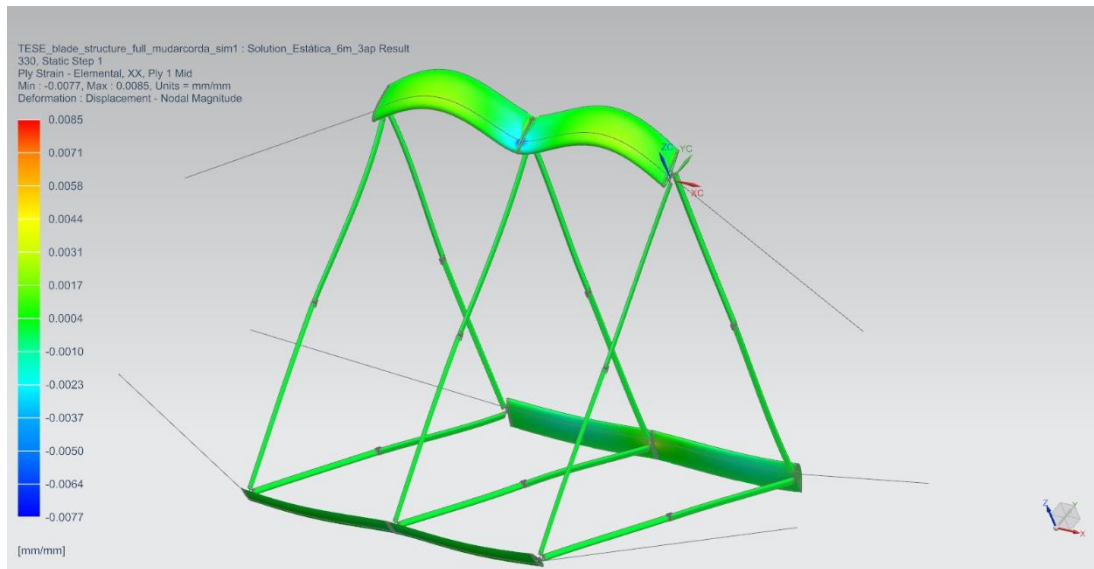


Figure B.2 – Ply Strain ε_{11} for ply 1 computed from the full structure analysis, for position $\theta = 330^\circ$

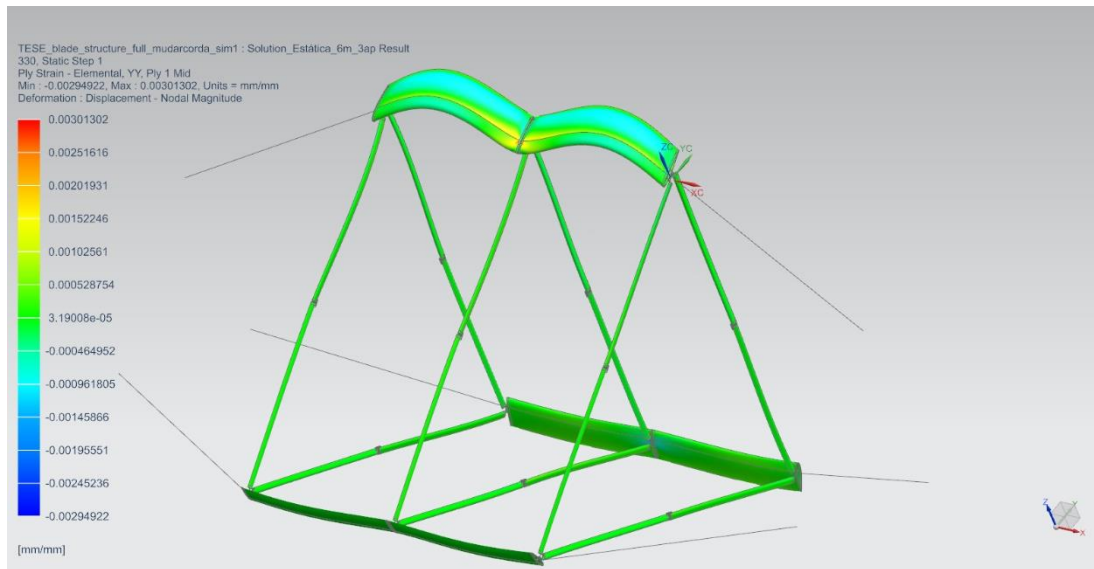


Figure B.3 – Ply Strain ε_{22} for ply 1 computed from the full structure analysis, for position $\theta = 330^\circ$

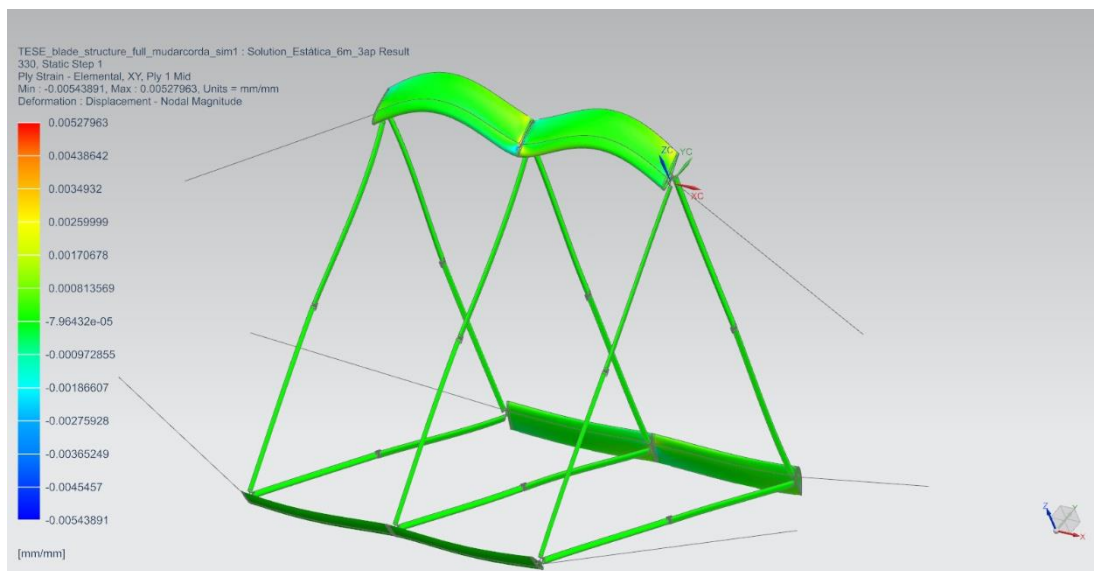
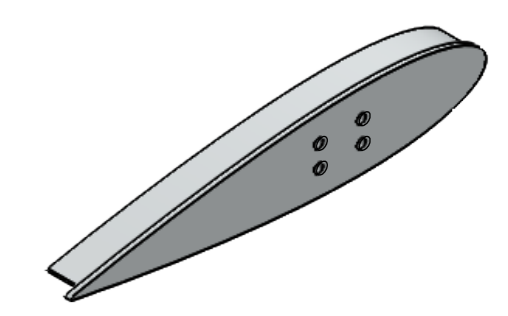
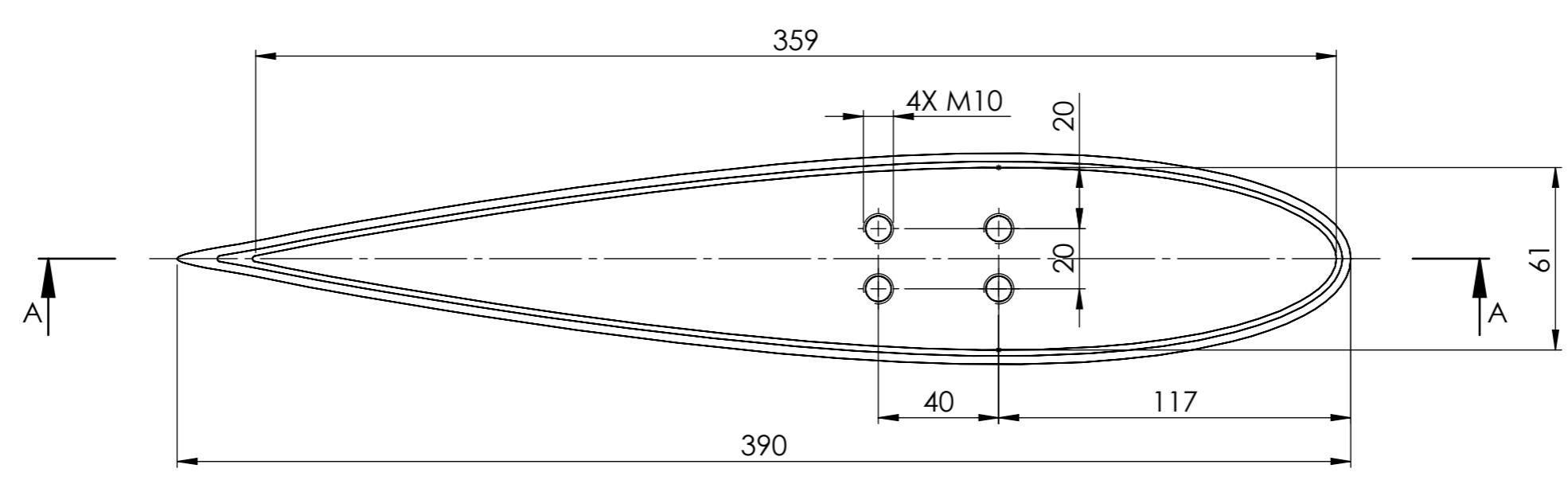
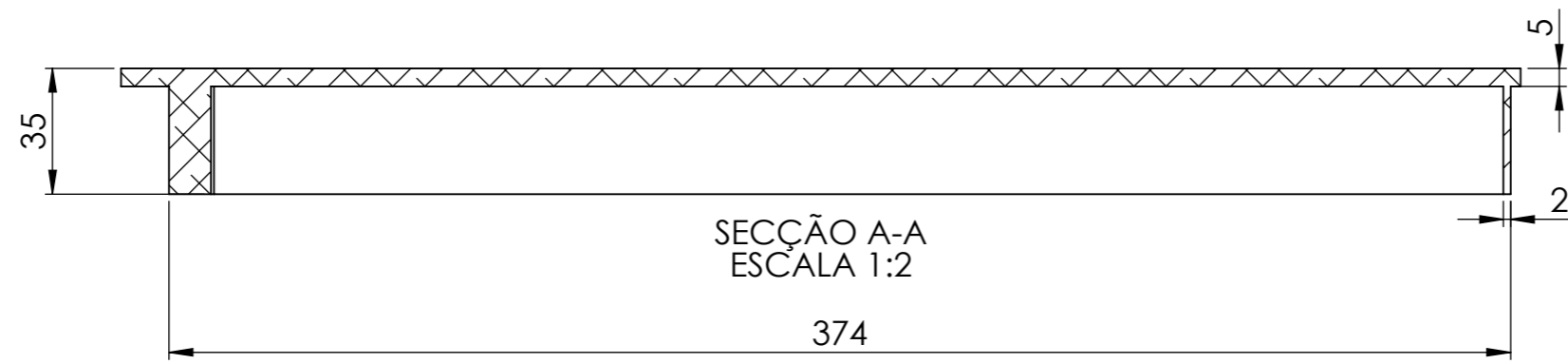


Figure B.4 – Ply Strain ε_{12} for ply 1 computed from the full structure analysis, for position $\theta = 330^\circ$

Appendix C

Technical drawings of the main components of the turbine structure.



UNLESS OTHERWISE SPECIFIED: DIMENSIONS ARE IN MILLIMETERS SURFACE FINISH: TOLERANCES: LINEAR: ISO 2768-m ANGULAR: ISO 2768-m			FINISH:		DEBURR AND BREAK SHARP EDGES		DO NOT SCALE DRAWING		REVISION	
DRAWN C. Gonçalves			SIGNATURE		DATE		TITLE: BLADE COVER			
CHK'D							DWG NO. 01		A3	
APPV'D							SCALE: 1:2		SHEET 1 OF 1	
MFG					MATERIAL: ALUMINIUM 7075-T6		WEIGHT:			
Q.A										

4 3 2 1

F

F

E

E

D

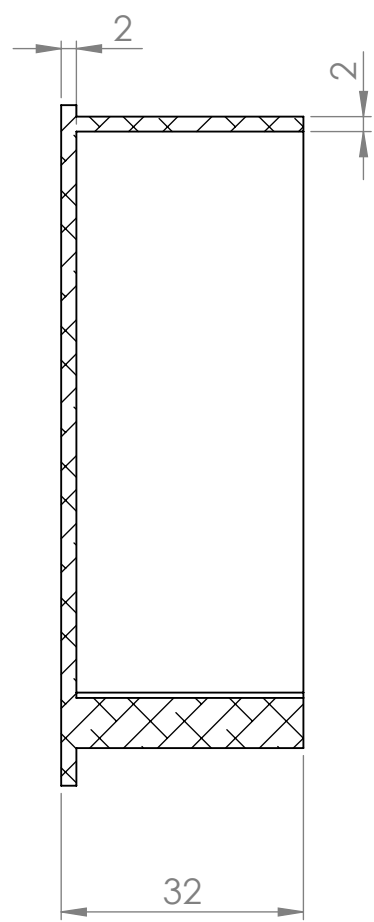
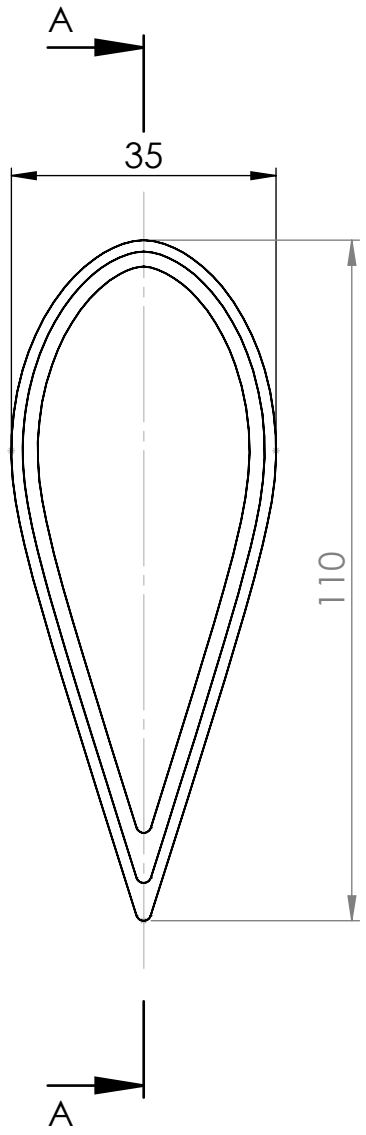
D

C

C

B

B



SECTION A-A
SCALE 1 : 1

UNLESS OTHERWISE SPECIFIED:
DIMENSIONS ARE IN MILLIMETERS
SURFACE FINISH:
TOLERANCES:
LINEAR: ISO 2768-m
ANGULAR: ISO 2768-m

FINISH:

DEBURR AND
BREAK SHARP
EDGES

DO NOT SCALE DRAWING

REVISION

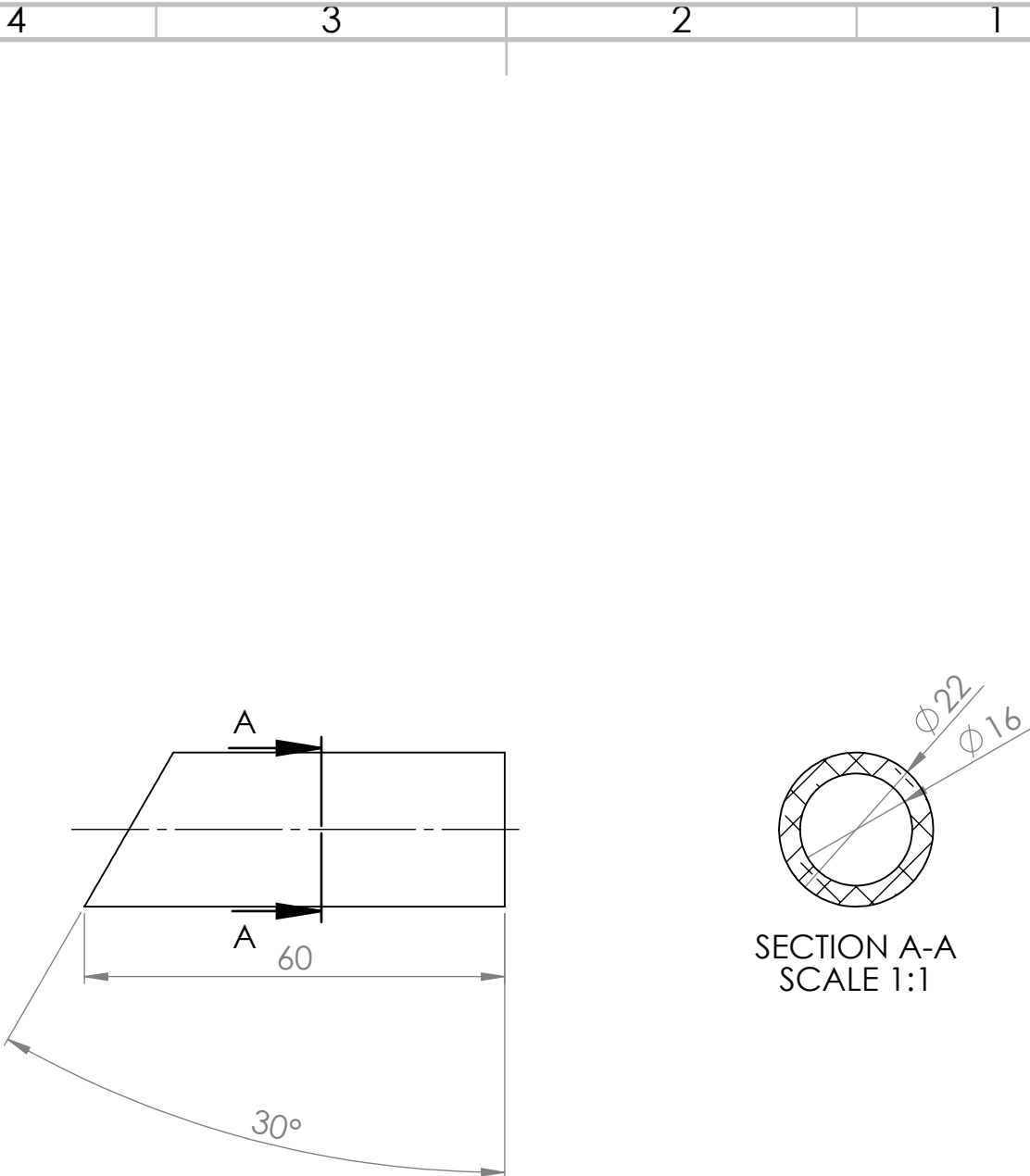
	NAME	SIGNATURE	DATE
DRAWN	C. Gonçalves		
CHKD			
APPV'D			
MFG			
Q.A			

TITLE:	ARM SUPPORT	
MATERIAL: Aluminium 7075-T6	DWG NO.	02
WEIGHT:	SCALE: 1:1	SHEET 1 OF 1

A

A

4 3 2 1



UNLESS OTHERWISE SPECIFIED:
 DIMENSIONS ARE IN MILLIMETERS
 SURFACE FINISH:
 TOLERANCES:
 LINEAR: ISO 2768-m
 ANGULAR: ISO 2768-m

FINISH:

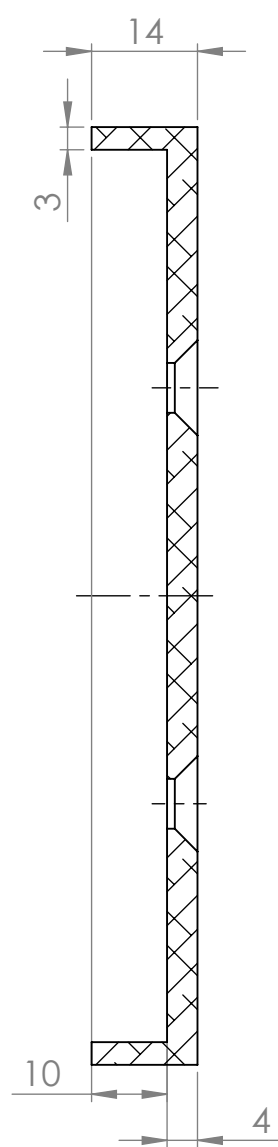
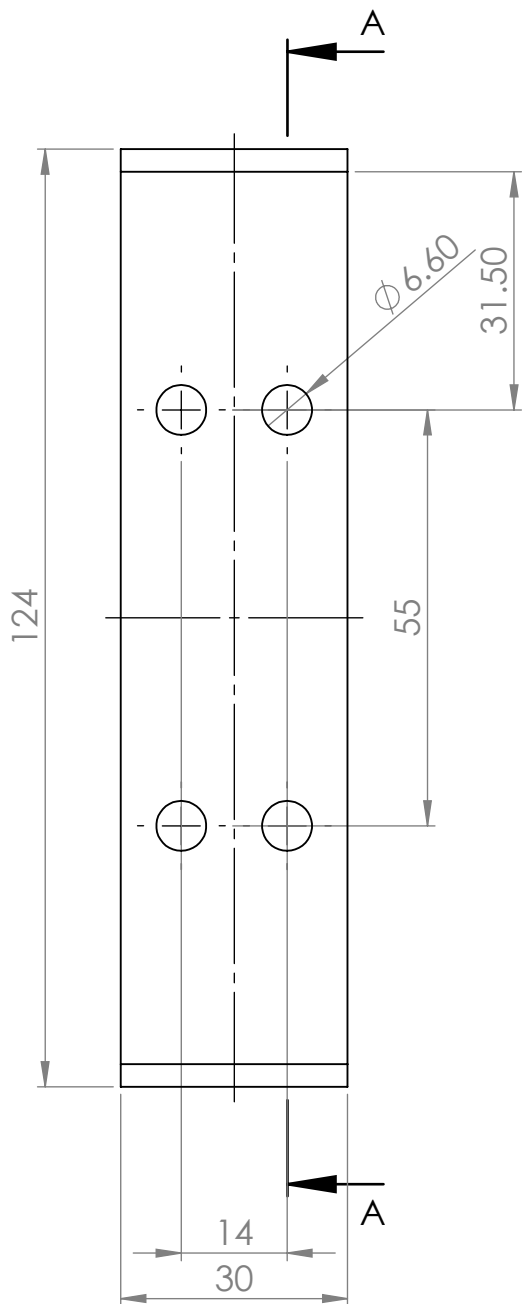
DEBURR AND
 BREAK SHARP
 EDGES

DO NOT SCALE DRAWING

REVISION

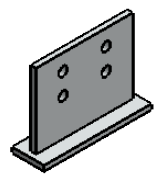
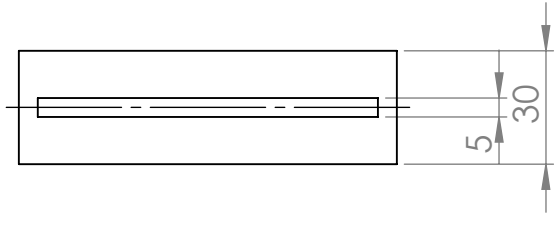
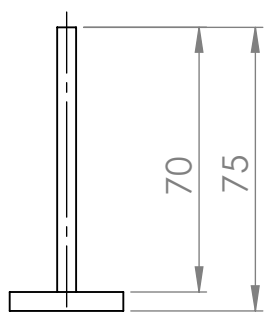
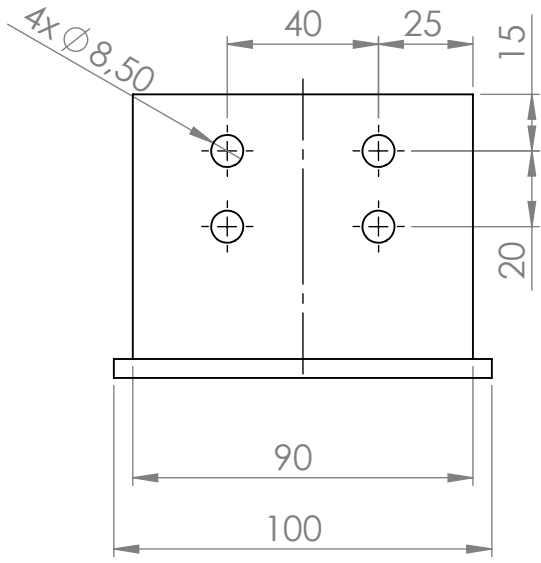
	NAME	SIGNATURE	DATE
DRAWN	C. Gonçalves		
CHK'D			
APPV'D			
MFG			
Q.A			

TITLE: BLADE SUPPORT TUBE		A4
DWG NO. 03		
WEIGHT:	SCALE:1:1	SHEET 1 OF 1



SECTION A-A
SCALE 1 : 1

UNLESS OTHERWISE SPECIFIED: DIMENSIONS ARE IN MILLIMETERS SURFACE FINISH: TOLERANCES: LINEAR: ISO 2768-m ANGULAR: ISO 2768-m			FINISH:	DEBURR AND BREAK SHARP EDGES	DO NOT SCALE DRAWING	REVISION																								
<table border="1"> <thead> <tr> <th>NAME</th> <th>SIGNATURE</th> <th>DATE</th> <th></th> </tr> </thead> <tbody> <tr> <td>DRAWN</td> <td>C. Gonçalves</td> <td></td> <td></td> </tr> <tr> <td>CHKD</td> <td></td> <td></td> <td></td> </tr> <tr> <td>APPVD</td> <td></td> <td></td> <td></td> </tr> <tr> <td>MFG</td> <td></td> <td></td> <td></td> </tr> <tr> <td>Q.A</td> <td></td> <td></td> <td></td> </tr> </tbody> </table>				NAME	SIGNATURE	DATE		DRAWN	C. Gonçalves			CHKD				APPVD				MFG				Q.A				TITLE: ARM SUPPORT BASE		
NAME	SIGNATURE	DATE																												
DRAWN	C. Gonçalves																													
CHKD																														
APPVD																														
MFG																														
Q.A																														
MATERIAL: ALUMINIUM 7075-T6				DWG NO. 04		A4																								
WEIGHT:				SCALE: 1:1		SHEET 1 OF 1																								



UNLESS OTHERWISE SPECIFIED:
 DIMENSIONS ARE IN MILLIMETERS
 SURFACE FINISH:
 TOLERANCES:
 LINEAR: ISO 2768-m
 ANGULAR: ISO 2768-m

FINISH:

DEBURR AND
 BREAK SHARP
 EDGES

DO NOT SCALE DRAWING

REVISION

	NAME	SIGNATURE	DATE
DRAWN	C. GONÇALVES		
CHK'D			
APPV'D			
MFG			
Q.A			

TITLE:	BLADE SUPPORT	
DWG NO.	05	A4
WEIGHT:		
SCALE: 1:2		SHEET 1 OF 1

MATERIAL: ALUMINIUM 7075-T6

4

3

2

1

F

E

D

C

B

A

F

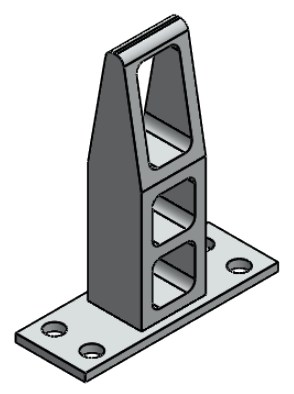
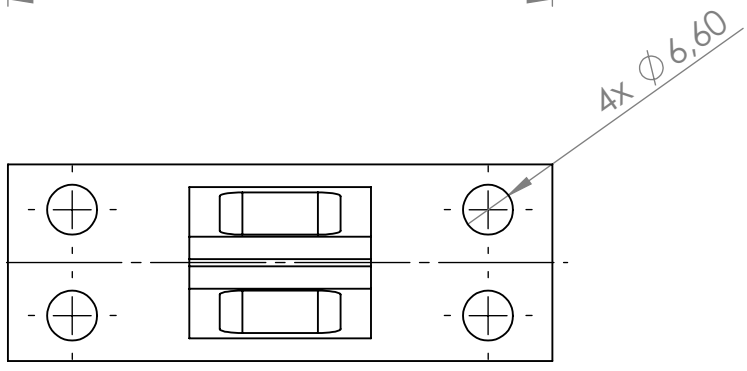
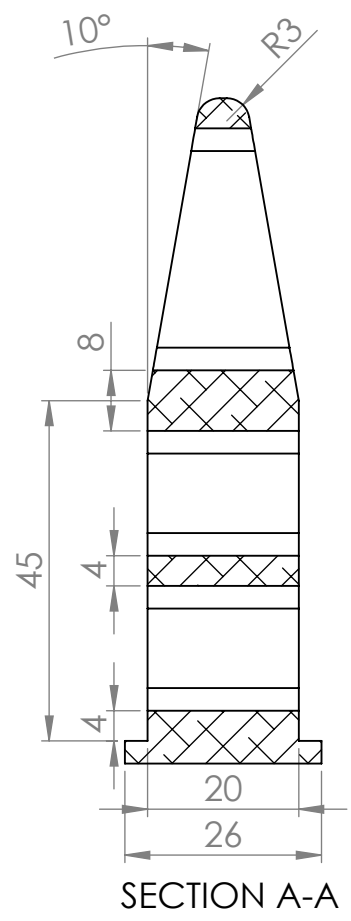
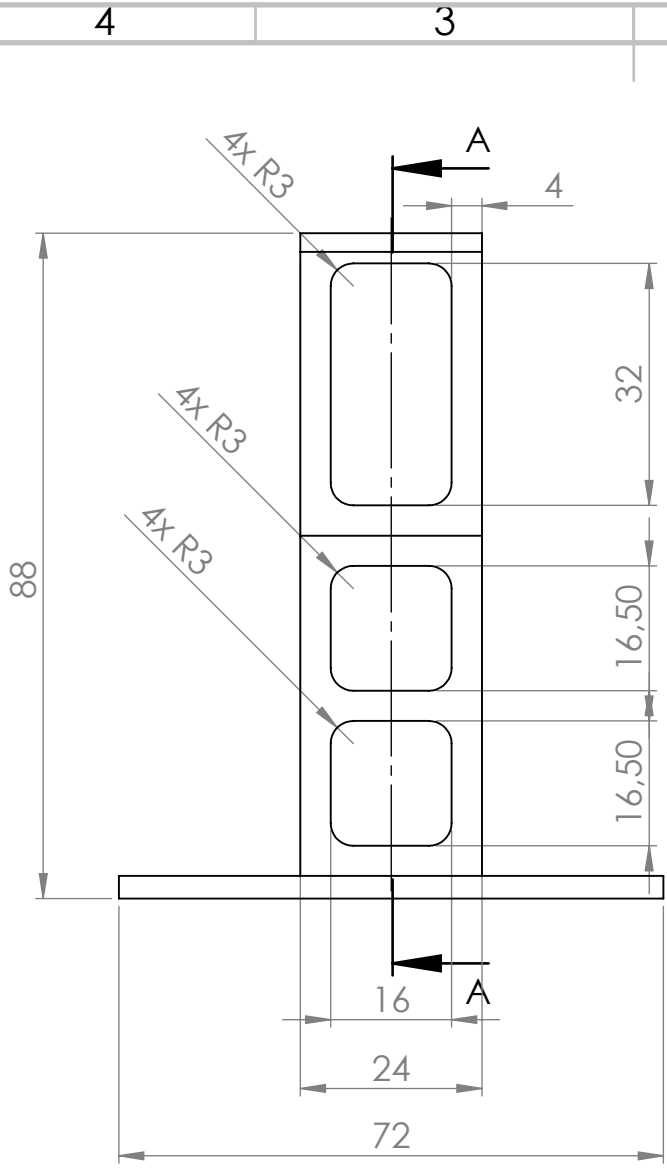
E

D

C

B

A



UNLESS OTHERWISE SPECIFIED:
 DIMENSIONS ARE IN MILLIMETERS
 SURFACE FINISH:
 TOLERANCES:
 LINEAR: ISO 2768-m
 ANGULAR: ISO 2768-m

FINISH:

DEBURR AND
 BREAK SHARP
 EDGES

DO NOT SCALE DRAWING

REVISION

NAME	SIGNATURE	DATE
DRAWN		
CHK'D		
APPV'D		
MFG		
Q.A		

TITLE:
**ARM INSERT
 SUPPORT**

DWG NO.
06

SCALE: 1:1

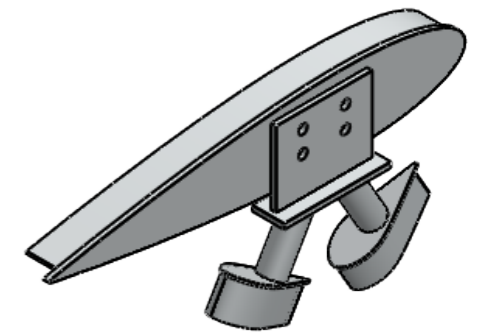
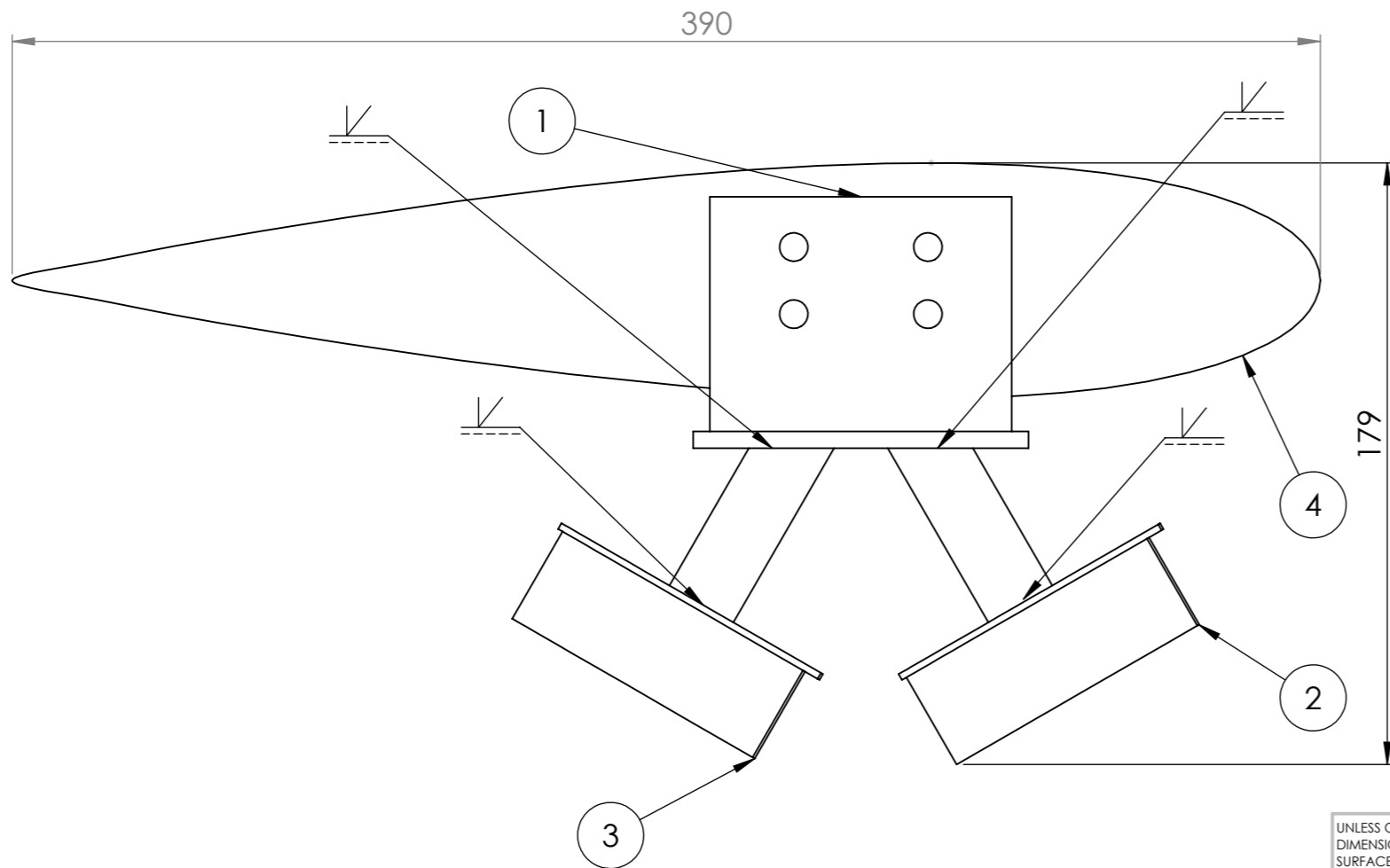
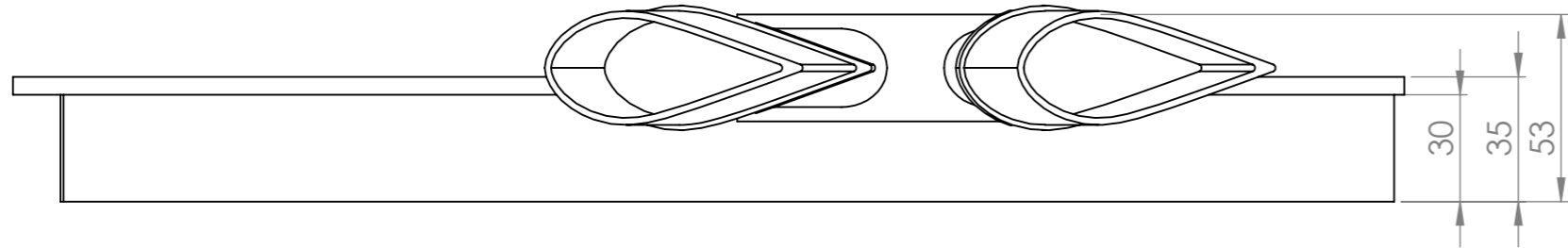
SHEET 1 OF 1

MATERIAL: ALUMINIUM 7075-T6

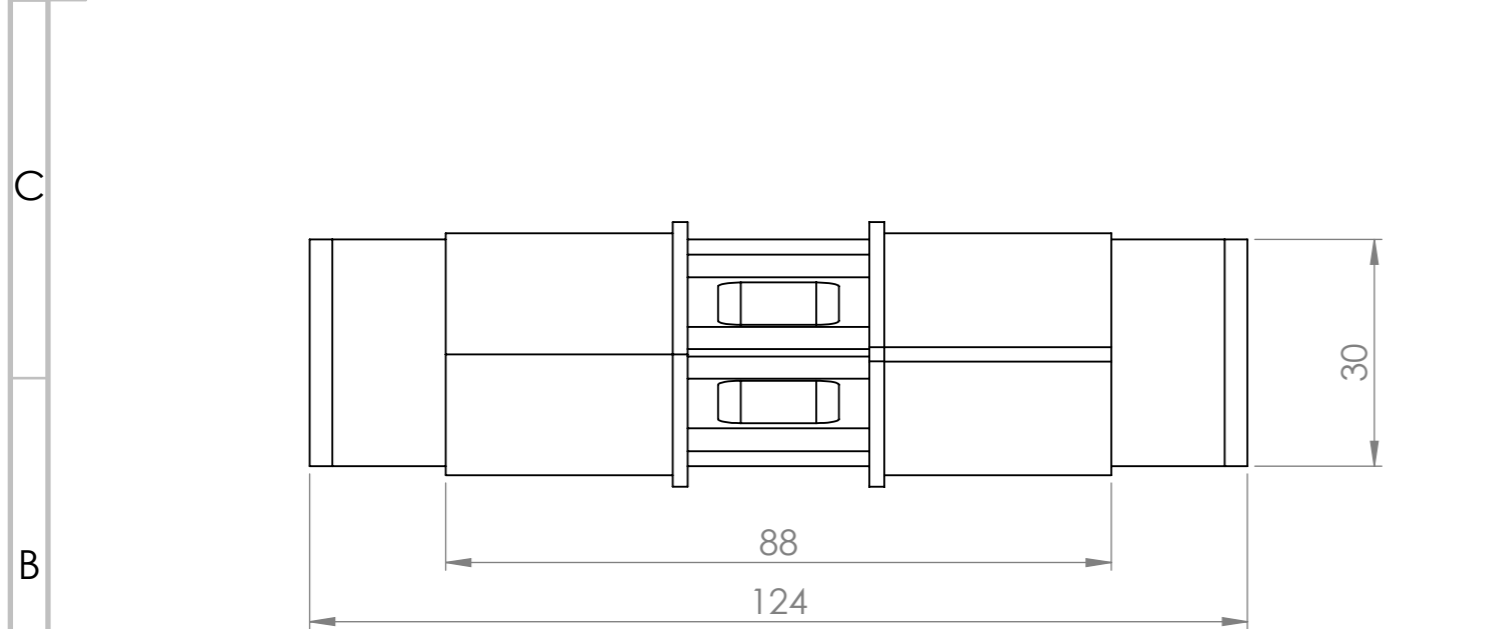
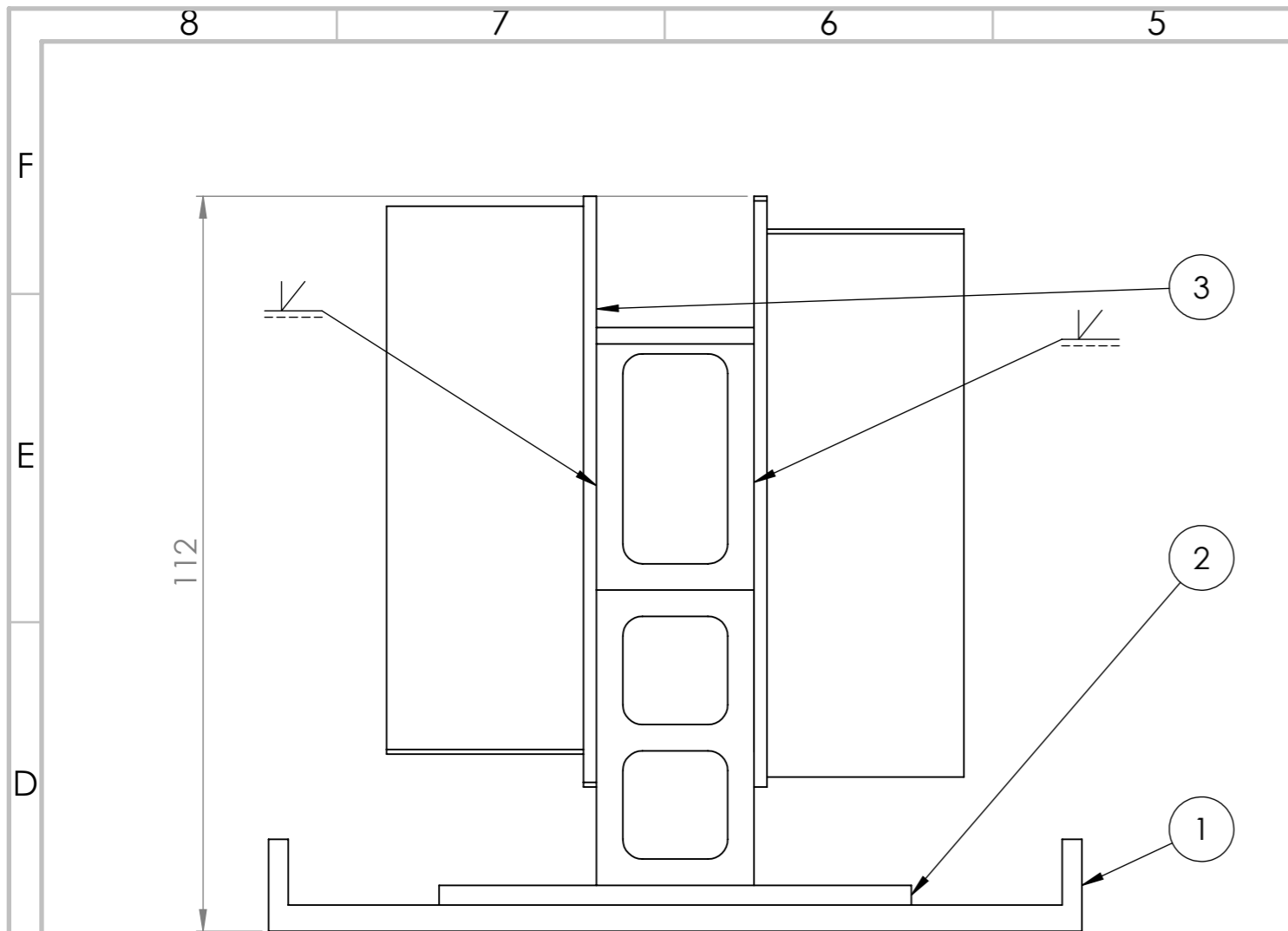
WEIGHT:

A4

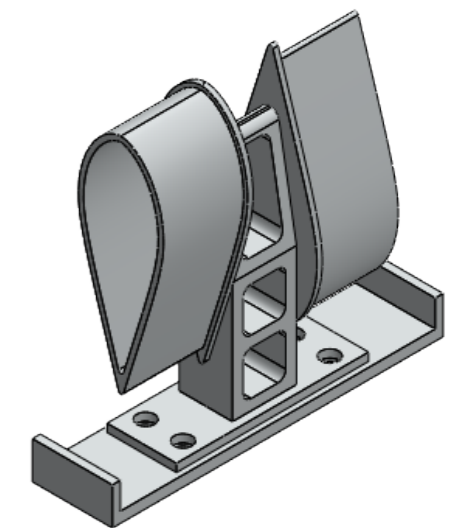
ITEM NO.	PART NAME	MATERIAL	QTY.
1	Blade Support	Aluminium 7075-T6	1
2	Blade Support (Leading Edge)	Aluminium 7075-T6	1
3	Blade Support (Trailing Edge)	Aluminium 7075-T6	1
4	Blade Cover	Aluminium 7075-T6	1



UNLESS OTHERWISE SPECIFIED: DIMENSIONS ARE IN MILLIMETERS SURFACE FINISH: TOLERANCES: LINEAR: ISO 2768-m ANGULAR: ISO 2768-m			FINISH:		DEBURR AND BREAK SHARP EDGES		DO NOT SCALE DRAWING		REVISION			
NAME	SIGNATURE	DATE				TITLE:		BLADE AND ARM SUPPORT ASSEMBLY				
DRAWN	C. GONÇALVES					DWG NO.					07	
CHK'D						SCALE:1:5					SHEET 1 OF 1	
APPV'D						WEIGHT:						
MFG						MATERIAL:					A3	
Q.A												



ITEM NO.	PART NAME	MATERIAL	QTY.
1	ARM SUPPORT BASE	ALUMINIUM 7075-T6	1
2	ARM INSERT SUPPORT	ALUMINIUM 7075-T6	1
3	ARM SUPPORT	ALUMINIUM 7075-T6	2



UNLESS OTHERWISE SPECIFIED: DIMENSIONS ARE IN MILLIMETERS SURFACE FINISH: TOLERANCES: LINEAR: ISO 2768-m ANGULAR: ISO 2768-m		FINISH:	DEBURR AND BREAK SHARP EDGES	DO NOT SCALE DRAWING	REVISION
NAME	SIGNATURE	DATE		TITLE: ARM SUPPORT NET LINK	
DRAWN C. GONÇALVES				DWG NO. 08	A3
CHK'D				SCALE:1:2	SHEET 1 OF 1
APPV'D					
MFG					
Q.A			MATERIAL:		
			WEIGHT:		